Surface and Electronic Structures of Some Functionality Materials Studied by Scanning Tunneling Microscopy

Thesis

submitted to

the Graduate University for Advanced Studies

for the degree

of

Doctor of Philosophy

by

Yoshihisa Mori

November, 1992

Acknowledgments

First, I must thank Professor Yusei Maruyama (The Graduate University for Advanced Studies and Institute for Molecular Science) for all that he has done for me in the past 3 years. He gave me a very interesting work and many suggestions.

The author would like to express his thanks to Dr. Tamotsu Inabe (Hokkaido University), Dr. Takehiko Mori (Institute for Molecular Science) and Dr. Kunio Awaga (The University of Tokyo) for their kind help and the fruitful discussions.

The author would like to thank Dr. Yasuhiro Nakazawa (Institute for Molecular Science) and Mr. Hironori Ogata (The Graduate University for Advanced Studies) for magnetic susceptibility measurement, and Dr. Hajime Hoshi (Institute for Molecular Science) and Toshifumi Terui (The Graduate University for Advanced Studies) for surface observation by using scanning electron microscope, and all the member of the MAD group for their helpful discussions.

The author thanks Professor Gunzi Saito (Kyoto University) and Dr. Hatsumi Mori (International Superconductivity Technology Center) for the supply of (BEDT-TTF) salt single crystals, Professor Masatoshi Sato for $YBa_2Cu_3O_x$ single crystal and Dr. S. M. Critchley (University Park Nottingham) for spun phthalocyanine films.

The author acknowledges Dr. H Bando (Electrotechnical Laboratory) for his ideas of LTSTM and Mr. Hisashi Yoshida, Mr. Kato Shinjij and Mr. Mizutani Nobuo (Equipment Development Center) for their great help to the progress of this study.

The author also should express his thanks to a great many friends. Mr. Toshifumi Terui, Mr. Hironori Ogata and Mr. Kentaro Iwasaki (The Graduate University for Advanced Studies) have been good friends and good partners of midnight drive and meal. They have been essential to my student life. Mr. Wataro Morita and all the member of "Tenrikyou AISHIN Branch Church" have been very kindly and necessary for my OKAZAKI life. Mr. Hirofumi Sakaguchi and Mr. Toshihisa Ito who are my best friends past ten years, have been also indispensable for my life.

The author also acknowledges my parents for their permission of everything I have done for 27 years.

Finally, I would like to acknowledge my future wife, Noriko. Thank you !!

Contents

1. General Introduction

1.1. Introduction

The microscope technique has advanced gradually aiming higher resolution, and the method of obtaining a microscopic image has changed from with light to with electron. One of the most useful methods is electron microscopy which is classified to Scanning Electron Microscopy (SEM) and Transmission Electron Microscopy (TEM), and by using these systems, we can approach to a nano world. But they have still a limit in resolution. We can not see any smaller region than the wavelength of electron so far as the electron microscope uses electron wave. In 1982, a new type of microscope was invented to make a break-through for this problem by Binnig and Rohrer[1]. The microscope is based on quantum mechanical tunneling effect of electron and it is called Scanning Tunneling Microscopy (STM). The fundamental difference between SEM or TEM and STM is that the former uses free electrons and the latter uses electrons in a substance. Since the development of STM, the method has been applied not only to surface science but also to various fields, quickly. At the beginning, STM could be used only for conductive materials, but according to the development of Atomic Force Microscope (AFM)[2], insulating materials can be also observed. In addition, many kinds of microscope (for example, Magnetic Force Microscope; MFM[3],[4], Frictional Force Microscope; FFM[5],[6], Scanning Ion-Conductance Microscope; SICM[7], Localized Charge Force Microscope; LCFM[8],[9], Scanning Thermal Profiler; STP[10] and so on) have been available. The environmental condition to use the microscope has been less specified, that is, not only in atmosphere at room temperature, but also in vacuum or in water, at low temperatures or at high temperatures. Moreover, not only surface structure, but also electronic structure in atomic scale can be detected by Scanning Tunneling Spectroscopy (STS).

STS which combines STM with tunneling spectroscopy can measure the electronic structure of some real space portion with atomic resolution. The method is specially useful for research of the energy structure near Fermi surface of materials and is the most direct and

reliable one to determine a superconducting gap which characterizes the nature of a superconductor.

In recent years, such exotic superconductors as organic superconductors [11] or copper oxide superconductors[12] have been discovered and it has been a very important subject to understand the essential nature or mechanism of the superconductivity of these substances. In this line, tunneling spectroscopic studies have been carried out for these materials by using conventional tunneling spectroscopy techniques (see Table 4-1). Obtained and reported results are, however, rather scattered in many respects, and still now it is in controversial situation for understanding the superconductivity in these substances.

STM/STS could afford the most reliable and direct information on the superconductivity in these substances if we had a complete Low-Temperature STM/STS system. This is a motivation of this thesis work, and the objective of this work is to realize the construction of a Low-Temperature STM/STS (LTSTM/STS). Several attempts for LTSTM/STS have been reported[13],[14],[15],[16], but they have not yet been perfectly completed. A complete LTSTM/STS means to measure a tunneling spectrum scanning the probe from a point to point in a real space at an atomic resolution with observing STM image at low temperatures.

In this thesis, essential features of STM and fundamental principles of tunneling spectroscopy are described in this General Introduction. The second chapter is for Instrumentation which is the most important part of this thesis work, and in the first place the general features of a conventional STM (Nanoscope II, Digital Instruments) are explained. In the second place, details of the construction of our LTSTM/STS system are described; instrumentation, parts, electronics and some testing results. Every idea is quite originally applied to this system. In the third place, the preparation of tunneling probe tips is stated, and the crucial importance of tip conditions for STM technique is clarified.

The third chapter is for the presentation of examples of STM observation. Graphite is a standard sample for STM and an atomic resolution is confirmed with it. Next examples are $(BEDT\text{-}TTF)_2X$ compounds because some of them are typical organic superconductors

which could be used for LTSTM/STS experiment in future. C_{60} is also a very interesting molecule and the structure of its thin film on graphite is observed for the first time.

In the fourth chapter, STM/STS technique is applied for a direct observation of the electronic structure at a molecular resolution. This is very unique and useful technique for analyzing microscopic natures of substances. Actually $(BEDT\text{-}TTF)_2KHg(SCN)_4$ is examined by this method and a two-dimensional electronic structure is clearly revealed for the first time. The second example is a typical copper oxide superconductor, $YBa_2Cu_3O_y$. Tunneling spectra of a $YBa_2Cu_3O_y$ single crystal is measured in superconducting state at 12K by using our home-made LTSTM/STS system. Obtained superconducting gap energy, ~58 meV seems to be reasonable comparing with other's data which were obtained by using different or similar methods.

The construction of LTSTM/STS system has not yet been completely achieved, but almost all obstacles have been overcome by original ideas and trial-and-error efforts. Details of the procedure are described in this thesis.

1.2. Scanning Tunneling Microscopy (STM)

At a metal-vacuum interface, the wave function for an electron at Fermi energy does not vanish outside the metal but rather decays exponentially as e^{-kx}, where $k \cong \sqrt{\frac{2m}{\hbar^2}}\sqrt{\phi}$, x is the distance into the vacuum, m is the electron mass and ϕ is the metal work function[17]. If two conductors are very close to each other within a few tenth Å, then electrons in one conductor can move to another one. When a voltage (V) which has lower energy than the workfunction, is applied between two metals, the tunnel current density is

$$j = \frac{\alpha\beta\bar{\phi}^{-1/2}V}{z} e^{-\alpha z\bar{\phi}^{-1/2}}$$

$$\alpha = \frac{4\pi\sqrt{2m}}{h} = 1.025 \quad (\text{Å}^{-1}eV^{-1/2})$$

$$\beta = \frac{e^2}{4\pi h}$$

$$\bar{\phi} = \frac{\phi_1 + \phi_2}{2},$$

where z is the distance between two metals and h is Planck's constant[18]. Because the workfunction of normal metal is ~ 5 eV, if z value is changed by only 1 Å, the tunnel current is changed by one figure as shown in Fig. 1-1. This mechanism is applied to STM. Therefore, the resolution is less than 1 Å, then an atom can be seen by using STM.

The principle of STM is shown in Fig. 1-2. A tip is controlled three dimensionally by a piezoelectric element. When a distance between sample and tip is below 10 Å and bias voltage is applied between them, a tunneling current begins to flow. The tunneling current is amplified by an operational amplifier then transferred to a control unit. An electronic feedback loop in the control unit is used to keep the tunneling current constant by adjusting the tip-sample separation. This adjusting voltage is just correlated with surface structure in the z-direction, and then an STM image can be obtained.

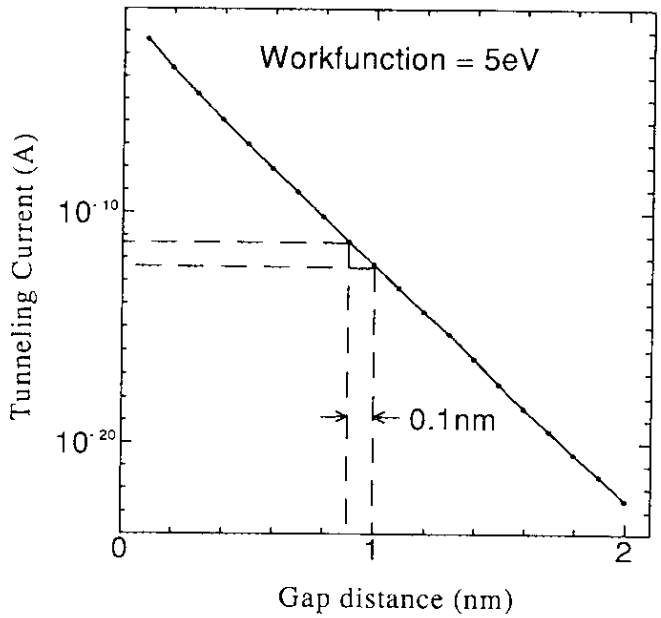

Fig. 1-1 The relationship between gap distance and tunneling current.

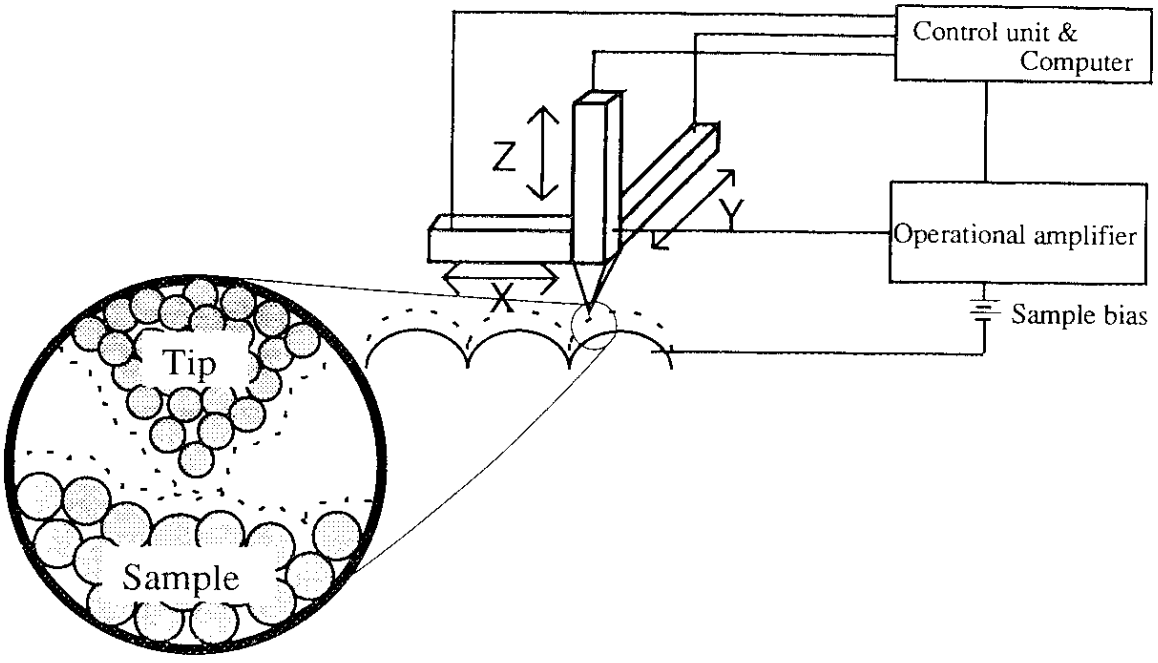

Fig. 1-2 The principle of STM.

The resolution of STM in the z-direction is very high as shown in Fig.1-3. Since the typical tunneling current is 1 ~ 10 nA and the current of this order can be controlled and detected within 1 % accuracy, the vertical resolution achieves about 0.1 Å. On the other hand, the lateral resolution is influenced by tip shape and is given by

$\Delta = \sqrt{2\lambda(R+z)}$,

where R is the radius of curvature of tip and λ is $2/\alpha\phi$[19]. If the top of the probe would be just one atom (R= 1 Å), the lateral resolution could be ~3 Å.

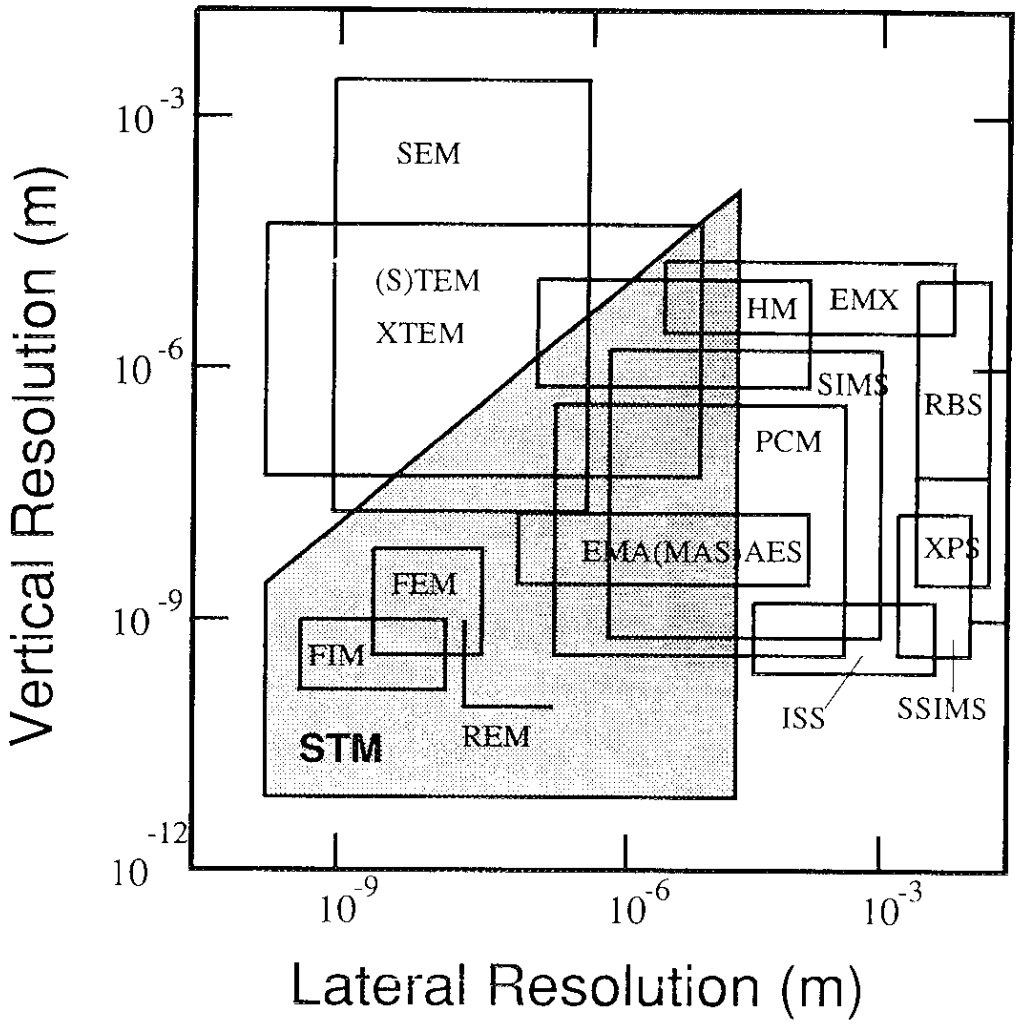

Fig. 1-3 The comparison of resolution for some microscopes.

1.3. Tunneling Spectroscopy

The tunneling spectroscopy provides not only a direct measurement of the superconducting energy gap and/or the phonon density of states, but also of the electron-phonon coupling strength. Therefore, it is a powerful tool for studying materials science, so several types of tunneling spectroscopy have been investigated. In the case of face-to-face contact type, the NIN (Normal metal-Insulator-Normal metal) structure was formed of a sandwich structure of thin oxide film (~ 50 Å) between sample and metal, but it is too difficult to control the oxidation of film and also the spectra are obtained for the average information all over the surface. In the case of a point contact type, the spectra would be obtained from some microscopic regions, but sample, tip and oxide film over the tip are easily damaged by contact pressure. Because the conventional methods have many uncontrollable factors (for instance, film thickness, contact pressure), reproducibility and reliability are always big problem. In this sense, the principle of STS which combines STM with tunneling spectroscopy, is very attractive. The insulator is just vacuum (~10 Å) and the tip is guaranteed not to touch sample. Moreover, the microscopic electronic structure is able to investigate because the tunneling region can be confined within atomic level. Therefore STS can give us many informations on materials. In the next place, the principle of the quantum mechanical tunnel effect will be explained briefly [11].

The current $I(V)$ and conductance $dI/dV = G(V)$ in structures, as shown in Fig. 1-4, which is flowing between two metallic electrodes separated by a narrow potential barrier $U(x)$, will be calculated. When the voltage is applied between two metals, the tunneling current begins to flow from one side to another side. In Fig. 1-4, the tunneling Hamiltonian H^T in the total Hamiltonian H,

$$H = H_1 + H_2 + H^1$$

which is then regarded as driving Hamiltonian for electron transition from one side (1) to the other (2). In the usual Fermi golden rule calculation W_{12} (transition rate) is given by

$$W_{12}(E_1) = \frac{2\pi}{\hbar}\left|\left\langle \psi_1 \middle| H^T \middle| \psi_2 \right\rangle\right|^2 \mathrm{N}_2(E_2)\delta(E_2 - E_1 - eV),$$

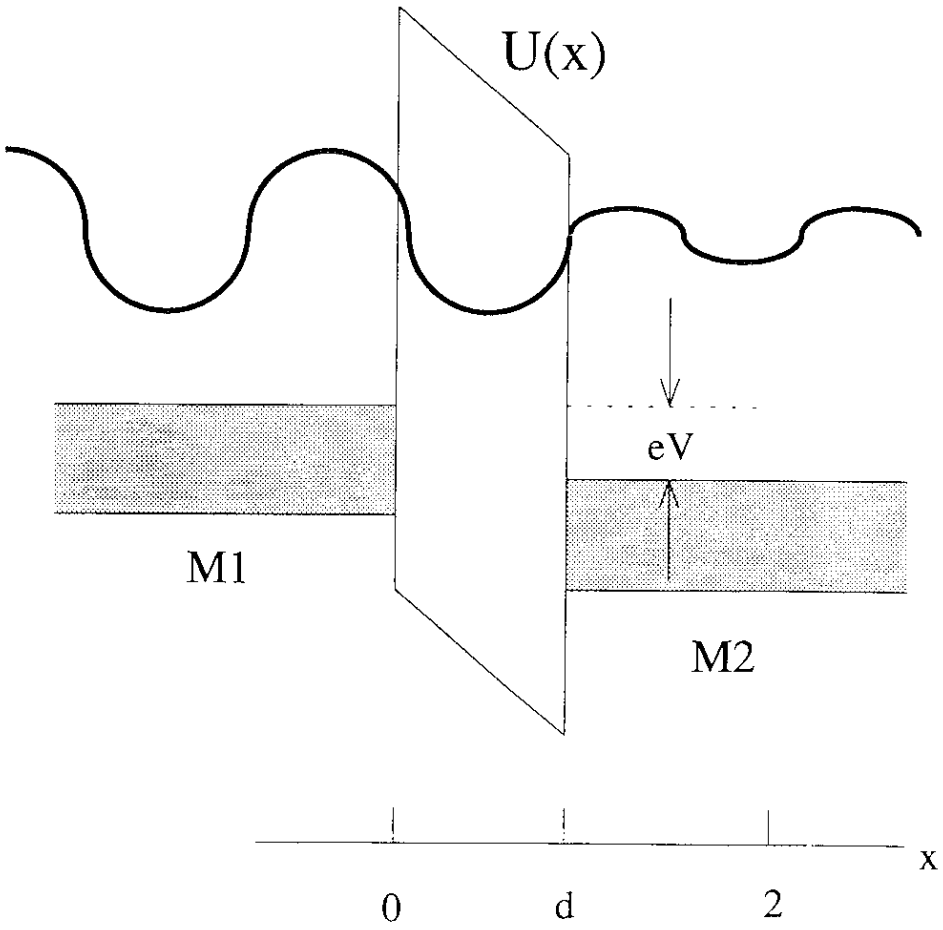

Fig. 1-4 Schematic energy diagram of tunneling effect.

where $W_{12}(E)$ describes the transition rate from a given state 1 to a set of states of equal energy and density $N_2(E_2)$ on the state 2, and $N_2(E_2)$ is the density of states at E_2 . Then the tunneling current from M_1 to M_2 is

$$J_{12} = \frac{4\pi e}{\hbar}\left|\left\langle \psi_1 \middle| H^T \middle| \psi_2 \right\rangle\right|^2 \int_{-\infty}^{\infty} dE_1 dE_2 N_2(E_2) N_1(E_1) \delta(E_2 - E_1 - eV) f(E_1)\left[1 - f(E_2)\right]$$

$$= \frac{4\pi e}{\hbar}|T|^2 \int_{-\infty}^{\infty} dE N_2(E+eV) N_1(E) f_1(E)\left[1 - f_2(E+eV)\right],$$

where $T \equiv \left\langle \psi_1 \middle| H^T \middle| \psi_2 \right\rangle$ and $f(E)$ is a Fermi distribution function. In the same way, the tunneling current from M_2 to M_1 is

$$J_{21} = \frac{4\pi e}{\hbar}|T|^2 \int_{-\infty}^{\infty} dE N_1(E) N_2(E+eV) f_2(E+eV)\left[1 - f_1(E)\right].$$

Therefore, the net current is given by difference between J_{12} and J_{21}:

$$J = J_{12} - J_{21} = \frac{4\pi e}{\hbar}|T|^2 \int_{-\infty}^{\infty} dE N_1(E) N_2(E+eV)[f_1(E) - f_2(E+eV)].$$

If the M_1 is a normal metal and can be regarded as $N_1(E) \sim N_1(0)$, the net current is written as

$$J = \frac{4\pi e}{\hbar}|T|^2 N_1(0) \int_{-\infty}^{\infty} dE N_2(E+eV)[f_1(E) - f_2(E+eV)]$$
$$= \frac{4\pi e}{\hbar}|T|^2 N_1(0) \int_{-\infty}^{\infty} dE N_2(E)[f_1(E-eV) - f_2(E)],$$

and differentiating the current with respect to voltage we have

$$\frac{dJ}{dV} = \frac{4\pi e^2}{\hbar}|T|^2 N_1(0) \int_{-\infty}^{\infty} dE N_2(E) \left[-\frac{\partial f(E-eV)}{\partial (eV)} \right].$$

In the case of $kT \ll E$,

$$\left[-\frac{\partial f(E-eV)}{\partial (eV)} \right] \equiv \delta(E-eV).$$

Hence, we get

$$\frac{dJ}{dV} \propto N_2(eV) \cdot |T|^2.$$

The final equation means that the differential of tunneling current for voltage is proportional to the density of state, $N_2(eV)$ at energy, eV. Therefore, if M_1 is a normal metal, the spectrum depends on the density of state of M_2.

In Fig.1-5 schematics of energy bands structure and corresponding I-V or dI/dV-V curves are shown. The cases of (a) and (b) are the case of two normal metals (NIN) and the current-voltage characteristic, respectively. On the other hand, the cases of (c)~(e) are for a normal metal and a single superconductor (SIN). At T=0 the superconductor has a gap of 2Δ at the Fermi level where there are no allowed states for single electron. Therefore, at a bias voltage across the junction of $eV_B < \Delta$, the electrons from the normal metal are unable to tunnel into the superconductor. At $eV_B = \Delta$, the electrons in the metal see a sharp rise in the density of state in the superconductor (at T=0 there is an infinite discontinuity in the density of state of a superconductor at Δ). The corresponding I-V curve is shown in (d), also dI/dV vs V curve is shown in (e). One can measure the energy gap and the density of state of the superconductor directly from this conductance curve.

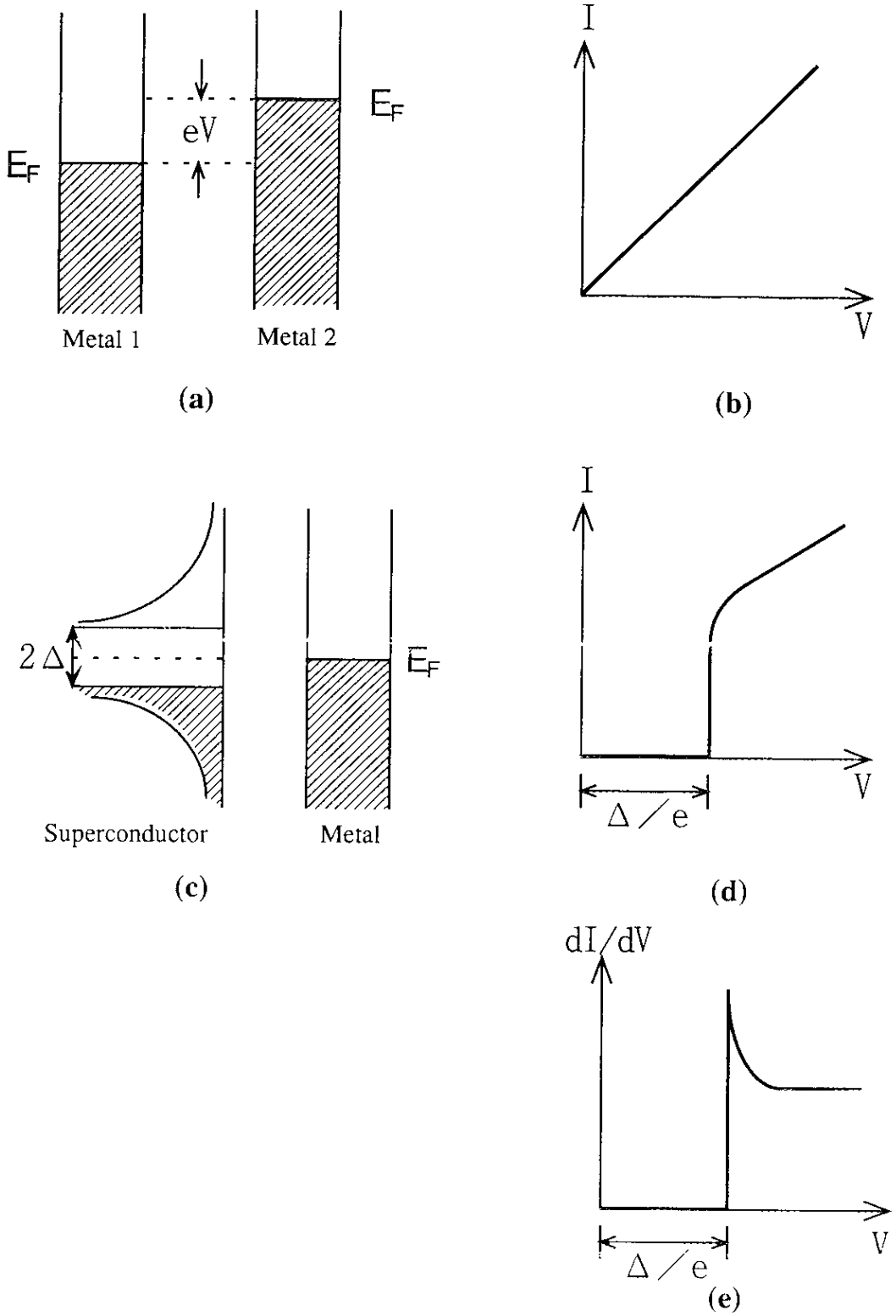

Fig. 1-5 The density of orbital and current-voltage characteristic for a tunnel junction.

References

[1] G. Bining, H. Rohere, Ch. Gerber and E.Weible: *Appl. Phys. Lett.*, **49** (1982)178.

[2] G. Bining, C. F Quate, and Ch. Gerber: *Phys. Rev, Lett.*, **56**(1986)930.

[3] Y. Martin and H. K. Wickramashinghe: *Appl. Phys. Lett.*, **50**(1987)1455.

[4] J. J. Saenz, N. Garcia, P. Grutter, E. Meyer, H. Heinzelmann, R. Wiesendanger, H. R. Hiber and H. J. Guntherodt: *J. Appl. Phys.*, **62**(1987)4293.

[5] C. M. Mate, G. M. McClelland, R. Erlandsson and S. Chiang: *Phys. Rev. Lett.*, **59**(1987)1942.

[6] R. Erlandsson, G. Hadziioannou, C. M. Mate, G. M. McClelland, and S. Chiang: *J. Chem. Phys.*, **89**(1988)5190.

[7] P. K. Hansma, B. Drake, O. Marti, S. A. Gould and C. B. Prater: *Science*, **243**(1989)641.

[8] B. D. Terris, J. E. Stern, D. Rugar and H. J. Main: *Phys. Rev. Lett.*, **63**(1988)2669.

[9] B. D. Terris, J. E. Stern, D. Rugar and H. J. Main: *J. Vac. Sci. Technol.*, **A8**(1990)374.

[10] C. C. Willams and H. K. Wickramasinghe: *Appl. Phys. Lett.*, **49**(1986)1587.

[11] K. Oshima, T. Mori, H. Inokuchi, H. Urayama, H. Yamochi and G. Saito: *Phy. Rev.*, **B39**(1989)11387.

[12] J. G. Bednorz and K. A. Müller: *Z. Phys.*, **B64**(1986)189.

[13] A. L. de Lozanne, S. A. Elrod and C. F. Quate: *Phys. Rev. Lett.*, **54**(1985)2344.

[14] R. V. Coleman, B. Drake, P. K. Hansma and C. C. Slough: *Phys. Rev. Lett.*, **55**(1985)230.

[15] J. R. Kirtley, C. C. Tsuei, Sung I. Park, C. C. Chi, J. Rozen and M. W. Shafer: *Phys. Rev.*, **B35**(1987)7216.

[16] S. Pan, K. W. Ng, A. L. de Lozanne, J. M. Tarascon and L. H. Greene: *Phys. Rev.*, **B35**(1987)7220.

[17] E. L. Wolf: *"Principle of Electron Tunneling Spectrodcopy"* , Oxford Univ. Press, (1985).

[18] J. G. Simmons: *J. Appl. Phys.*, **34**(1963)1793, 2581.

[19] J. Tersoff and D. R. Hamann: *Phys. Rev.*, **B31**(1985)805.

2. Instrumentation

2.1. Introduction

An STM is a powerful tool to observe surface structures and to measure tunneling spectra with atomic resolution. In order to achieve the atomic scale observation, it is crucially important to make an environmental disturbance as low as possible. In this direction, some improvements have been carried out, to reduce vibration, to cut off sound wave, to cool down for decreasing thermal noise, to achieve high S/N ratio of electric circuit, to make a good tunneling tip and so on. Figure 2-1, shows the relation between the resonance frequency of STM unit and vibration isolation system's[1]. It is necessary to realize the condition that the resonance frequency of STM unit is 100 times higher than the vibration isolation system's, at least. But there are actual limits for each of them, *i.e.* ~ 30 kHz upper limit for STM unit and ~4 Hz lower limit for vibration isolation system. Therefore the STM unit should be designed compactly and rigidly.

It is also very important for low temperature experiment to design a compact instrument because compact one has small thermal mass. Additionally, if the unit is very compact, it is possible to do experiment in the magnetic field by combining with slender dewar. In an experiment at low temperature, it is very difficult but important to decrease the electrical noise in a long cable between sample and preamplifier.

A tunnel probe tip should be very carefully checked, because it is impossible to obtain good STM image when the tip condition is poor. In this chapter, the STM system which was used for the room temperature experiments is elucidates in the first place. The design and construction of a low temperature STM are described in detail in the second part. Then the electronics for tunneling spectroscopy is explained. And finally, the method for making a good tip is stated.

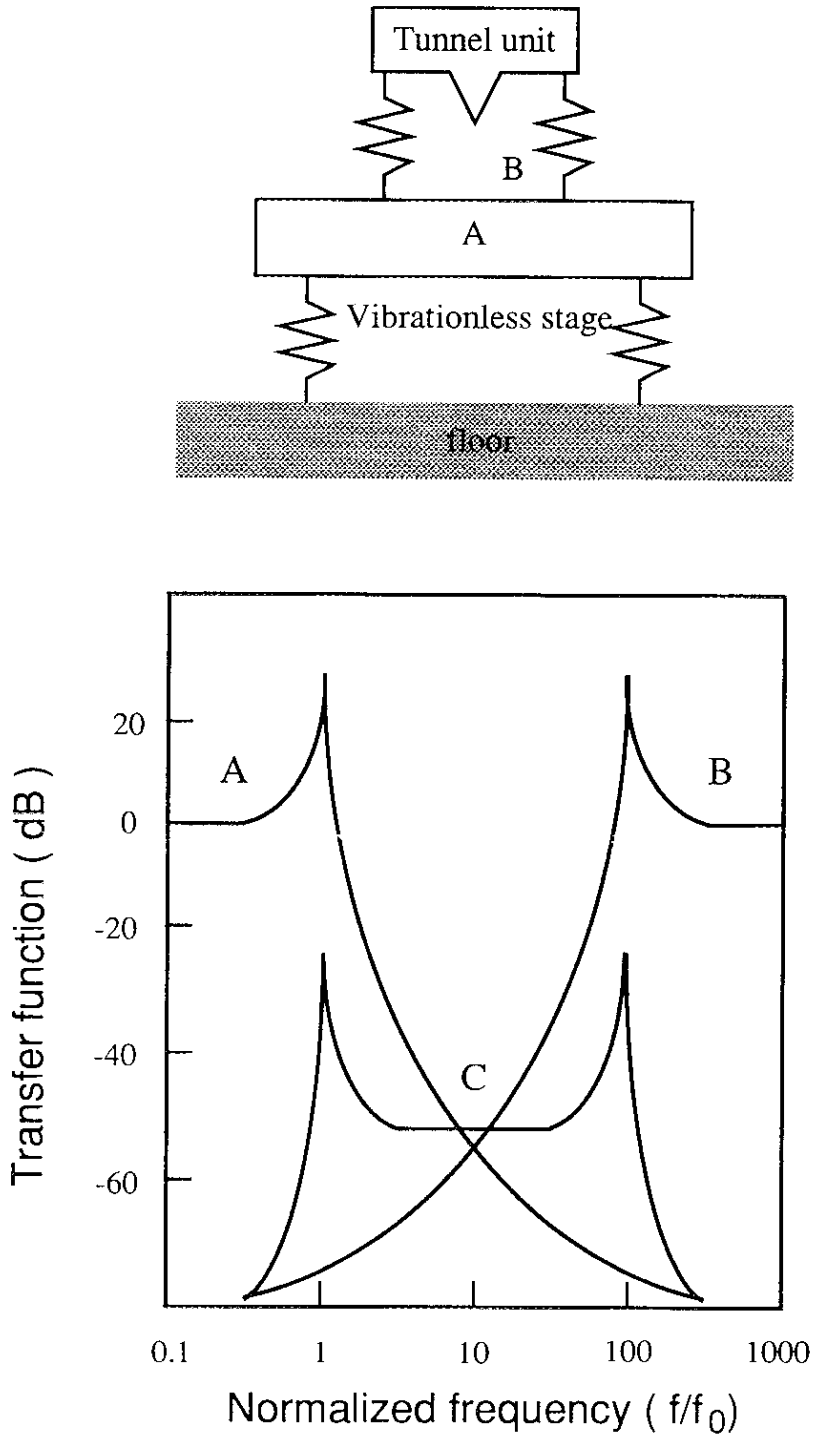

Fig. 2-1 Simplified model of vibration isolator and STM unit. The transfer function (A) defined for vibration isolator vs floor, (B) that defined for STM unit vs vibration isolator and (C) that defined for STM unit vs floor.

2.2. Scanning Tunneling Microscope[2]

The STM system, NanoScope II (Digital Instrument), consists of three major components, the microscope, the control unit and the computer workstation. A simplified schematic of the system is shown in Fig. 2-2.

The microscope consists of the piezoelectric scanner which is held by the head on the stage, the preamplifier mounted on the head, the base which supports the head and sample, the support structure for the base, the coarse adjust screws and the stepper motor to control the fine adjust screw. The scanner is tube type which has four electrodes (+X, +Y, -X and -Y) outside and one electrode (Z) inside, and controls 3D motion of the tunneling tip by the applied voltage (within ±220 V). The sensitivity of our piezoelectric tube for three directions (X, Y and Z) are 20.9 Å/V, 14.1 Å/V and 20.0 Å/V, respectively. The schematic electric

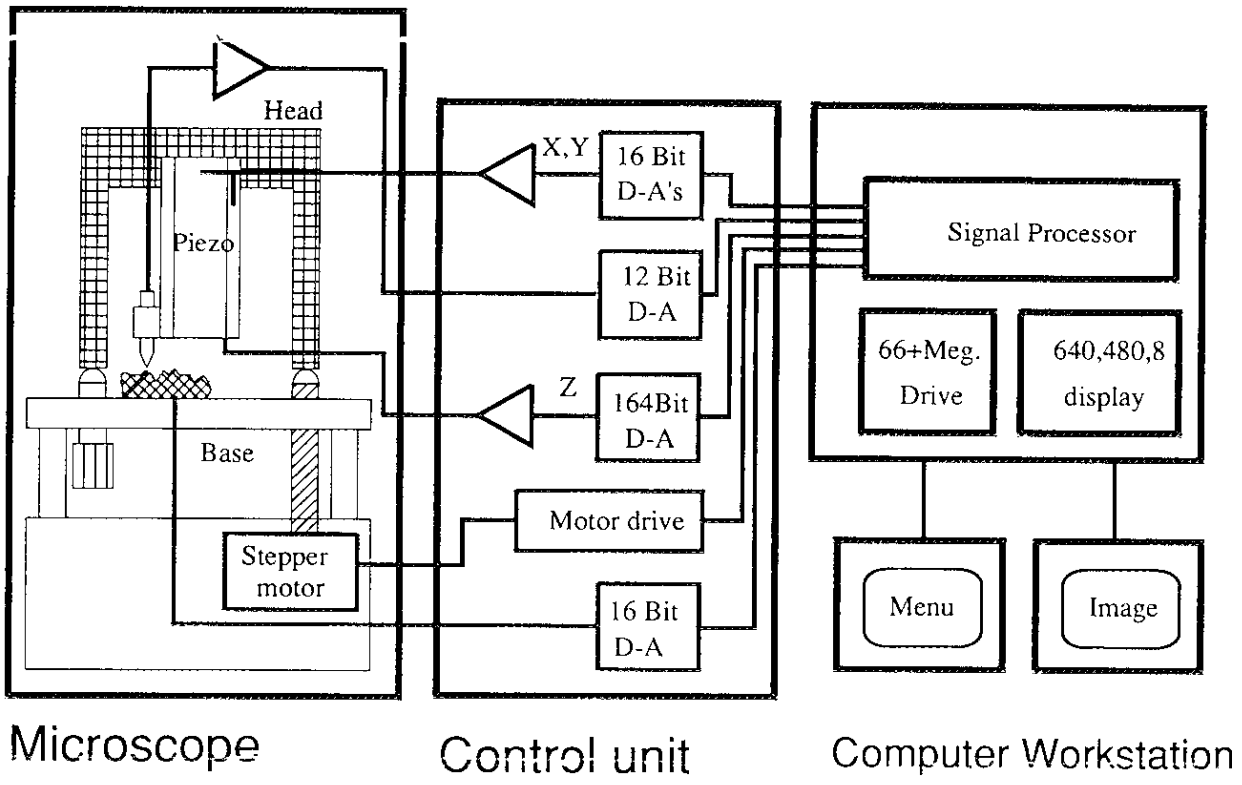

Fig. 2-2 The block diagram of RTSTM (NanoScope II)

circuit is shown in Fig. 2-3. The sample bias that is variable DC voltage is applied to the sample, then the tunneling current (typical current is ~1 nA) flows into the ground through the tip and the resistance (R_1: 1 MΩ). The voltage converted by R_1 is amplified 100 times (R_2: 1 kΩ, R_3: 100 kΩ).

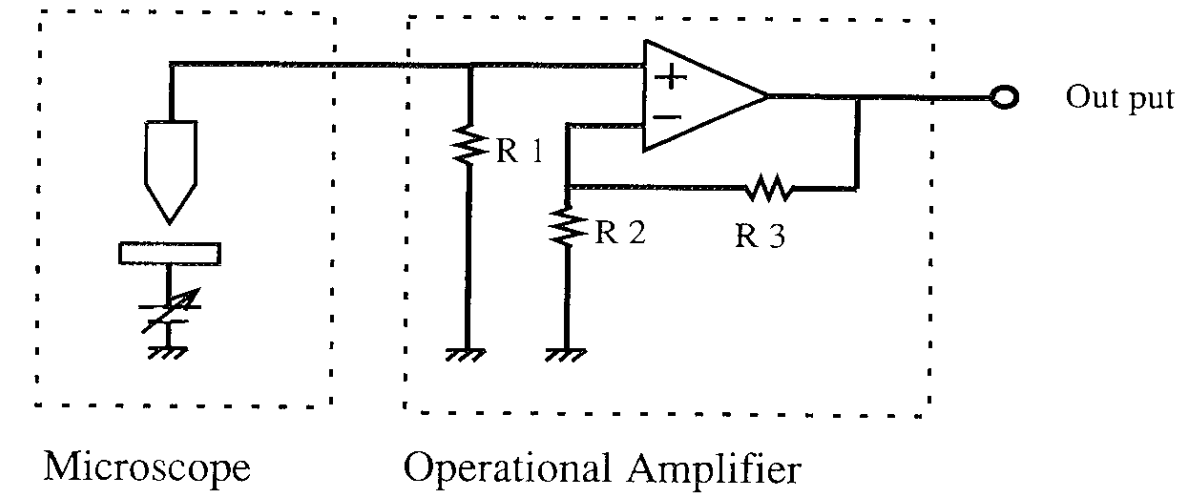

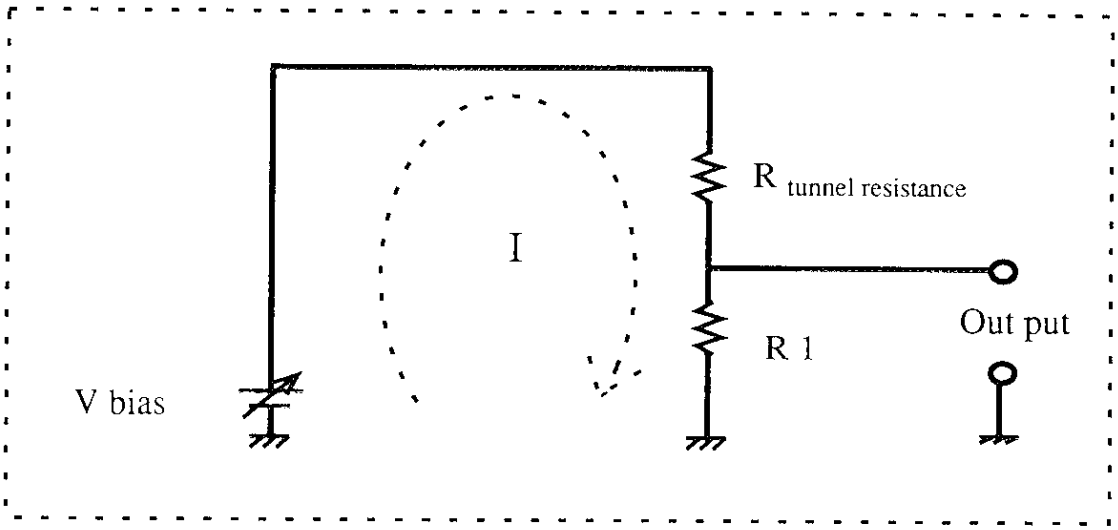

Fig. 2-3 The electronic circuit of operational amplifier for RTSTM.

The fine approach is achieved by the combination of lever, screw and step motor. The ratio of lever is 8:1. The screw goes ahead 0.32 mm per pitch and the step motor rotates 0.45 degree/step. Therefore, the tip moves to sample with 500 Å/step, as shown in the next equation.

$$\frac{1}{8}\times\frac{0.32\times10^{-3}}{1}\left(\frac{\text{pitch}}{\text{turn}}\right)\times\frac{1}{360}\left(\frac{\text{turn}}{\text{deg}}\right)\times0.45\left(\frac{\text{deg}}{\text{step}}\right)=500\left(\frac{\text{Å}}{\text{step}}\right).$$

Figure 2-4 shows microscope and vibration isolation system. The microscope should be isolated from sources of vibration in the acoustic, sub-acoustic frequencies and so on. This requirement can be relaxed somewhat for large scale images, but atomic scale work is very sensitive to ordinary room vibrations. In order to isolate the vibration, the microscope is based on a pad of soft silicon rubber that is slightly larger than the microscope base and about half an inch thick. Moreover, the microscope with the pad is put on the vibration isolation system which has a large mass. On the other hand, in order to isolate the air current and sound, the microscope is covered by a metallic cap. The whole system including microscope, pad and vibration isolation system is finally covered by the cage made of the sound-absorbing and sound-isolating material.

The control unit is an analog/digital interface of the system, acting as the gateway between the computer workstation and microscope. The computer workstation consists of the 80386 PC/AT-compatible computer, color graphics monitor, monochrome text monitor, video printer, dot printer and mouse. The microscope is controlled by the computer workstation.

The basic function of the instrument is to move the tip in an X-Y raster scan across a conducting sample while scanning the tunneling current between the tip and sample. A feedback loop uses the current as an input to control the height of the tip by applying a voltage to the scanning piezo (the Z drive voltage). The raster scan and the feedback loop are controlled by the digital signal processor (DSP) in the workstation. The DSP passes Z and/or current data to the 80386 processor (CPU) and graphics processor in the workstation for display or storage. The CPU sends operator commands for controlling the raster scan or feedback loop to the DSP. The operator has to control the tunneling current, the bias voltage

on the sample and the gain parameters of the feedback loop. The tip height is controlled by the feedback loop and/or spectroscopy software and is typically less than 10 Å.

If the tunneling current is input, new X, Y, and Z voltages are outgoing as a output at a sampling rate of 63 kHz (typical). The X and Y scan voltages are triangle wave outputs analogous to the horizontal and vertical scans on a CRT monitor. The scan frequencies and amplitudes can be varied by the operator. Offsets can be added to the scan voltages to move the scan to different areas of the sample surface. The scan voltages are carried from the control unit to the microscope by the flat ribbon cable and are connected directly to the electrodes on the piezoelectric scanner.

The feed back loop passes from the microscope through the control unit to the DSP and back again. The tunneling current from the microscope enters the control unit and is sampled at a 63 kHz rate, then converted to a digital binary representation and transmitted over by the flat ribbon cable to the DSP. The DSP then uses this value to calculate a new Z value that is transmitted back to the control unit where it is converted to an analog signal and amplified with a high voltage amplifier, and applied to the Z electrode of the microscope piezoelectric scanner.

The actual manual of operation is as follows:

1) Hold the sample on the base by a metal clip. When the sample is too small to hold, fix the sample on a copper plate with gold paste.

2) Insert a new tip into the tip holder on the piezo electric tube and mount the head onto the sample holder.

3) Adjust the two coarse approach screws until the tip comes within 0.25 mm from the surface as shown in Fig. 2-5. Try and adjust the screws such that the head is not tilted to one side or the other.

4) Set many parameters (tunneling current, bias voltage, feedback gain, scan size and so on) on the STM menu.

5) Engage.

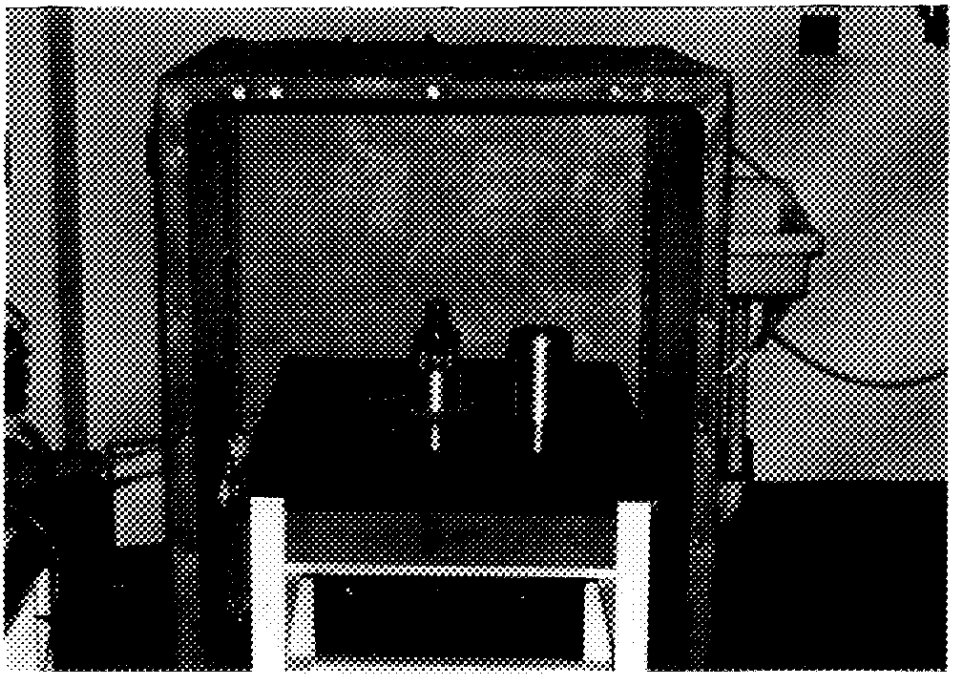

Fig. 2-4 The photograph of STM unit on the vibration isolation system.

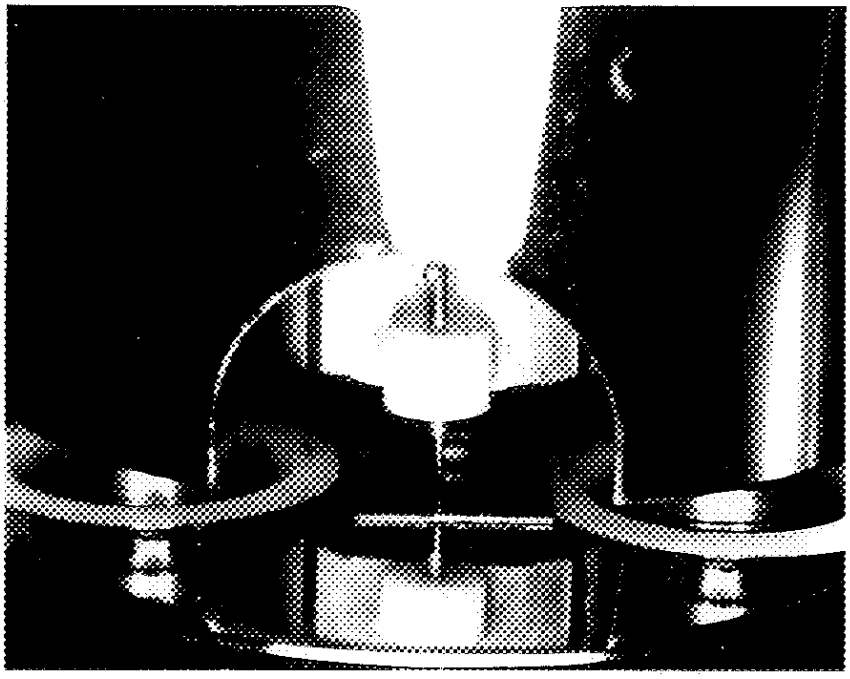

Fig. 2-5 The photograph is taken after coarse approach with an optical microscope of the tip/sample junction. The reflection image of the tip is seen on the graphite sample.

2.3. Low Temperature Scanning Tunneling Microscope (LTSTM)

LTSTM/STS is extremely useful for studying microscopic natures of a superconductor. Elrod was the first to develop an LTSTM and he used it to measure the spacial variation of the energy gap in Nb_3Sn[3]. This system had an STM mounted in a high vacuum can that was immersed in a liquid helium dewar. Since Elrod's initial report, seveal other groups have built and operated LTSTM [4],[5],[6]. Kirtley *et al.*[5], de Lozanne *et al.*[6] and Hasegawa *et al.*[7], have used an LTSTM to measure the energy gap in the high Tc superconductors. It is still very diffcult to get STM images at liquid helium temperature with atomic resolution and this performance has been achieved only by a few groups in the world.

Hasegawa *et al.*[8] observed STM images and tunneling spectra for cleavage plane (*ab* plane) of $Bi_2Sr_2CaCu_2O_y$ crystals, but they have not yet succeeded in STS along the perpendicular plane to *ab* plane. This measurement is crucially important to know the anisotropic nature of superconductivity in this kind materials. Bando et al. [9] constructed a LTSTM to observe the superconducting gap of $(BEDT\text{-}TTF)_2Cu(NCS)_2$, organic superconductor. In this case LTSTM/STS has also not yet accomplished. Each group has developed each own instrument rather independently and there has been no general consensus for the design of LTSTM/STS system yet. Kirk compared in his thesis [10] several types of LTSTM machines developed at Stanford University and he claimed that it was the need to adopt to new environment, just as in Darwinian evolution.

In our LTSTM machine the special features for designing are the following:

1. Compact and rigid-type.
2. High-performance piezo elements.
3. Ultra low noise circuits and cables.
4. "Fine" coarse approach with a diffrential screw.
5. FRP cryostat (without liquid nitrogen).
6. Operation in a magnetic field.
7. Electrochemical treatment for probe-tip.

The details of our system is described in the following part.

This section summarizes the design of our LTSTM system (~liquid helium temperature operation). The system consists of the control unit, the computer workstation, the tunneling spectroscopy system and the microscope unit. As for the control unit and the computer workstation we utilized the part of Nanoscope II STM of room temperature operation (see 2.2.). The tunneling spectroscopy system is described in the next section (see 2.4.). In this section, the microscope unit is explained in detail.

The schematic of the whole LTSTM system is shown in Fig. 2-6 and 2-7. As a cryostat is made of FRP (fiber-reinforced plastics) material, the heat insulating is very effective without the dual structure for liquid nitrogen. For example, it takes more than 30 hours until 3 liters liquid of helium evaporate up. And also, the bottom of the cryostat was designed as a slender type (OD = 90 mmϕ) to be able to do experiment in a magnet. In order to isolate the vibration, the cryostat was put on the rubber plate. The step motor to adjust a fine approach is fixed on the stage which is set on the flange. The step motor is controlled by computer, and rotates 0.05 degree by one step. Inside of the tube was evacuated to ~1×10^{-5} Torr by diffusion pump for a low temperature experiment. In this tube, there are six coaxial cables (+X, +Y, -X, -Y, Z and Ground), a thermocouple (AuFe-Chromel), heater, the driving shaft, and two carbon coated double shielded cables (Signal and Bias). The STM unit was hung to the tube by four springs to isolate the vibration.

The materials used for the STM unit are hestelloy (metal) and Macor (a machinable ceramics) whose thermal expansion coefficients are close to the piezoelectric element's. The unit which consists of a fine approach mechanism, a piezo holder, a piezo element, a tip holder, sample holder and a coarse approach mechanism, is designed compactly and rigidly with 20 mm in diameter and 110 mm in length as shown in Fig. 2-8. In order to realized the fine approach a differential screw was used whose pitches were 0.8 mm and 0.75 mm, respectively as shown in Fig. 2-9. The screw, therefore, pushes down the piezo holder with the rate of 0.05 mm/turn. As a result, the shift of the tip by one step is :

$$0.05\left(\frac{\text{mm}}{\text{turn}}\right)\times\frac{1}{360}\left(\frac{\text{turn}}{\text{deg}}\right)\times0.05\left(\frac{\text{deg}}{\text{step}}\right)=6.9\times10^{-9}\left(\frac{\text{m}}{\text{step}}\right)\approx70\left(\frac{\text{Å}}{\text{step}}\right)$$

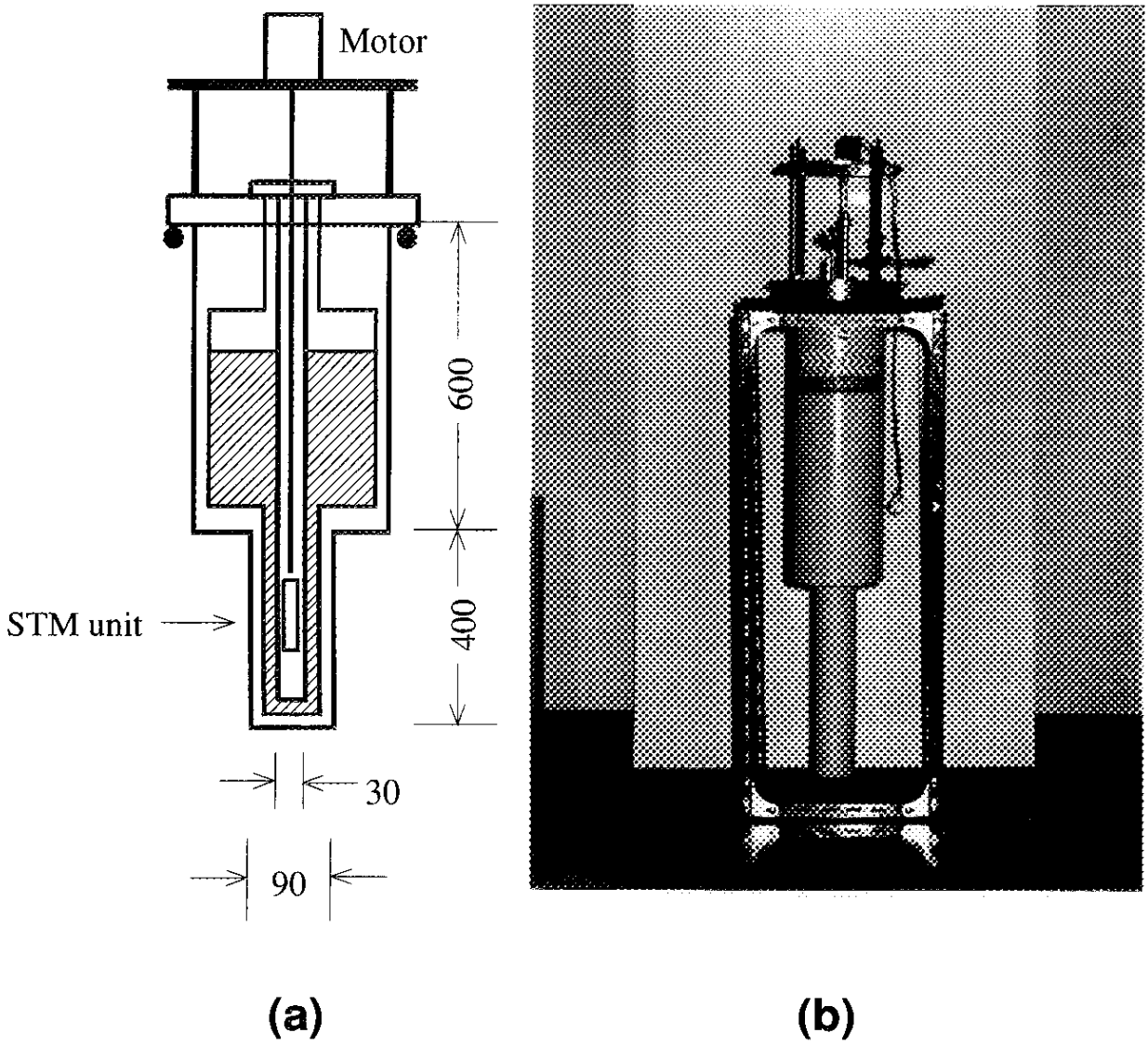

Fig. 2-6 The schematic of the whole low temperature STM system (a) and photograph of dewar (b).

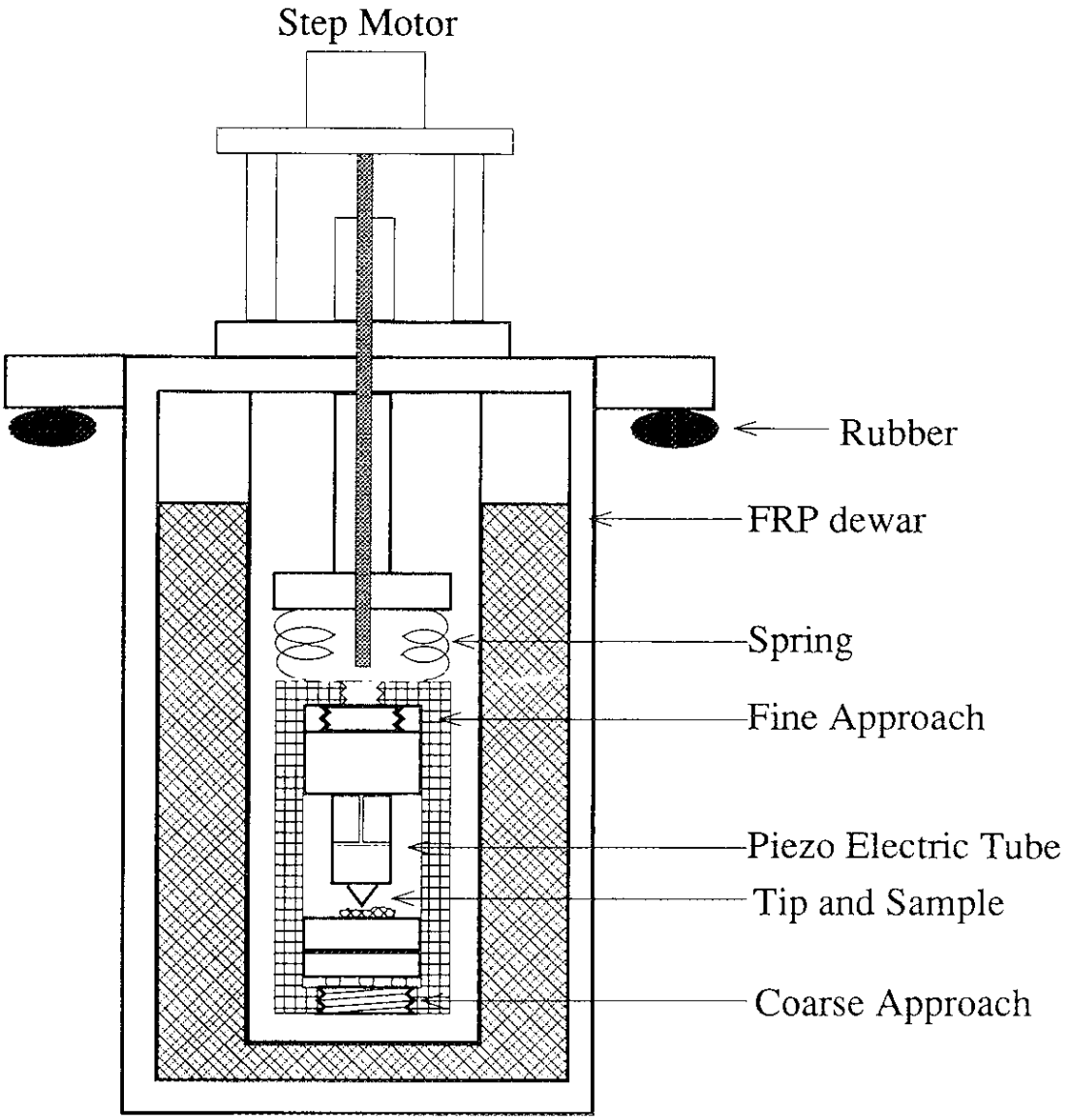

Fig. 2-7 The schematic of the microscope part of LTSTM.

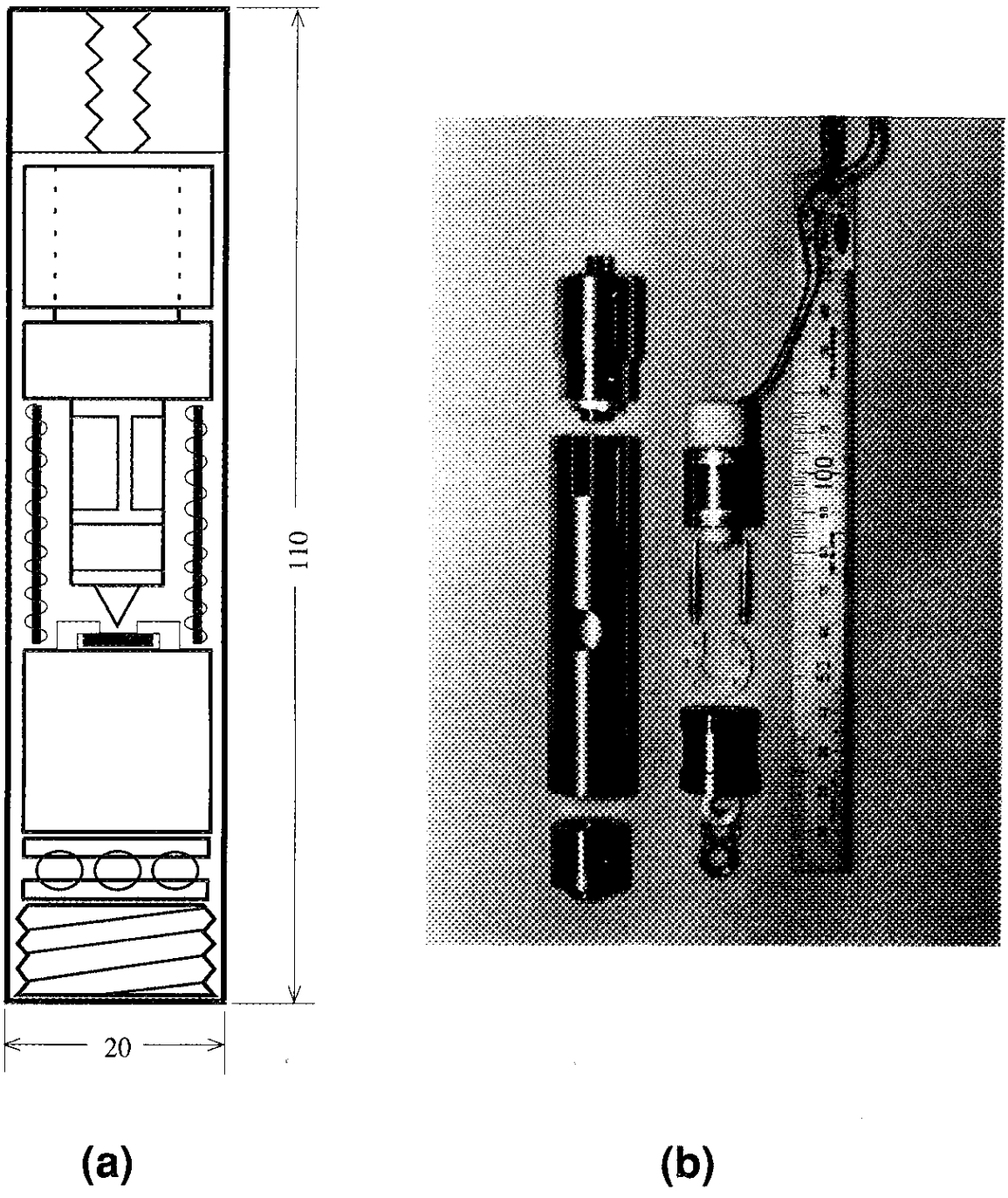

Fig. 2-8 The schematic of STM unit for low temperature system (a) and its photograph (b).

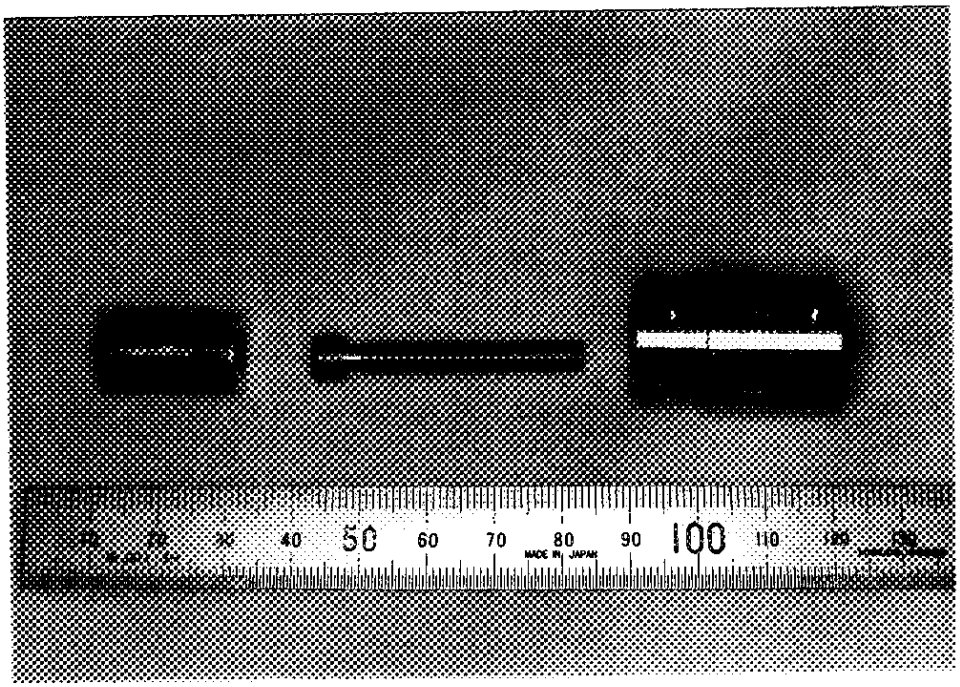

Fig. 2-9 Photograph of a differential screw for the fine approach . These pitches are 0.8mm and 0.75mm, respectively.

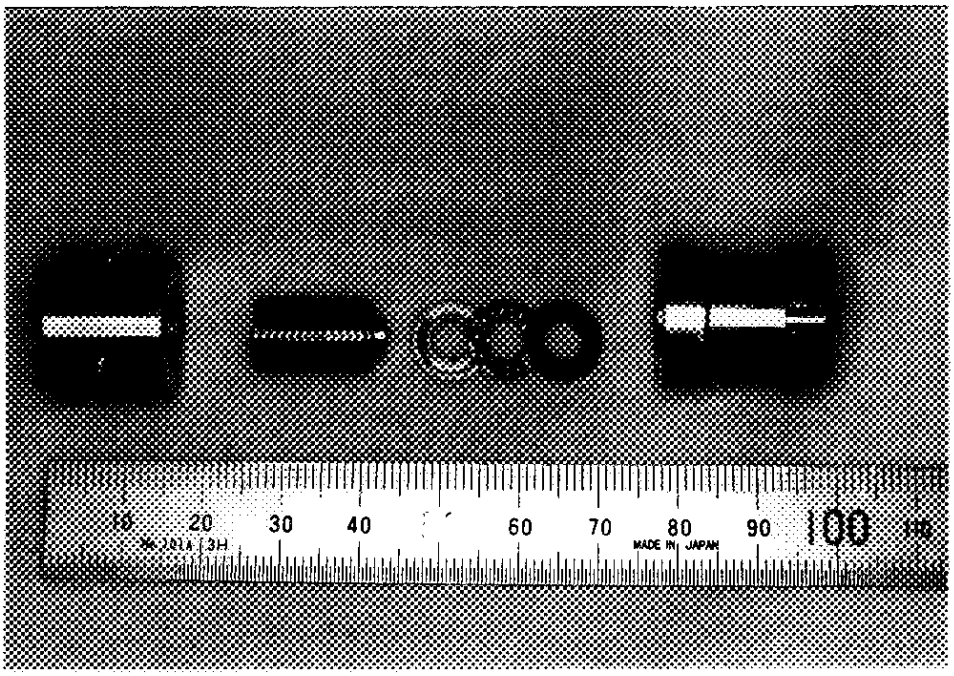

Fig. 2-10 Photograph of the coarse approach screw with 1.25mm pitch.

The piezoelectric tube was C-82 type (electrostriction constant ($\times 10^{-12}$ m/V): d_{31}=-260, d_{33}=540, d_{15}=750, resonance frequency ~150 kHz). The size is ID = 6 mm, OD = 8 mm (w=1 mm) and height (L)=20 mm (in Fig. 2-11.). The movable distance is given by :

$$\Delta L = d_{31} \times V \times L \div w = \frac{-260 \times 10^{-12} \times 200 \times 8 \times 10^{-3}}{1 \times 10^{-3}} = -416 \times 10^{-9} \approx -400(\text{nm})$$

with V=200(V). The maximum signal that can be applied without damaging the tube is 250 V/mm. The piezoelectric response is reduced by cooling from room temperature to 4K with a factor about one tenth. The fine approach mechanism at low temperature must be enough to bring the sample towards the tip with step size of ~400Å , to ensure that the tip does not crash into the sample.

On the outside surface of the piezoelectric tube, there are five electrodes +X, +Y, -X , -Y and Z, as shown in Fig. 2-11. There is one electrode for a ground terminal on the inside surface of the tube. The coarse approach system consists of the screw with 1.25 mm pitch and the ball bearing to prevent the sample holder from rotating during coarse approach (in Fig. 2-10.). The procedure for approaching the sample into tunneling range is quite simple. First, at room temperature, the coarse approach screw was rotated to reach within 5 μm from the tip with the aid of an optical microscope. The long tube in the STM unit was shielded by indium seal and pumped down to 1×10^{-5} Torr and finally filled with helium gas. It was cooled first in liquid nitrogen because the thermal mass of the system is large. The STM unit was cooled down to ~77K (liquid nitrogen) or ~4.2K (liquid helium), and the fine approach was carried out . A coaxial rod inside the tube can be rotated from outside of the dewar. The step motor controlled by computer rotates the coaxial rod until the assigned tunneling current starts to flow.

The electric circuit for tunneling current detection is shown in Fig. 2-12. There are some differences from the case of room temperature STM (RTSTM) which was shown in Fig. 2-3. The operational amplifier has three resistances to change amplification; R_3= 100 κΩ, 500 κΩ and 1 MΩ, respectively. Sensitivity was improved so that the amplification was a 100 times to 1000 times. In this case, the I-V converter which has a better element was put between the STM unit and the operational amplifier. The source of electric power for this

(a)

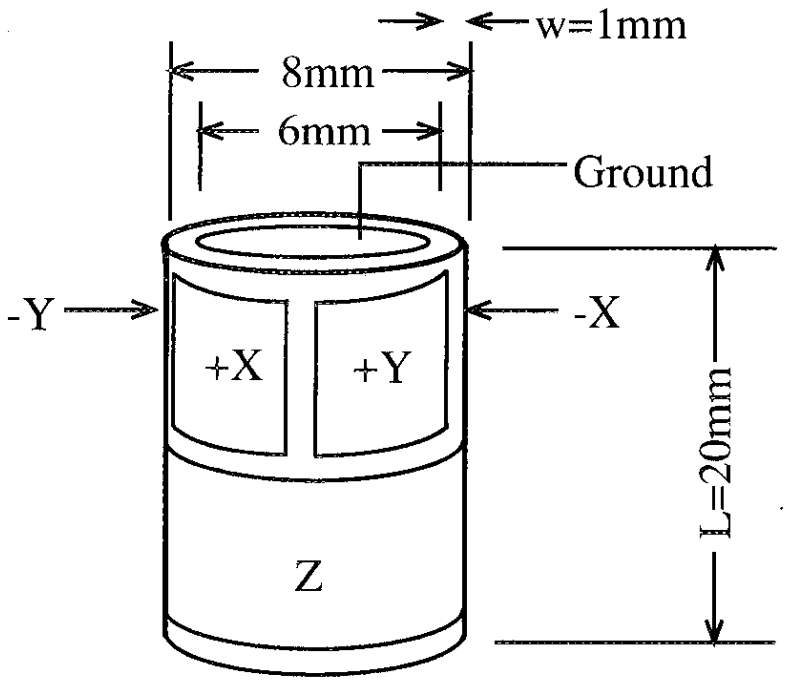

(b)

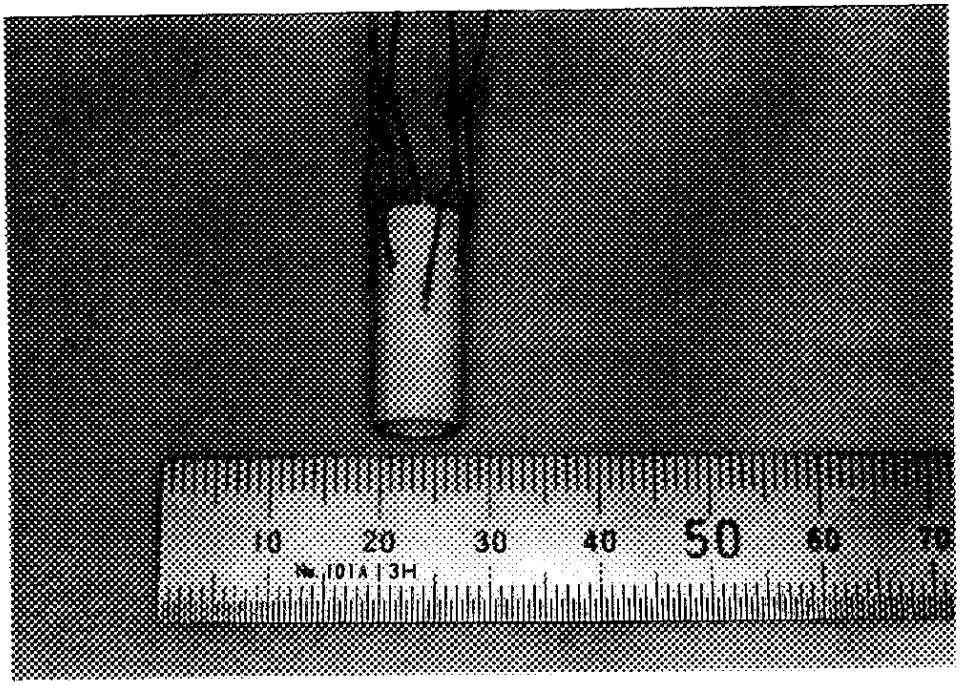

Fig. 2-11 The piezoelectric element of tube type (a) and its photograph (b). There are five electrodes outside and one electrode inside.

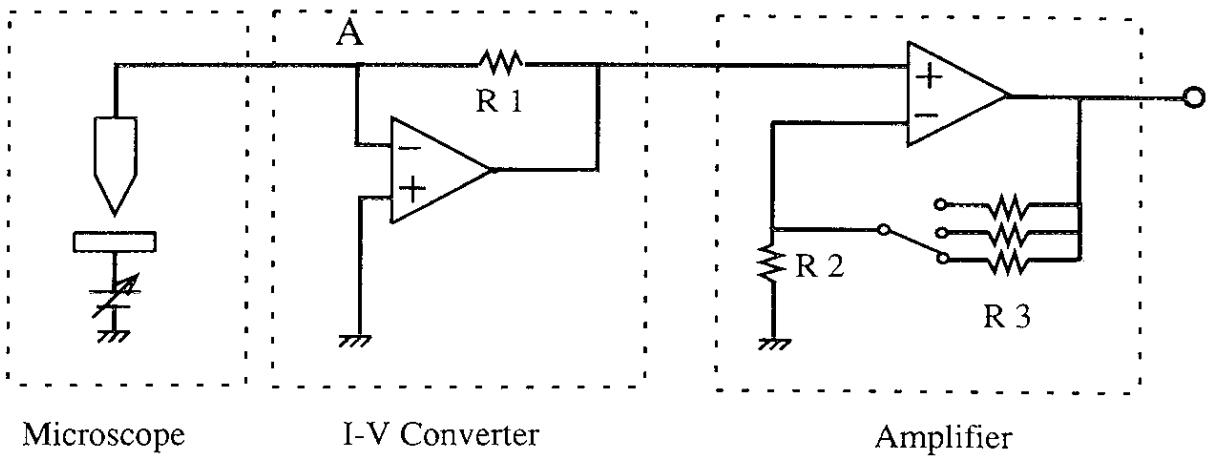

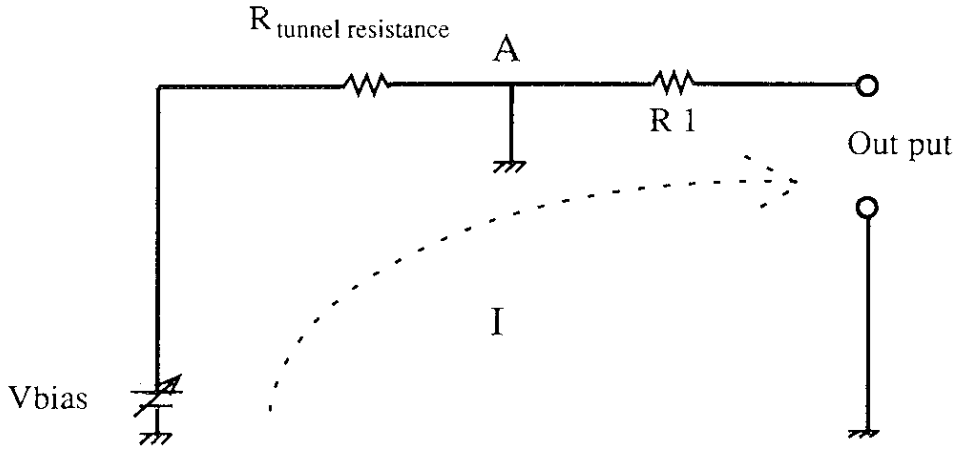

Fig. 2-12 The electronic circuit for tunneling current detection of LTSTM. These resistances value are R_2=1kΩ and R_3=100kΩ, 500kΩ and 1MΩ. Therefore amplification is a 100 times to 1000 times.

system was two dry batteries (9V) ,then the stability of electric source was much better than the RTSTM case in which rectified DC ± 15V from AC voltage was used. When the sample bias is V_{bias}, and the resistance to transform the tunnel current I into voltage is R_1, the sample voltage (V_{sample}) is

$$V_{sample} = V_{bias} - R_1 I \quad \text{(Fig. 2-3).}$$

Therefore, V_{sample} was under the influence of a voltage drop of $R_1 I$, and was unstable under the current image ,in particular. On the other hand, in the case of new circuit, as shown in Fig. 2-12 (b), A the sample voltage is

$$V_{sample} = V_{bias},$$

because the point A is virtual ground. The circuit is hard to be influenced by a high frequency wave.

Some STM images at low temperature were obtained by using the above system. Figure 2-13 shows the HOPG (see 3.2.) image at 77K(liquid nitrogen). The corrugation of carbon atoms was recognized, so we can say that the atomic resolution was achieved at low temperatures.

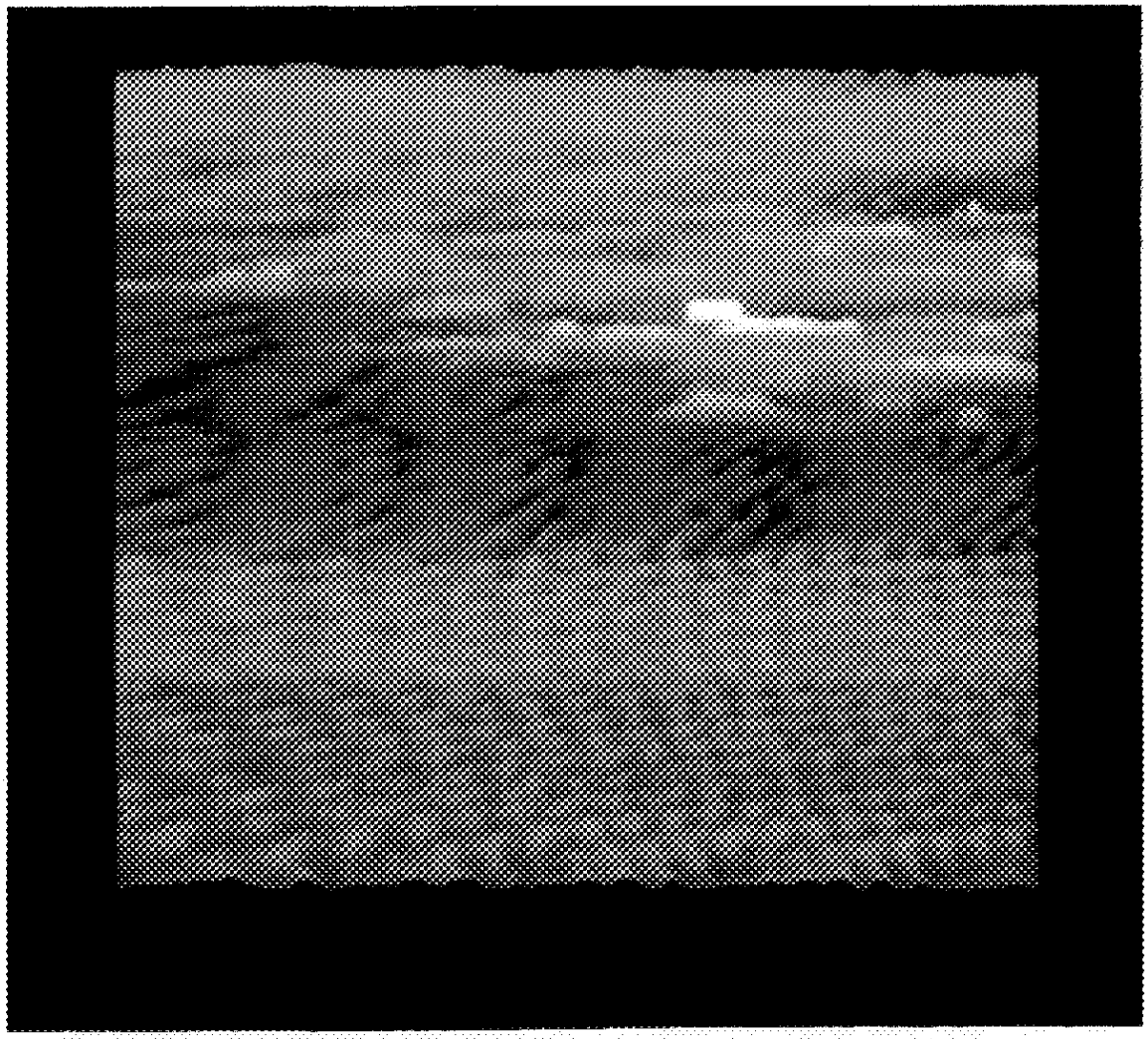

Fig. 2-13 The STM image of HOPG at low temperature. (~77K)

2.4. Electronics for Tunneling Spectroscopy

There have been many kinds of differential circuits that are of simple but high accuracy. One of the most famous one was developed by Hebard and Shumate [11]. In our system, the similar circuit which was designed by Nanba and Akimitsu [12] was used. In this circuit, switch capacitor filter: S.C.F. was used instead of a lock-in amplifier, but it has enough sensitivity for our experiment.

The principle of the differential circuit is shown in Fig. 2-14. In order to measure a conductance ($dI/dV = G$) at a point (A), alternating voltage (dV) is superimposed with DC voltage (V_{DC}), then

$V = V_{DC}+V_1\sin(\omega_0 t)$, and $V_1 << V_{DC}$.

The current through the tunneling gap (junction) can be developed in a Taylor series as

$$I(V)=G(V)\cdot V$$

$$I(V) \cong G(V_{DC})V_{DC} + G\Big|_{V_{DC}} V_1\sin(\omega_0 t) + \frac{1}{2}\frac{dG}{dV}\Big|_{V_{DC}} V_1^2\sin^2(\omega_0 t)$$

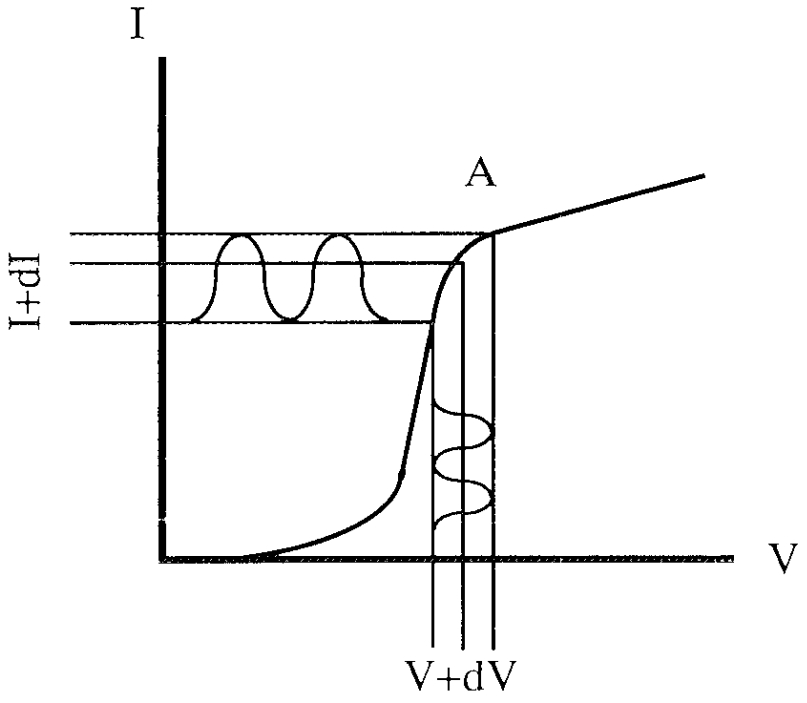

Fig. 2-14 The principle of the differential circuit.

where $G(V_{DC})V_{DC}$ is the direct current through the junction resulting from a dc bias voltage (V_{DC}), and $G|_{V_{DC}}$ is the differential conductance of the junction. In this system, because the dV is always controlled to constant value by the feedback circuit, the $G|_{V_{DC}}$ is proportional to the alternating current (dI).

The block diagram of this circuit is shown in Fig. 2-15. The dV signal (about 500 Hz) from an "oscillating circuit" passes the "voltage controlled amplifier: V.C.A.", and it is mixed with the super low frequency signal for sweep. The mixed signal applies the sample through the "current buffer". The voltage between both ends of sample is amplified by the differential amplification and is transferred to the dV detection circuit. The output voltage from the dV detection circuit is compared with standard voltage, and turns back to the V.C.A to keep constant value of dV on the sample. The output voltage of the differential

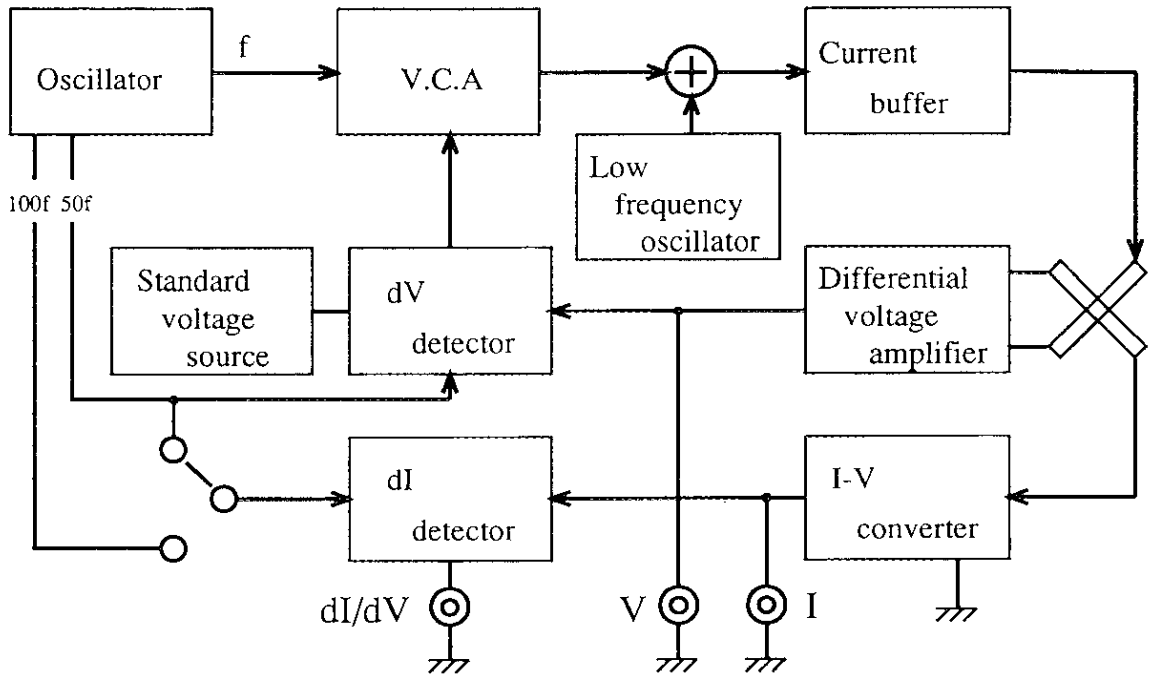

Fig. 2-15 The block diagram of the differential circuit.

amplification corresponds to the parameter (V) of X axis. The current through the sample is transformed to the voltage (I) by "I-V converter" and the divisional voltage (dI) is obtained by the dI detection circuit. It corresponds to the parameter of Y axis. By using an output for reference signal from the curcuit, a lock-in amplifier can be also used in order to increase the signal-to-noise ratio (S/N) of the measurement.

The speed of the sweep of the DC bias signal is determined by taking into account the frequency of the modulation voltage, time constant and the scannig voltage width. The width of changeable frequency was 0.001 ~ 100 Hz. The width of sweep voltage was 0 ~ 10 V. For the divisional voltage, the amplitude and the frequency were 0.1, 0.5, 1 and 5 %, for the width of sweep voltage and 1.5 ~ 400 Hz, respectively.

2.5. Electrochemical Etching of STM's tip

It is very important for an STM experiment to make a good tunnel probe tip, but it is very difficult to make a single atom tip. The wrong tip is often produced unstable and strange STM image. Even if the tip condition is stable, a double tip shape sometimes leads false images as shown in Fig. 2-16. In our case, several methods for preparation of tip were examined; those are mechanical cutting, mechamical polishing and electrochemical etching[13].

The easiest method for making a tip is the cutting off the wire by a cutting pliers. In this method, a good image with atomic resolution, *e.g.*, HOPG is sometimes provided. The scanning electron microscopy (SEM) images of the tip, are, however, not so fine, as shown in Fig. 2-17. The shape and surface are irregular and the shape of the tip-end is broad. This method may not always result in good stable images.

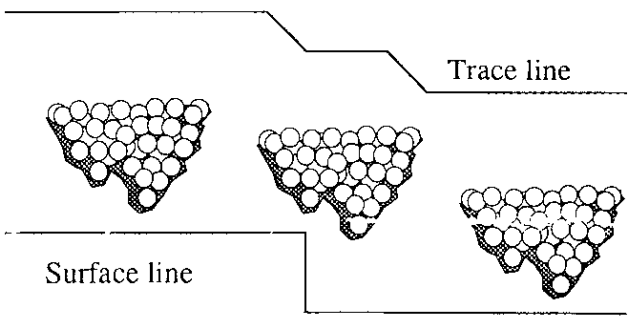

Fig. 2-16 The effect of double tip.

Mechnically polished tips somtimes give good quality images with atomic level topography but sometimes do not. This means that this method is unreliable. The Digital Instruments supplies this type of tip commercially. The SEM images of this Pt/Ir tip (Digital Instruments), are shown in Fig. 2-18. The shape of tip is sharper than the above-mentioned tip. Although the tip end image is very rough and the radius of curvature is not small.

In contrast to above two methods, the electrochemical etching Pt/Ir tip gave fairly better SEM images as shown in Fig. 2-19. The tip surface looks rigid and smooth. It has a longer slender portion near the tip-end of which shape is so sharp that the radius of curvature is ~ 500 Å. Observed STM images were much better and more stable, so we mainly used this

(a)

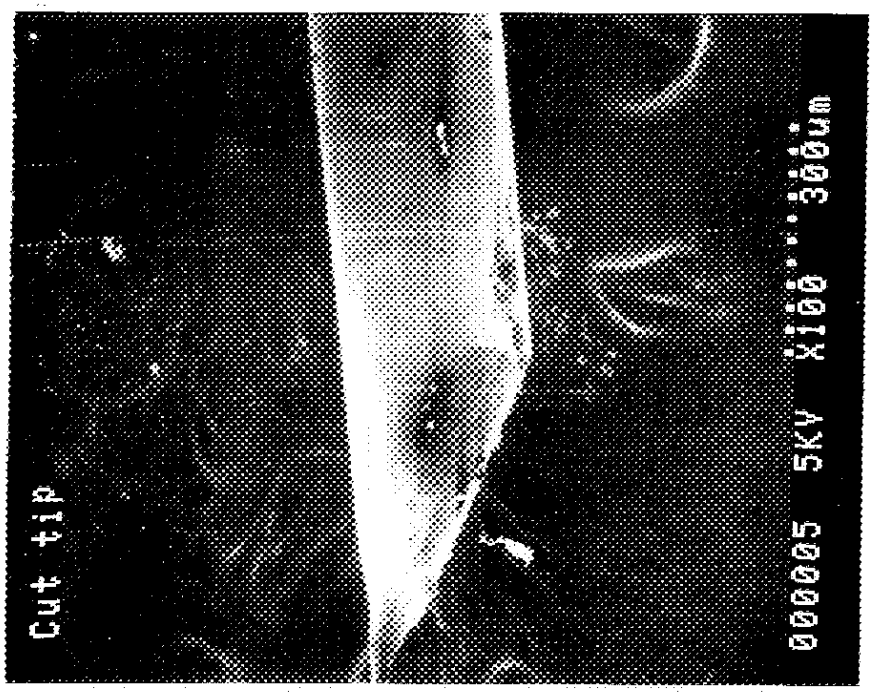

(b)

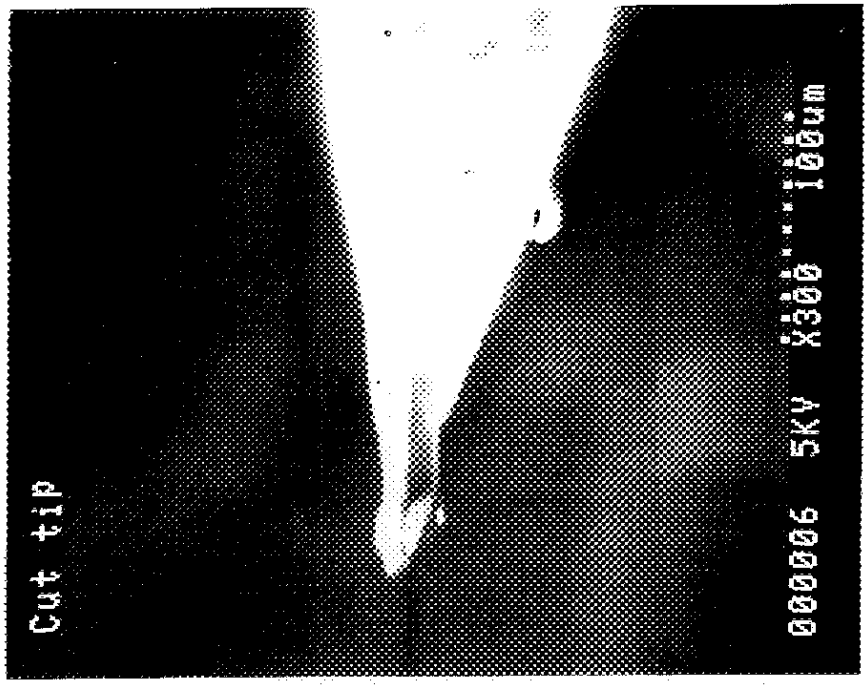

Fig. 2-17 SEM images of cut tip with magnifications of 100 (a) and 300 (b) times.

(a)

(b)

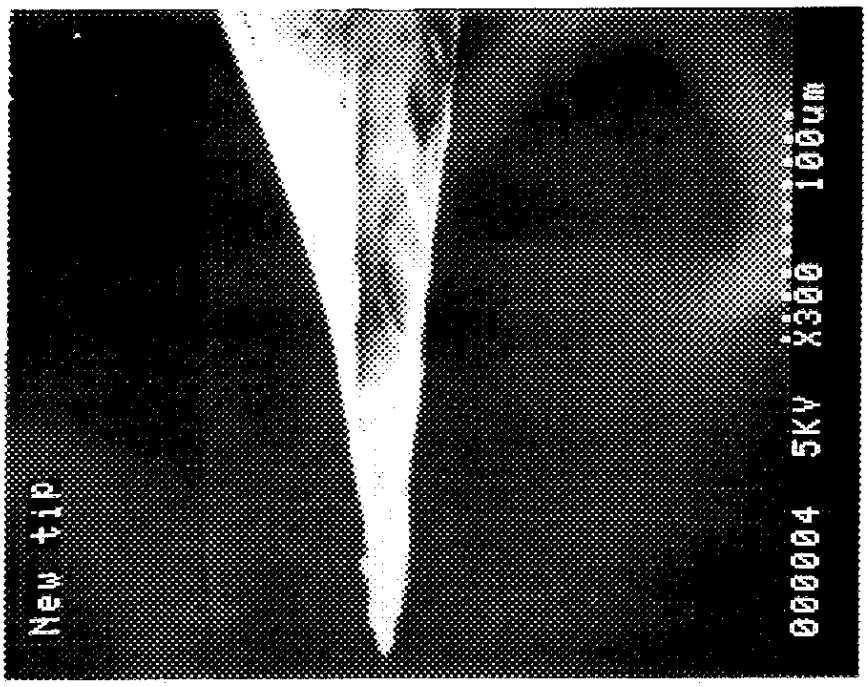

Fig. 2-18 SEM images of mechanically polished tip with magnifications of 100 (a) and 300 (b) times.

(a)

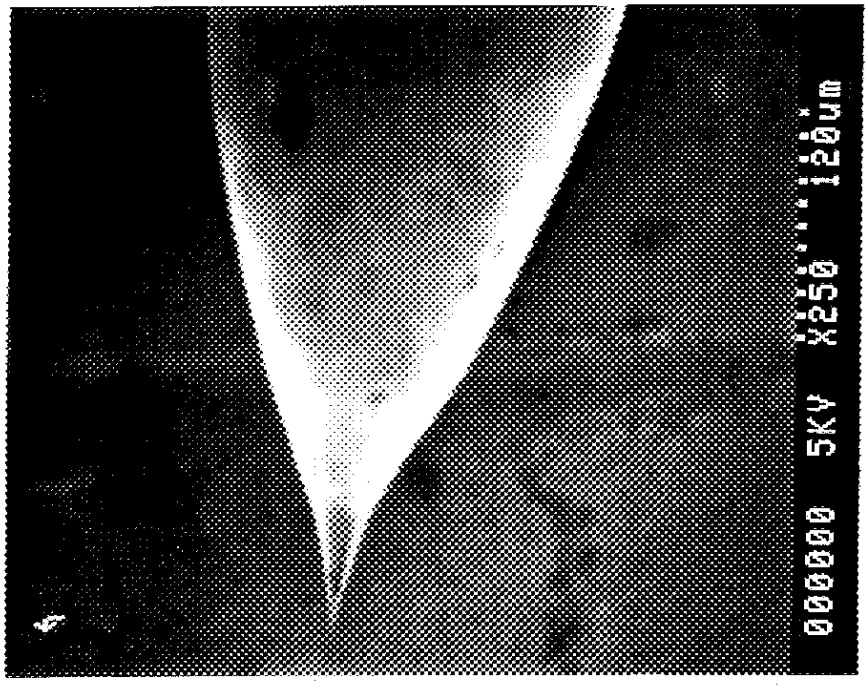

(b)

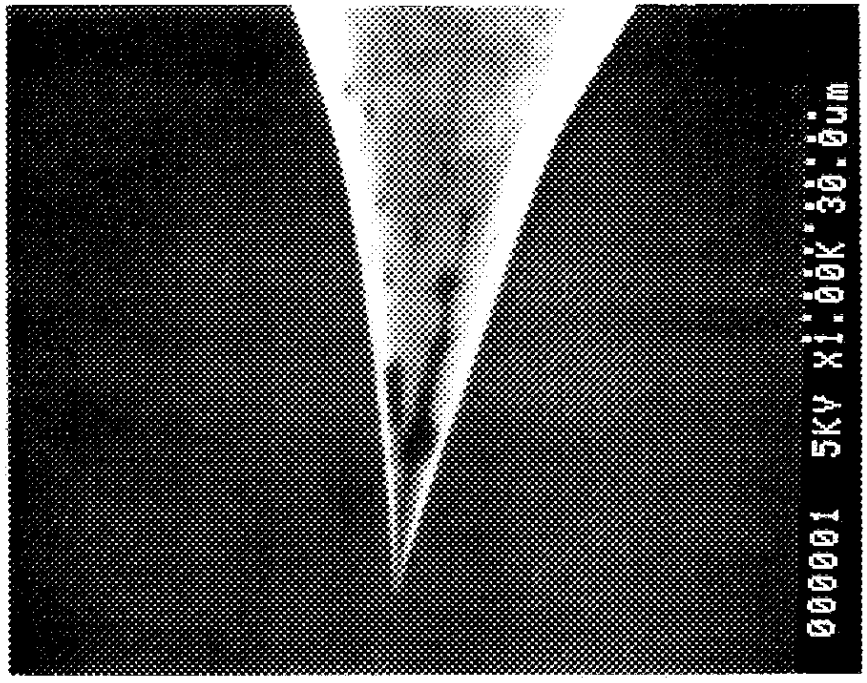

Fig. 2-19 SEM images of electrochemically etched tip with magnifications of 250 (a) and 1000 (b) times. The radius of curveture is ~500 Å.

types of tip in this work.

The schematic of electrochemical etching method was shown in Fig. 2-20. The 80:20 Pt/Ir wire of 0.3 mmϕ was used and it was dipped by ~1.5 mm into 60 ml of etchant solution consisting of saturated $CaCl_2/H_2O/HCl$(60%/36%/4% in volume). The Pt/Ir wire was etched against a carbon rod at 25V rms. ac for ~5 min. until bubbles from the tip ceased emerge. The etchant must be periodically refreshed since the attack deteriorates as the chloride ion concentration was depleted with the formation of a platinum chloride complex. After etching, the tip is rinsed in distilled water to remove the residual etchant solution.

Other than the Pt/Ir tip, tungsten tip was sometimes used. In the case of W tip, good tips were made by almost similar etching method, but were used different solution that is 1 molar KOH using distilled water[14]. The W wire is easily etched compared with Pt/Ir wire. Although, the tip is not recommended because the tip is more easily oxidized than Pt/Ir tip.

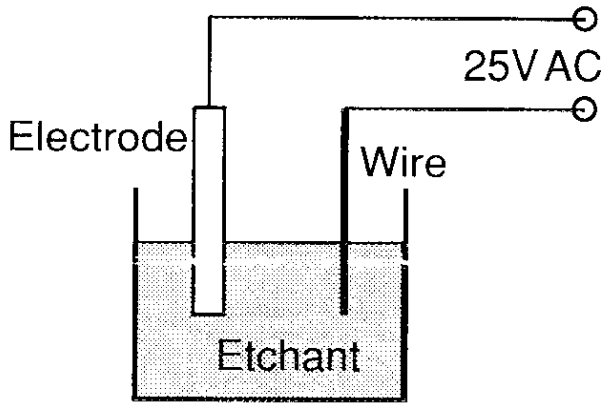

Fig. 2-20 The schematic of chemical etching.

2.6. Conclusion

In order to obtain good STM image with atomic resolution, a lot of care should be taken to isolate many noise sources in the environment. As a result of considering of some counterplan for noise, it was understood that various kind of vibrations, tip condition and surface condition of the sample are the most influential factor for noises. It is particularly important to make a good tip. Electrochemical etching method was most successful to get a good tip, even if it is not always successful. More relevant etching method should be developed, in order to obtain better STM images.

In the LTSTM system, the noise sources increased, in particular, the vibration by bubbles of cryogen and the electrical noise due to longer cable between sample and operational amplifier. As a result of several improvements, the total S/N ratio was enhanced, and tunneling spectra at low temperatures have been successfully measured. It is, however, still not so easy to obtain a stable STM image at low temperature. The most difficult point to develop LTSTM is that there is no general principle or way for stable operation, and we have to solve each problem case by case. In our case at the present stage we should extend the length of sample holder for more stable operation at liquid helium temperature. Such extension may issue another noise problem, and then we have to overcome it, and so on.

References

[1] M. Okano, K. Kajimura, W. Mizutani, M. Ono, S. Wakiyama and F. Sakai: *J. Vac. Sci. Technol.*, **A5**(1987)3313.

[2] A. F. Hebard and P. W. Shumate: *Rev. Sci. Instrum.*, **45**(1974)529.

[3] Instruction Manual of NanoScope II by Digital Instruments.

[4] A. L. de Lozanne, S. A. Elrod and C. F. Quate; *Phys. Rev. Lett.*, **54**(1985)2344.

[5] R. V. Coleman, B. Drake, P. K. Hansma and C. C. Slough: *Phys. Rev. Lett.*, **55**(1985)230.

[6] J. R. Kirtley, C. C. Tsuei, Sung I. Park, C. C. Chi, J. Rozen and M. W. Shafer: *Phys. Rev.*, **B35**(1987)7216.

[7] S. Pan, K. W. Ng, A. L. de Lozanne, J. M. Tarascon and L. H. Greene: *Phys. Rev.*, **B35**(1987)7220.

[8] T. Hasegawa, H. Suzuki, S. Yaegashi, H. Takagi, K. Kishio, S. Uchida, K. Kitazawa and K. Fueki: *Jpn. J. Appl. Phys.*, **28**(1989)L179

[9] H. Bando *et at.*; *"The Physics and Chemistry of Organic Superconductors"* ed. by G. Saito, (Springer-Verlag, 1990) p.167.

[10] M. D. Kirk: Doctor Thesis, Stanford Univ. (G. L. No. 4543)1989.

[12] T. Nanba and J. Akimitsu: *Kotaibuturi*, **20**(1985)20 [In Japanese].

[13] I. H. Musselman and P. E. Russell: *J. Vac. Sci. Technol.*, **A8**(1990)3558.

[14] Y. Liang, W. E. Packard, Z. W. Fu, H. A. Blackstead, K. K. Chin, J. D. Dow, J. K. Furdyna, W. M. Hu, R. C. Jaklevic, W. J. Kaiser, A. R. Pelton, M. V. Zeller and J. Bellina. Jr: *J. Vac. Sci. Technol.*, **A6**(1988)445.

3. Surface Structure Observed by STM

3.1. Introduction

Since the discovery of STM, it has become a most powerful tool in the study of surface science. The reason is not only its high resolution but also the difference of method taking image between electron microscopy and STM. In the case of electron microscopy, it is only possible to observe in vacuum, and a sample surface is damaged by collision of free electron. On the other hand, STM can be used not only in vacuum but also in air, in water or in gas, and a sample surface is not damaged. The bias voltage is less than workfunction, that is, it is 1mV~1V. Because the tunnel current is 1nA~10nA, electric power is 1pW~10nW. The low power prevents samples from damaging. Assuming that tunnel current flows through one atom at the end of the tip, the density of current is $\sim 10^{7}$ A/cm^{2}. In this case, the velocity of electron is $\sim 6\times 10^{9}$ number/sec and the time of passing tip for an electron is 2×10^{-10} sec. The time is longer than scattering time of electron in solid (10^{-14}~10^{-13} sec). As a result, the temperature of sample surface does not increase by observation.

Therefore the surface observation has carried out not only for inorganic materials, but also for organic materials and biological samples as DNA[1], liquid crystal[2],[3], phthalocyanine[4], high conductive organic crystal such as BEDT-TTF salt or proteins. In this chapter, studies on surface structures of some important functionality materials at room temperature will be described. At first, highly oriented pyrolytic graphite (HOPG) which is usually used as a standard sample and substrate in STM experiments, was observed. The next section, single crystals of six types BEDT-TTF salts which are known to be layered structure organic conductors or superconductors were studied. Moreover, C_{60} films evaporated on HOPG by MBE technique were observed. The C_{60} molecule is taken interest in the process of growth on substrate because the molecules rotate in bulk at room temperature. In addition, phthalocyanine films made by spin coat method were observed. The sample had high resistance itself and moreover, the film was not enough thin for STM

experiment. It is expected that to obtain the STM image of this films are very difficult and need some contrivance.

3.2. Highly Oriented Pyrolytic Graphite (HOPG)

The crystal structure of graphite is shown in Fig. 3-1. In this figure, it is recognized that the six carbon atoms form hexagon like a benzene ring, and spread all over the plane as a honeycomb. In this plane, there are strong sigma (σ) bonds and pi (π) bonds. On the other hand, in the side view of graphite, the distance between first layer and second layer is 3.37 Å. It is easy to cleave plane (0001) of graphite and to make a clean surface because the bonding force between layers is weak van der Waals force. Therefore, the graphite has been used as a standard sample for the STM observation.

In this figure, there are three types for carbon atoms (α,β,γ). A carbon atom in the first layer which is just above a second layer's atom is called " α atom". A carbon atom below which no carbon atom is present in the second layer is called " β atom". The carbon atom in the second layer which is below the center of a hexagon in the first layer is called " γ atom".

In Fig. 3-2, one dimensionai carbon image is shown along X-axis of HOPG. The amplitude of the corrugation was 1.6 Å. By spreading this line scan image along Y-axis, a two dimensional image was obtained as shown in Fig. 3-3. Moreover three dimensional surface image, as shown in Fig. 3-4, was obtained by computer graphics. In this figure, the scan size was 10 Å $\times$ 10 Å and sample bias and tunneling current were -20 mV and 1nA, respectively, and the bright parts correspond to carbon atoms. The distance from peak to peak is 2.4 Å and it is different from real atomic distance (1.42 Å). If the crystal structure of graphite overlapped with this image, it is recognized that, only three carbon atoms among six atoms of a benzene ring can be seen in the STM image. The reason is the following [5]: The tunneling current of STM is predominantly determined by the density of state near the Fermi surface. In the case of graphite, there is π band around Fermi level and the state of density of the band is very effective for the tunneling current. At the position of α atom, the π band may split from the Fermi surface into the bonding orbital and the anti-bonding orbital by the interaction between this atom and second layer's atom. As a result, it is easier for tunneling current to flow into the β atom than to the α atom. It is most difficult to flow into γ atom.

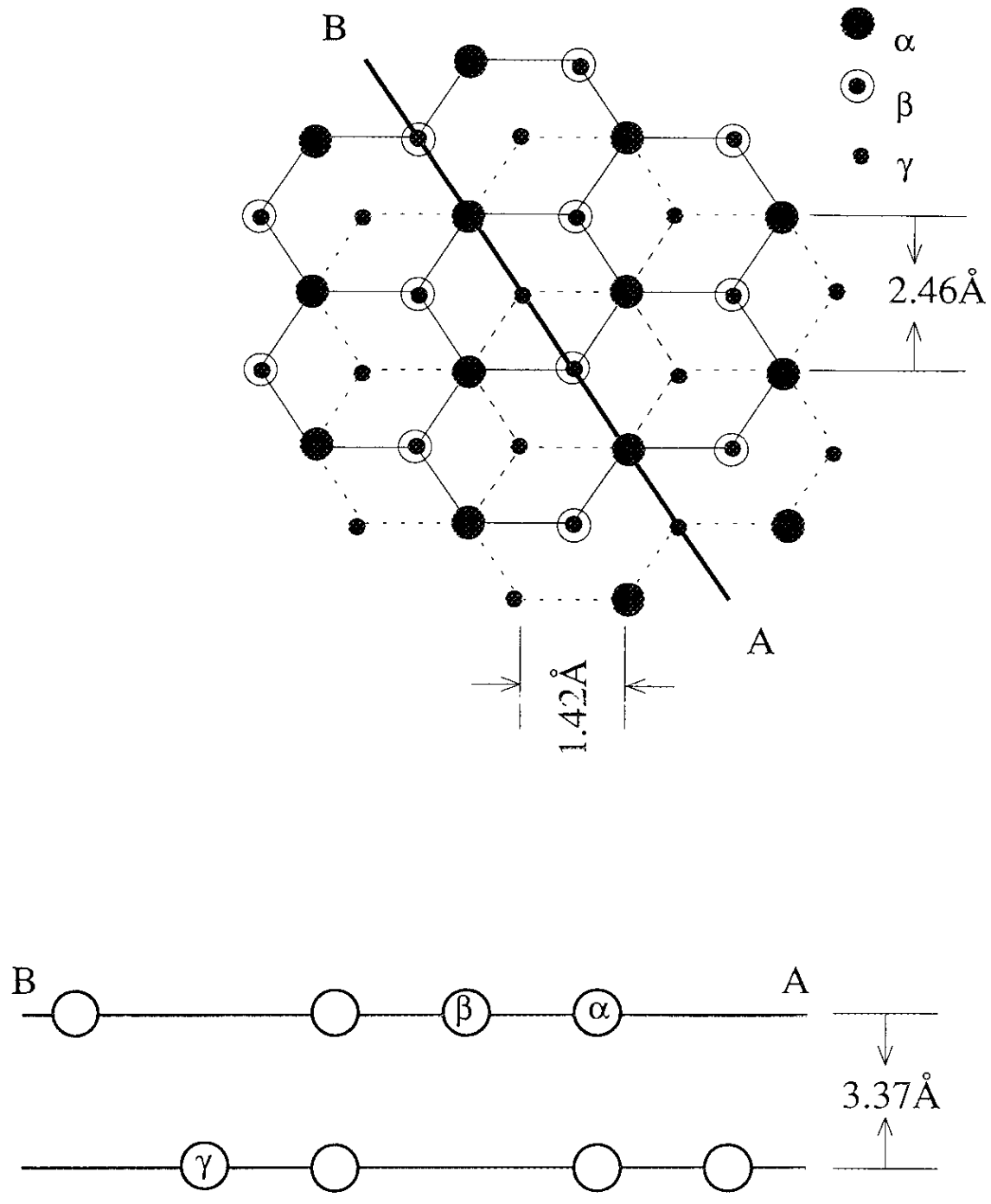

Fig. 3-1 The crystal structure of graphite and sectional side view along A-B. There are three type positions (α, β, γ).

Therefore, in the case of graphite, only β atom can be seen by STM, and the STM image shows triangle lattice with 2.46 Å period.

Figure 3-5 shows larger scan image for HOPG. In this figure, scan size was 100 Å × 100 Å, and applied bias voltage and tunneling current were -20 mV and 1 nA, respectively. The regular arrangement of carbon atoms can be seen. The two dimensional spectrum filtered by fast Fourier transform (FFT) for this image is shown in Fig. 3-6. In this figure, the hexagonal spots for HOPG are clearly recognized.

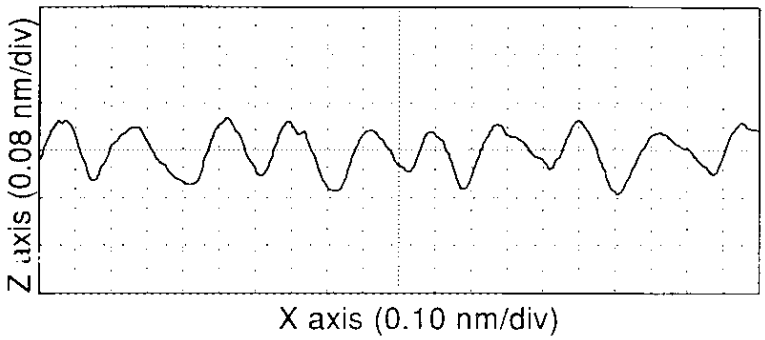

Fig. 3-2 The one dimensional line image of HOPG.

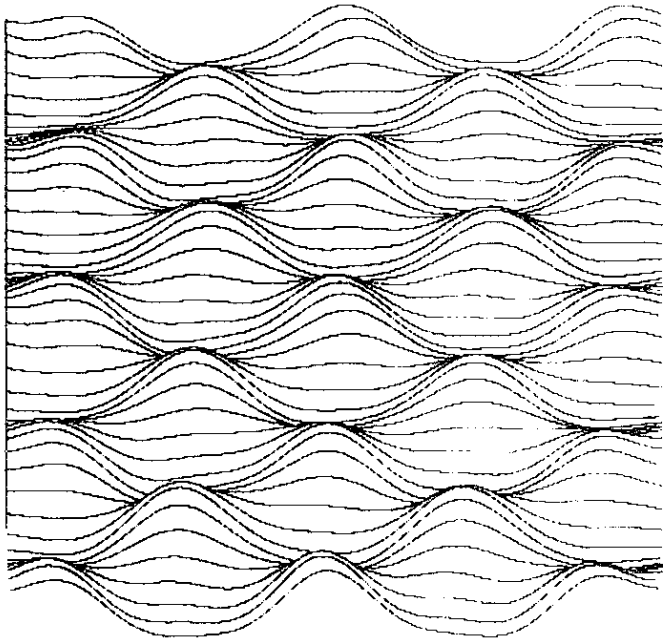

Fig. 3-3 The two dimensional line image of HOPG.

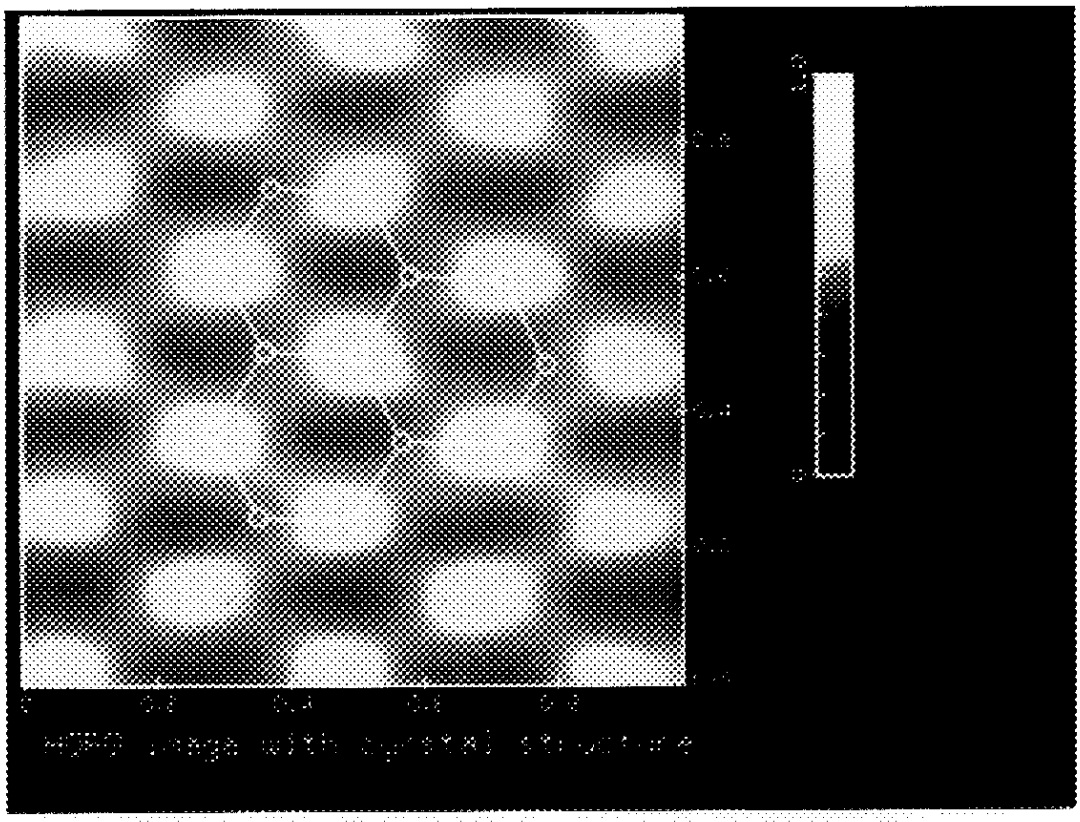

Fig. 3-4 The three dimensional surface image of HOPG with crystal structure. Scan size was 10 Å × 10Å, and bias voltage was -20 mV. The bright parts correspond to carbon atoms.

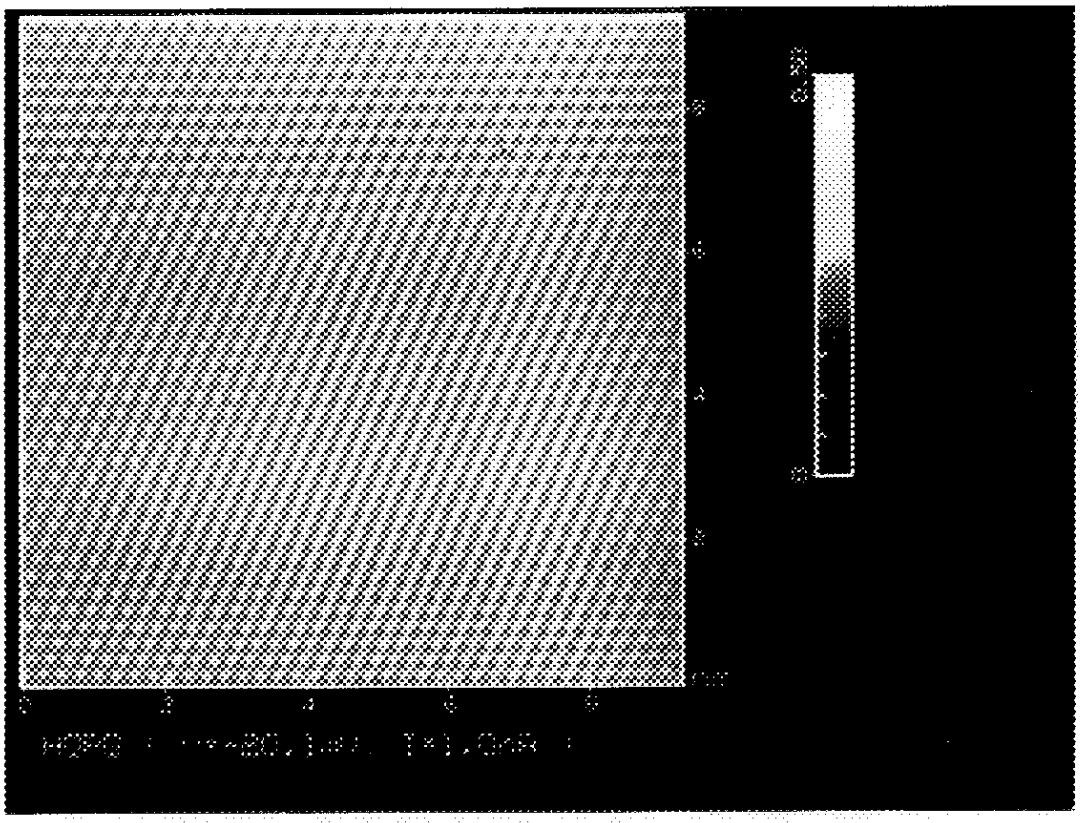

Fig. 3-5 The wide area surface image of HOPG with 100 Å × 100Å. The sample bias and tunneling current were -20 mV and 1 nA.

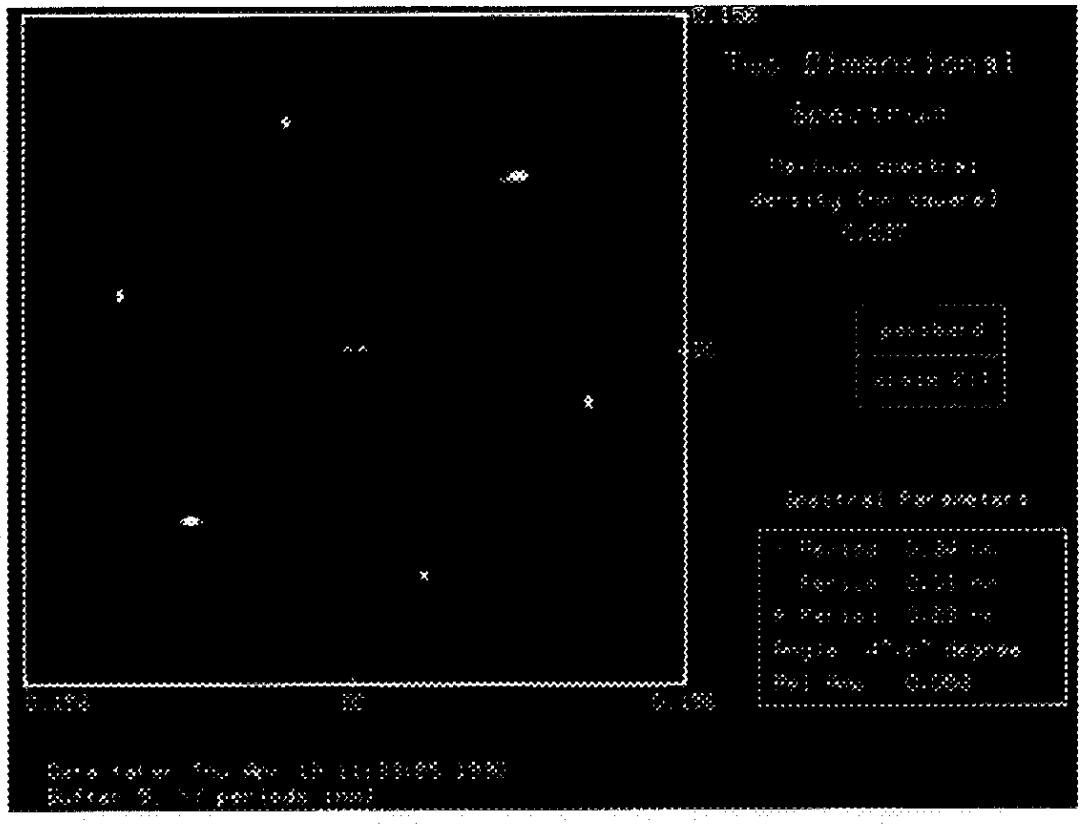

Fig. 3-6 The two dimensional spectrum filtered by FFT for HOPG.

3.3. Bis(ethylenedithio)-tetrathiafulvalene (BEDT-TTF) Salt

Some of the BEDT-TTF salts, $(BEDT\text{-}TTF)_2X$, are known to be layered structure organic conductors or superconductors. In particular, the $(BEDT\text{-}TTF)_2Cu(NCS)_2$ is the most famous for its high transition temperature (Tc = 10.4 K) among the organic superconductors[6],[7]. The two dimensional (2D) crystal structure was reported with X-ray crystal analysis[8], and the 2D character of the electronic structure has also been clarified by the magneto electrical measurements[9]. However, it is still interesting and worthwhile to observe **direct** images of molecules at the **surface** of these crystals by STM because the crystal structure revealed by an X-ray analysis is an **average** structure for the **bulk** of the crystal. STM could directly reveal existing defects or impurities while it is impossible for X-ray diffraction to detect such non-periodic structures. Furthermore, STM images are predominantly reflecting a spatial distribution of HOMO-LUMO or Frontier electron densities while the structure by a conventional X-ray analysis corresponds to a spatial distribution of atomic nuclei or core-electrons positions, so each structure is not always coincident with each other. Two-dimensionality (2D) in the electronic structure of these crystals have been indirectly inferred based on several experimental and theoretical results which can be explained by assuming 2D anisotropy. Applying STS for these crystals, we could **directly** reveal the 2D character in the electronic structure. This is another importance to carry out STM/STS experiments for this type of layered materials, e.g. $(BEDT\text{-}TTF)_2X$ type organic superconductors or copper oxide superconductors.

In our experiment, the three types of salts were used; $(BEDT\text{-}TTF)_2Cu(NCS)_2$, $(BEDT\text{-}TTF)_2MHg(SCN)_4$ (M= Cs, Rb, K and NH_4) and $(BEDT\text{-}TTF)_3Li_{0.5}Hg(SCN)_4(H_2O)_2$. In this series of compounds, the size of anion was systematically changed and the corresponding effect for crystal structure or electronic properties was the subject to be studied. The X-ray analysis for crystal structure was going on for the latter two types crystals by Mori *et al.*[10], and they were claiming the difference of crystal structures among these crystals. So, it was worthwhile to confirm the X-ray analysis results by our STM method as a collaboration. Single crystals were prepared by Mori *et al.* with the electrochemical

oxidation of BEDT-TTF in a 1,1,2-trichloroethane solution under the constant current of 1.5 μA at room temperature using potassium thiocyanate, copper(I) thiocyanate, and 18-crown-6 ether as the supporting electrolytes and platinum rods as the electrodes. These single crystals were black colored and typical size was 0.1 mm × 1 mm × 1 mm in the directions of a* (perpendicular to the *bc* plane), b and c axes, respectively, and their crystal structure parameter which was determined by X-ray diffraction analysis is shown in Table 3-1 with other properties[10].

A single crystal of $(BEDT\text{-}TTF)_2X$ was fixed on a copper plate by gold paste because the sample was too small to hold by metal clip. Then sample bias was applied through the copper plate. The STM current images were obtained at room temperature in air with a NanoScope Ⅱ (Digital Instrument) (see 2.2.). The PtIr tip was used in all these experiments and the crystal surface was observed without any cleaning treatment. Optically shinning surfaces (2D plane) usually gave good STM results. On the other hand, it was very difficult to obtain the image of the side view of a crystal, because their crystals were very thin and rough in this plane. In this case, the flat crystal was fixed to side-face up with gold paste. Therefore the coarse approach should be carried out carefully to make a soft landing to the side face with a high resolution optical microscope. Figure 3-7 shows the distribution of the highest occupied molecular orbital (HOMO). The high concentration of the electron density is clearly on the sulphur atom , therefore the sulphur atoms expected to be seen more easily than other atoms.

In conclusion, arrangement of molecules at the surface of this type of crystal almost coincides with the bulk structure observed by X-ray diffraction within the molecular site resolution. We can tell nothing more of atomic level resolution in this experiment, but a surface effect might be revealed with atomic level resolution, if any. Anyhow, the differences in crystal structure among these samples claimed by X-ray diffraction analysis are confirmed by our STM observation. Details of the results are described in the following section.

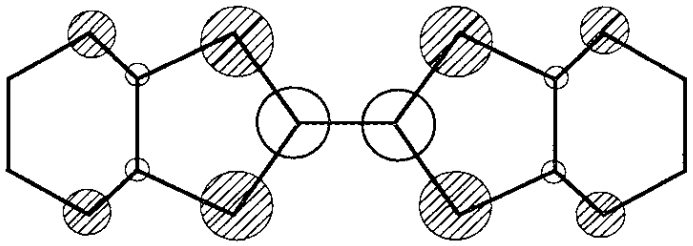

Fig. 3-7 HOMO structure of BEDT-TTF molecule.

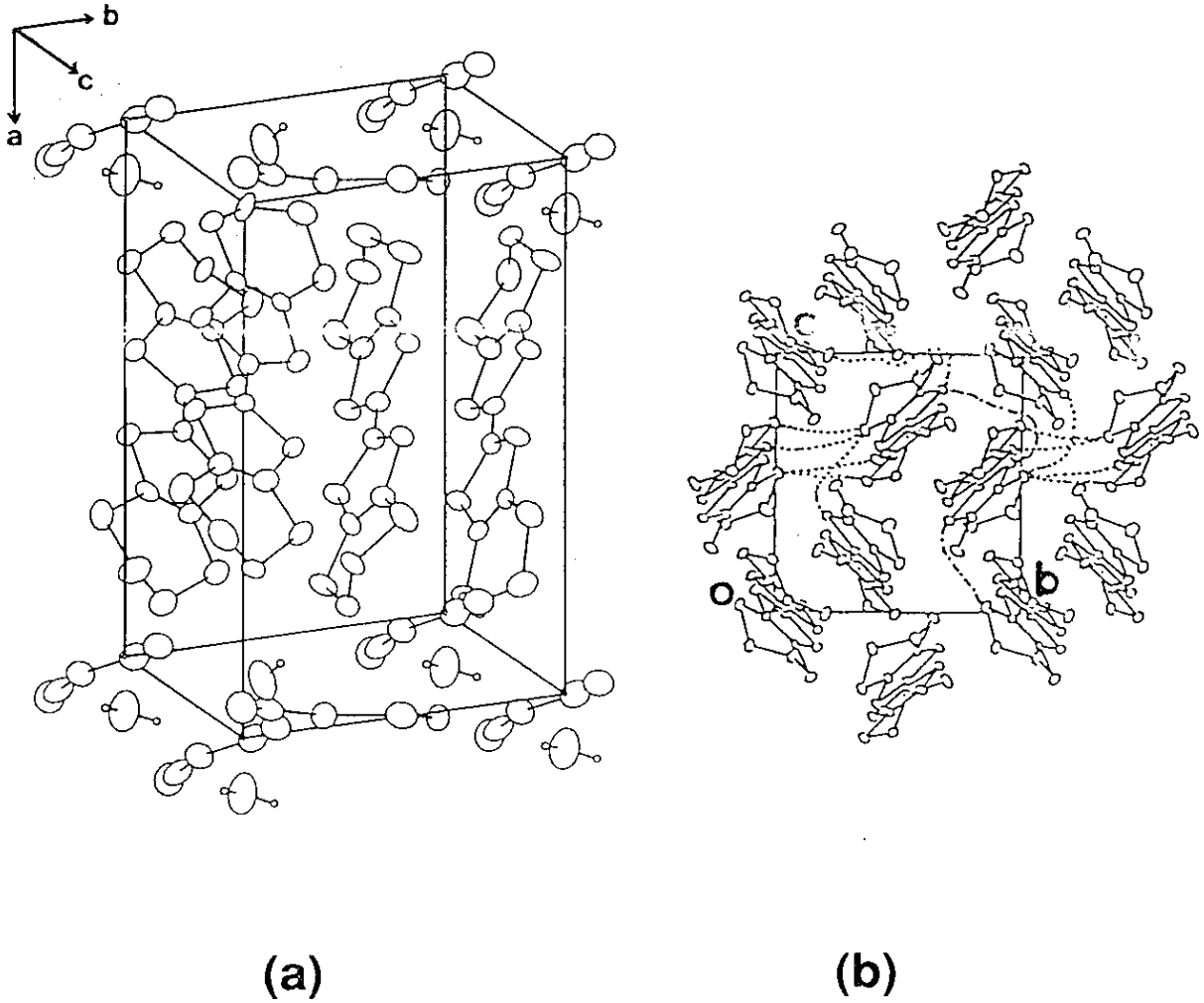

Fig. 3-8 The crystal structures of $(BEDT\text{-}TTF)_2Cu(NCS)_2$. (a) The *bc* plane corresponds to the 2D plane and BEDT-TTF molecules are sandwitched with anion layers. (b) The top view of $(BEDT\text{-}TTF)_2Cu(NCS)_2$. The dotted lines show S··S contacts.

Table 3-1 The color, shape, electrical conductivity, crystallographic data and other properties for mercury thiocyanate salts based upon BEDT-TTF (ET) with Cu, Rb, NH_4, K, Li and Cs.

Samples	$(ET)_2Cu$ $(NCS)_2$	$(ET)_2Rb$ $Hg(SCN)_4$	$(ET)_2NH_4$ $Hg(SCN)_4$	$(ET)_2KHg$ $(SCN)_4$	$(ET)_3Li_{0.5}$ $Hg(SCN)_4$ $(H_2O)_2$	$(ET)_2Cs$ $Hg(SCN)_4$
a (Å)	16.284	10.050	10.091	10.082	12.583	20.903
b	8.440	20.566	20.595	20.565	19.721	22.097
c	13.124	9.965	9.963	9.933	36.395	4.459
α (°)	90.0	103.57	103.65	103.70	89.05	90.01
β	110.30	90.57	90.53	90.91	103.29	96.14
γ	90.0	93.24	93.30	93.06	89.07	77.36
color	black	black	black	black	black	black
shape	plate	plate	plate	plate	block	plate
conductibity (Scm^{-1})	2.5	6	110-380	20-100	9	5
system	monoclinic	triclinic	triclinic	triclinic	triclinic	triclinic

3.3.1. $(BEDT\text{-}TTF)_2Cu(NCS)_2$

The crystal structure of $(BEDT\text{-}TTF)_2Cu(NCS)_2$,is shown in Fig. 3-8, which was determined by X-ray diffraction[8]. The system is monoclinic and lattice parameters are a= 16.248 Å, b= 8.440 Å, c= 13.124 Å and β= 110.30 °. The layered structure where BEDT-TTF conductive sheet stacks on a $Cu(NCS)_2$ anion layer alternately, can be seen in Fig. 3-8(a), and its period along the a-axis is 16.248 Å. The top view of the crystal structure is shown in Fig. 3-8(b) , in which the κ type arrangement of (BEDT-TTF) molecule can be recognized. Moreover, there are short S··S contacts between intra- and interpair to construct the two dimensional layer.

A typical example of the STM observation for a $(BEDT\text{-}TTF)_2Cu(NCS)_2$ crystal is shown in Fig. 3-9. In this figure, (a) is the 30 Å × 30 Å image for the *bc* plane that corresponds to the 2D metallic plane. The applied bias voltage was -23.5 mV. Since the similar image was obtained for the inverse bias voltage (23.5 mV), the electronic structure should be metallic, and this image corresponds to the 2D BEDT-TTF molecular arrangement, which is in good agreement with the reported crystal structure determined by X-ray diffraction. Intermolecular couplings of the electron clouds through S··S bonding can be recognized in this figure.

On the other hand, the side-view image of this crystal is shown in Fig. 3-9(b) as the 120 Å × 120 Å image for the plane along a-axis. The image was obtained when bias voltage was 50 mV and tunneling current was 1 nA. This image clearly shows the alternating stacks of BEDT-TTF conductive layers and $Cu(NCS)_2$ anion nonconductive layers, and the spacing period is about 15 Å that is in good agreement with the lattice constant of a-axis (16.24 Å).

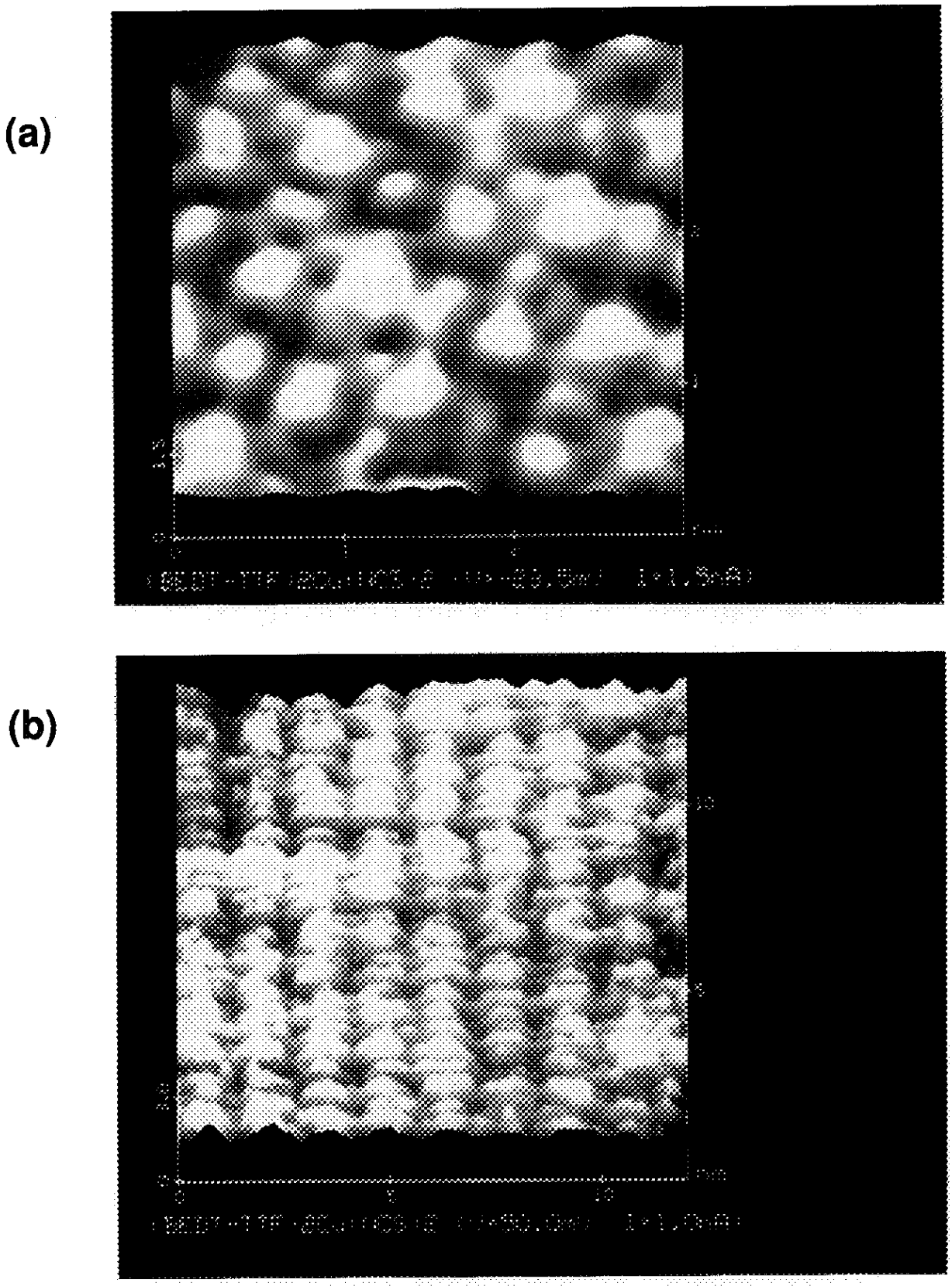

Fig. 3-9 STM images of $(BEDT\text{-}TTF)_2Cu(NCS)_2$ single crystal; (a) for the *bc* plane with a sample bias of -23.5 mV and a scanning area of 30 Å × 30 Å, and (b) for the plane along a-axis with a sample bias of -50 mV and scanning area of 120 Å × 120 Å.

3.3.2. $(BEDT\text{-}TTF)_2KHg(SCN)_4$

The crystal structure of $(BEDT\text{-}TTF)_2KHg(SCN)_4$ was determined by X-ray diffraction[11], as shown in Fig.3-10. This crystal belongs to triclinic system, and the crystallographic data are a= 10.082 Å, b= 20.565 Å, c= 9.933 Å, α= 103.70 °, β= 90.91 ° and γ= 93.06 °, respectively (as shown in Table 3-1). In this salt, 2D plane is *ac* plane.

Typical STM image for the *ac* plane of this crystal is shown in Fig. 3-11(a). which was obtained by the constant current mode (sample bias: -22.3 mV, tunneling current: 3 nA and scan area: 60 Å × 60 Å). The arrangement of α-type can be recognized. When the inverse bias was applied (22.3 mV), the image did not almost change, therefore it was considered that the image corresponded to the 2D BEDT-TTF molecular arrangement and the image is in good agreement with the crystal structure determined by X-ray diffraction. In this image, there seems to be two types' molecules; the bright line of molecule and a little dark line of molecule ordered alternately. This is explained as the influence of anion layer[12]. Figure 3-12 shows the top view of the BEDT-TTF cation layer where the position of K and Hg ions in the top layer are also marked. There are four type positions of molecules which are labeled A to D. On the line of A-B, the anion ions sit on the center between A and B, but on the line of C-D, the anion ions sit just above BEDT-TTF molecules. Therefore, the molecules at A and B look brighter than the molecules at C and D.

On the other hand, the current image for side view is shown in Fig. 3-11(b) with 110 Å × 110 Å area, -41.8 mV sample bias and 8.2 nA tunneling current. This image clearly shows the alternate stacks of BEDT-TTF conductive layers and $KHg(SCN)_4$ anion layers, and the spacing period is about 20 Å that is in good agreement with the lattice constant of b-axis (20.565 Å) obtained from X-ray analysis.

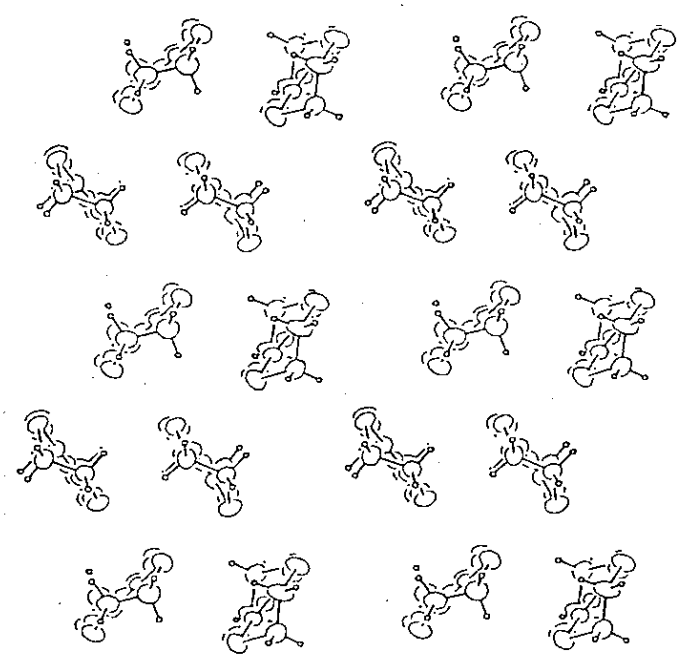

Fig. 3-10 The crystal structure of $(BEDT\text{-}TTF)_2KHg(NCS)_4$.

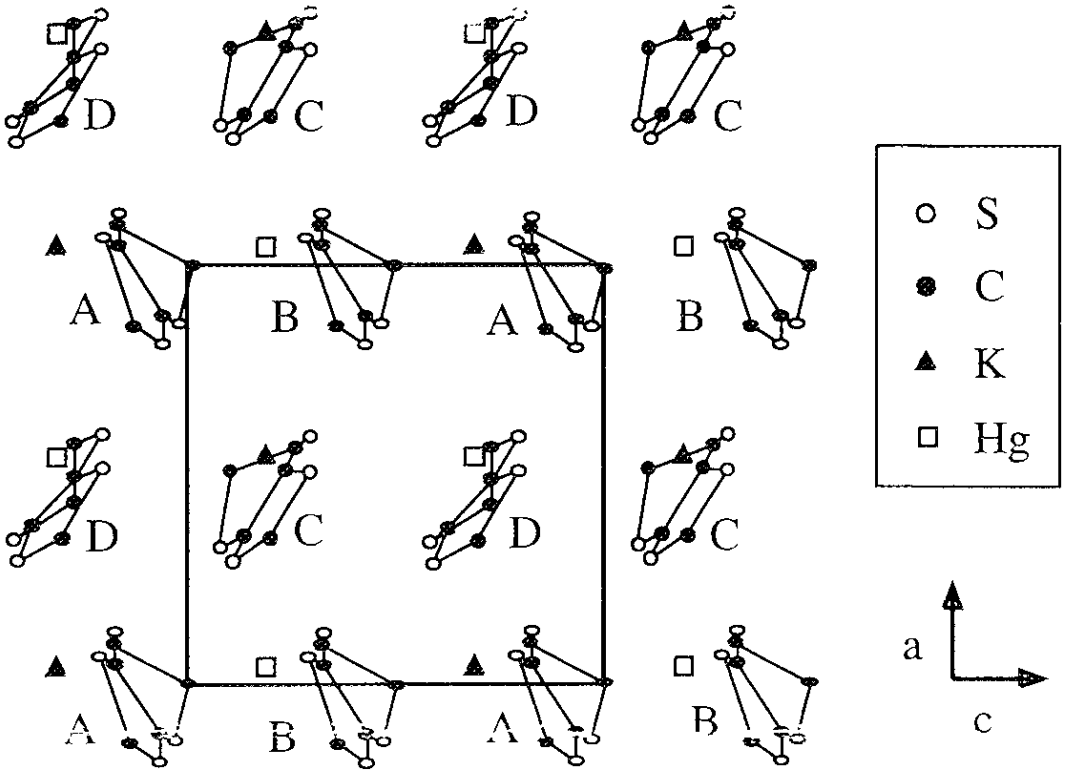

Fig. 3-12 The top view of $(BEDT\text{-}TTF)_2KHg(NCS)_4$ with K and Hg ions in the top anion layer.

(a)

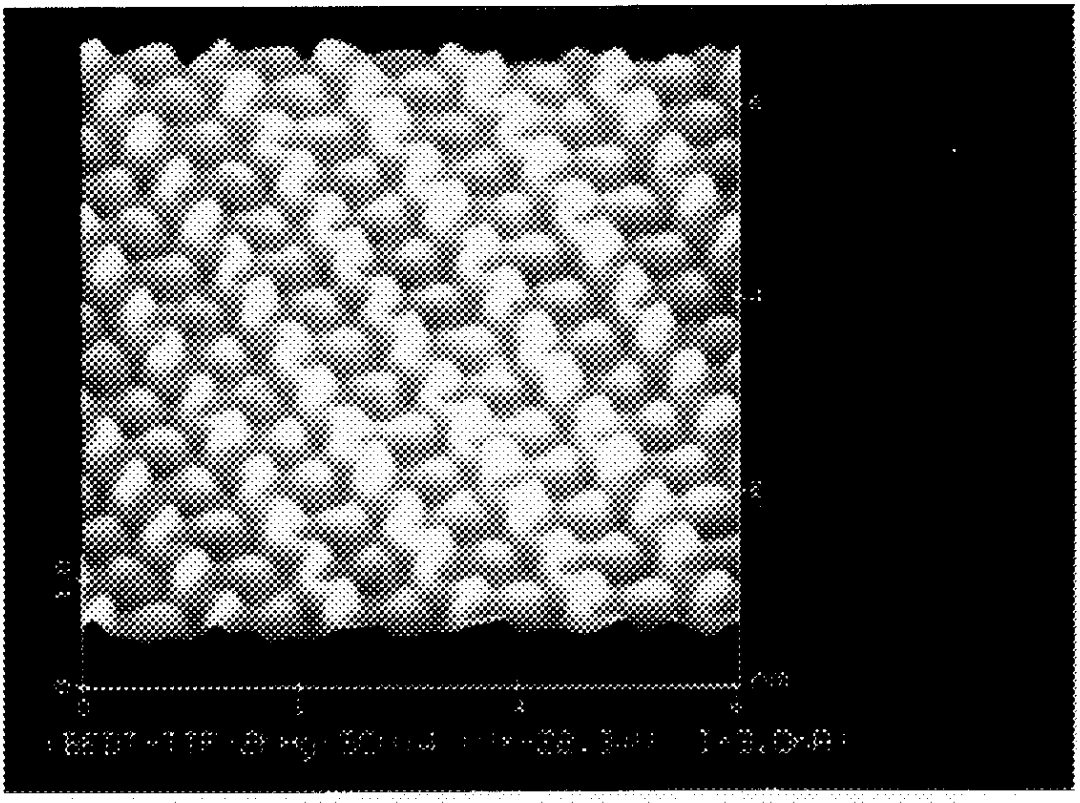

(b)

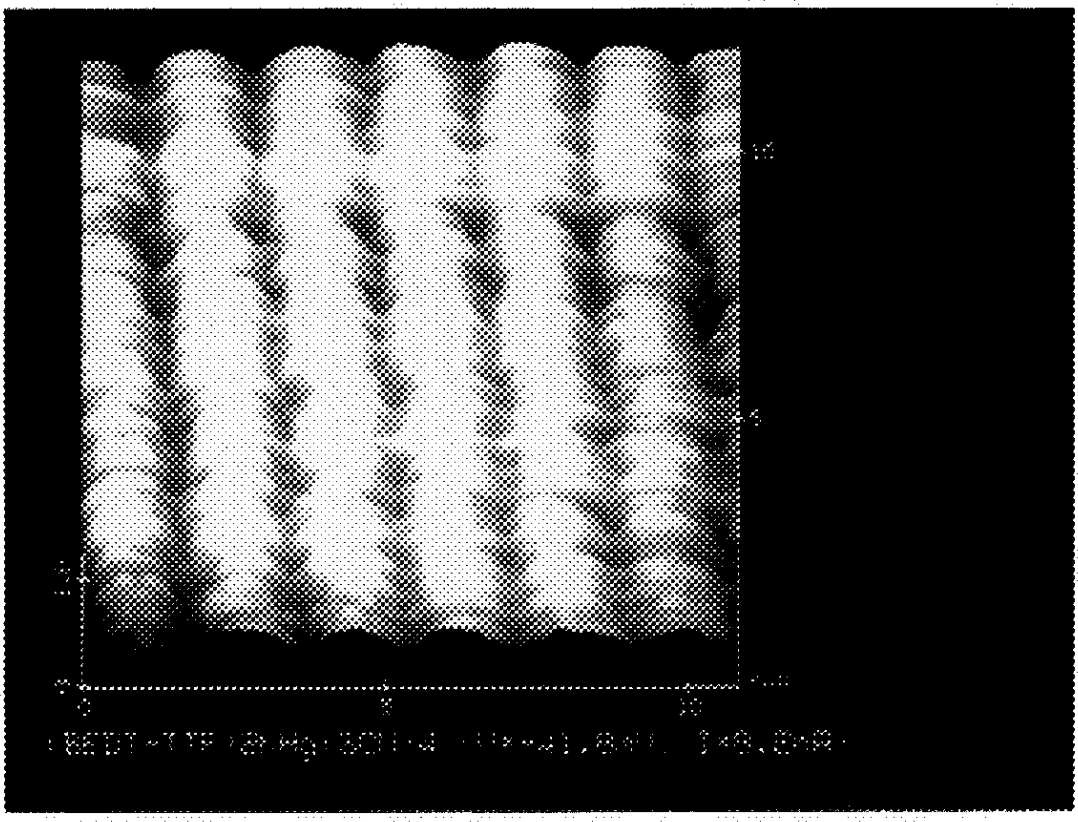

Fig. 3-11 STM images of $(BEDT\text{-}TTF)_2KHg(NCS)_4$ single crystal; (a) for the *ac* plane with a sample bias of -22.3 mV and a scanning area of 60 Å × 60 Å, and (b) for the plane along a-axis with a sample bias of -41.8 mV and scanning area of 110 Å × 110 Å.

3.3.3. $(BEDT\text{-}TTF)_2RbHg(SCN)_4$

The crystal structure of $(BEDT\text{-}TTF)_2RbHg(SCN)_4$ was determined by X-ray diffraction, as shown in Fig.3-13[10]. The crystal belongs to triclinic system, and the crystallographic data which are almost similar to the $(BEDT\text{-}TTF)_2KHg(SCN)_4$ salt, are a= 10.050 Å, b= 20.566 Å, c= 9.965 Å, α= 103.57 °, β= 90.57 ° and γ= 93.24 °, respectively, and *ac* plane corresponds to the 2D plane.

The STM image for *ac* plane is shown in Fig. 3-14(a) which was obtained by the constant current mode (sample bias: -23.5 mV, tunneling current: 4.6 nA and scan area: 40 Å × 40 Å). When the inverse sample bias was applied (23.5 mV), the image was not influenced also. Therefore the STM image is corresponding to the 2D BEDT-TTF molecular arrangement, and the image is in good agreement with the crystal structure determined by X-ray diffraction. In the case of this image, also two types' molecules (bright image molecules and little dark image molecules) can be seen, by the same reason described above (see 3.3.2.).

On the other hand, the current image for side view is shown in Fig.3-14(b) with 210 Å ×210 Å area, -20.1 mV sample bias and 6.1 nA tunneling current. This image clearly shows the alternate stacks of BEDT-TTF conductive layers and $RbHg(SCN)_4$ anion layers, and the spacing period is about 20 Å that is in good agreement with the lattice constant of b-axis (20.566 Å).

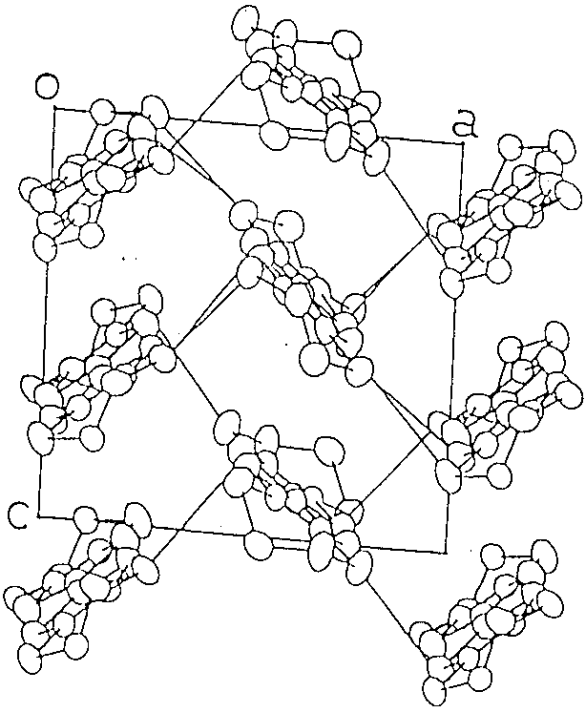

Fig. 3-13 The crystal structure of $(BEDT\text{-}TTF)_2RbHg(NCS)_4$.

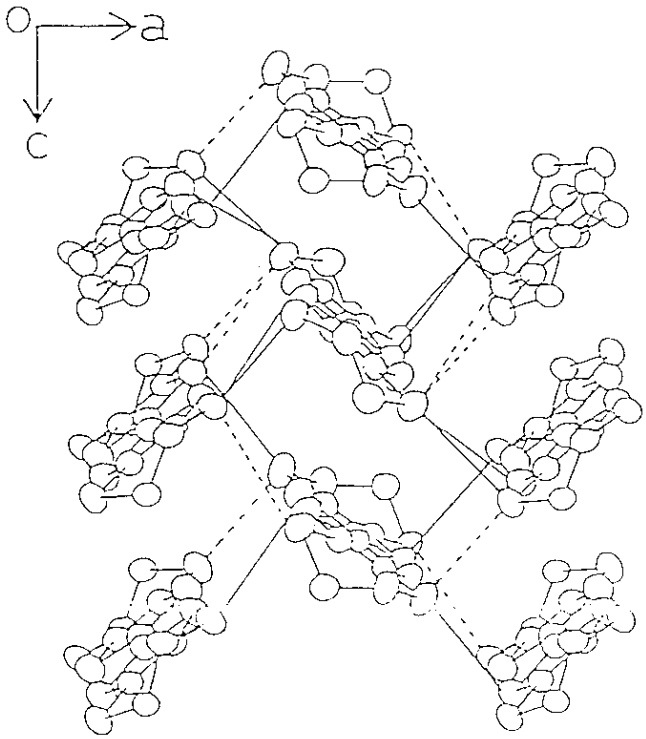

Fig. 3-15 The crystal structure of $(BEDT\text{-}TTF)_2NH_4Hg(NCS)_4$.

(a)

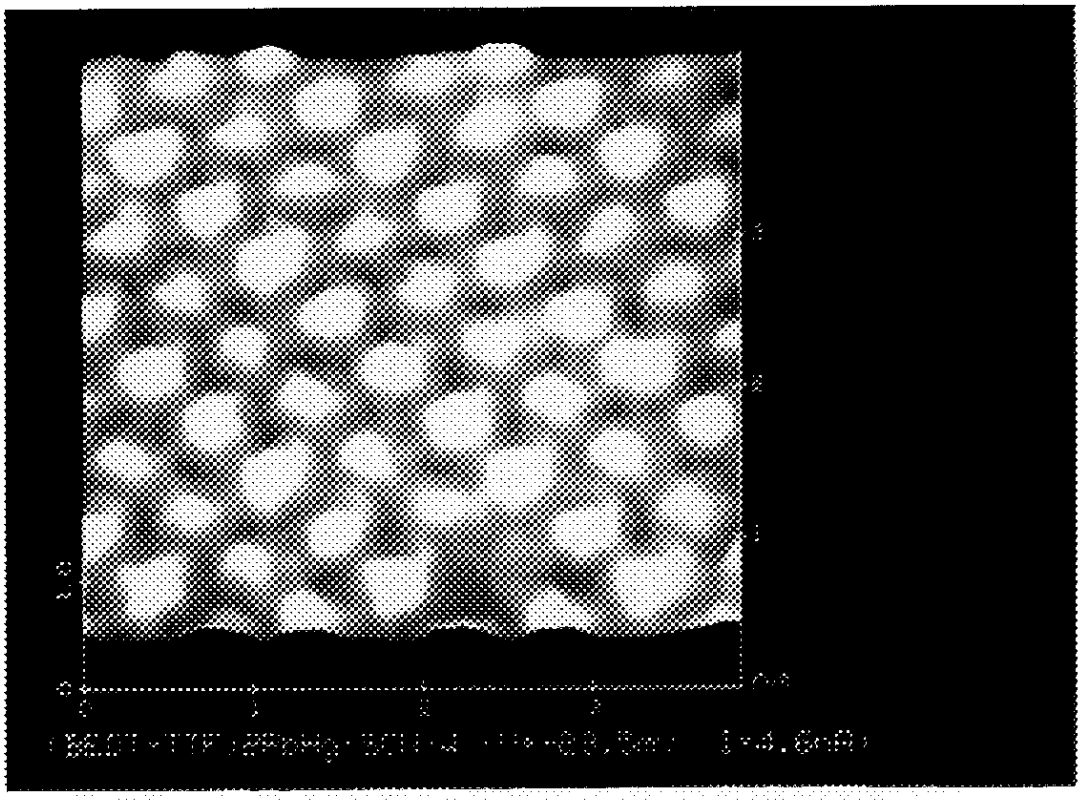

(b)

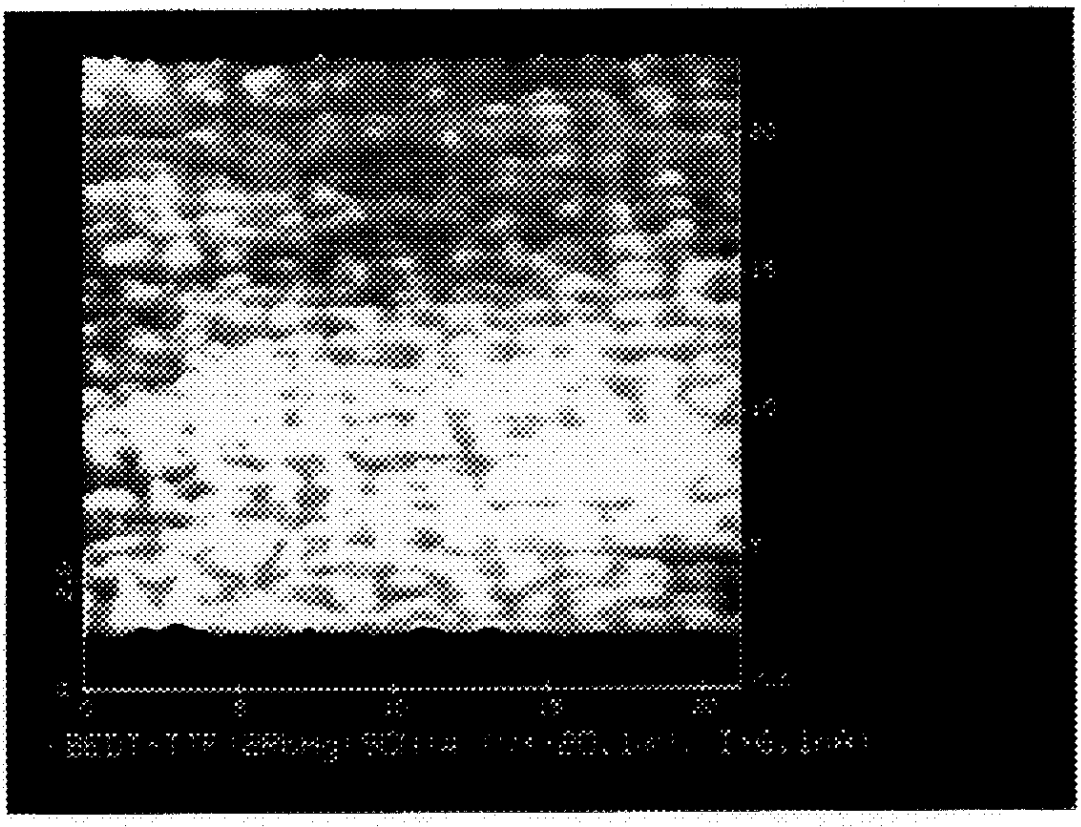

Fig. 3-14 STM images of $(BEDT\text{-}TTF)_2RbHg(NCS)_4$ single crystal; (a) for the *ac* plane with a sample bias of -23.5 mV and a scanning area of 40 Å × 40 Å, and (b) for the plane along a-axis with a sample bias of -20.1 mV and scanning area of 210 Å × 210 Å.

3.3.4. $(BEDT\text{-}TTF)_2NH_4Hg(SCN)_4$

The $(BEDT\text{-}TTF)_2NH_4Hg(SCN)_4$ becomes superconductor at 0.8 K. The crystal structure, which was determined by X-ray diffraction, is shown in Fig. 3-15[10], and its system is triclinic. The crystallographic data of the salt are almost same the above two salts, and lattice parameters are a= 10.091 Å, b= 20.595 Å, c= 9.963 Å, α= 103.65 °, β= 90.53 ° and γ= 93.30 °, respectively. In this salt, 2D plane is *ac* plane, also.

The STM image for *ac* plane is shown in Fig. 3-16(a) which was almost same above two salts. The image was obtained by the constant current mode, and the parameters were as follows; sample bias was -29.9 mV, the tunneling current was 1.0 nA and scan area was 100 Å × 100 Å . The arrangement of α-type can be recognized as similar as the above case. When the inverse sample bias was applied (29.9 mV), the image was almost unchanged, The arrangement of molecules is in good agreement with the crystal structure determined by X-ray diffraction. In this image, we can see two types' molecules as similar as the above described (see 3.3.2.)[13].

On the other hand, the current image for side view is shown in Fig.3-16(b) with 410 Å ×410 Å area, -51.9 mV sample bias and 1.0 nA tunneling current. This image clearly shows the alternate stacks of BEDT-TTF conductive layers and $NH_4Hg(SCN)_4$ anion layers, and the spacing period is about 20 Å that is in good agreement with the lattice constant of b-axis (20.595 Å).

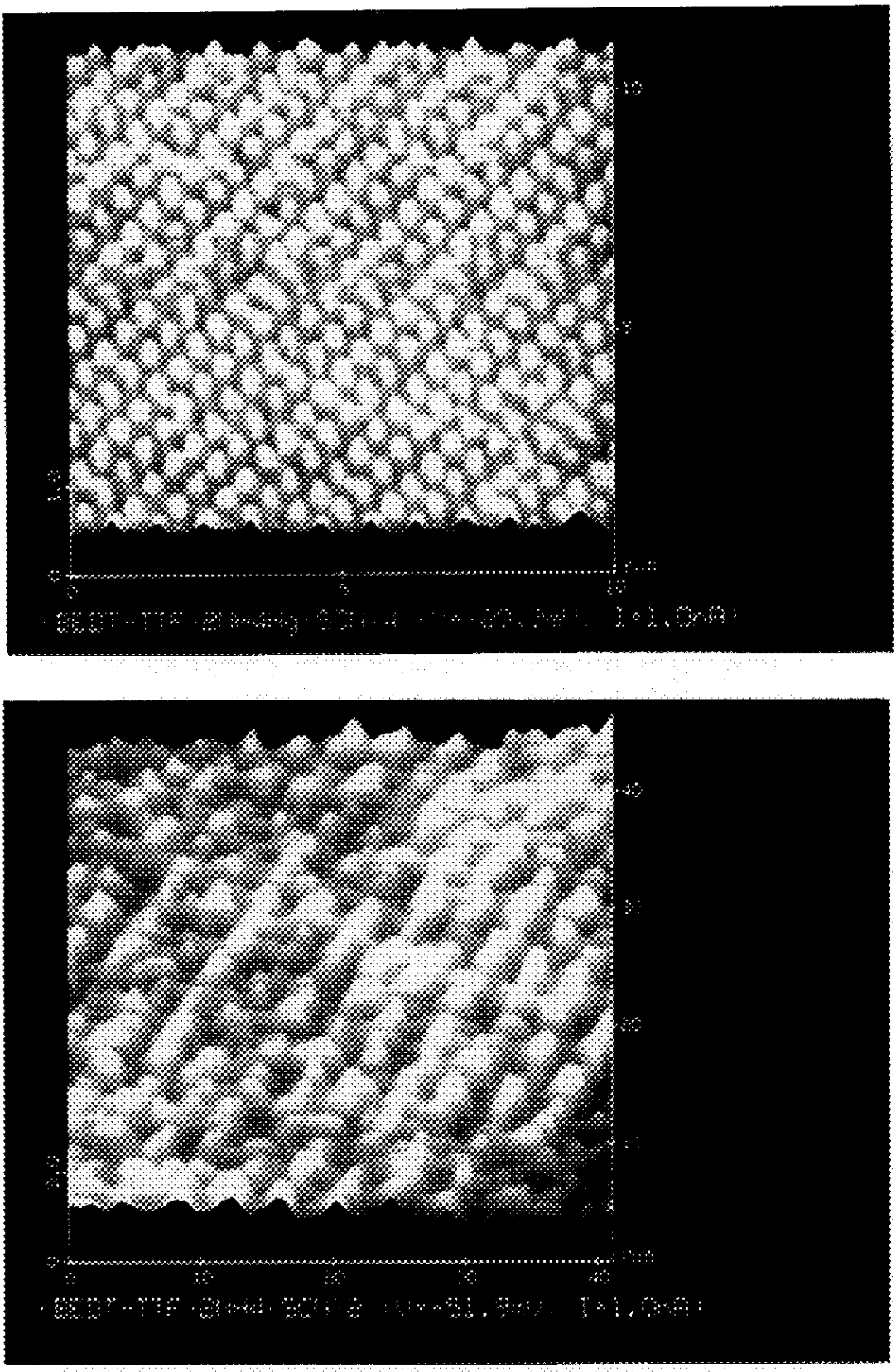

Fig. 3-16 STM images of $(BEDT\text{-}TTF)_2NH_4Hg(NCS)_4$ single crystal; (a) for the *ac* plane with a sample bias of -29.9 mV and a scanning area of 100 Å × 100 Å, and (b) for the plane along a-axis with a sample bias of -51.9 mV and scanning area of 410 Å × 410 Å.

3.3.5. $(BEDT\text{-}TTF)_2CsHg(SCN)_4$

The crystal structure of $(BEDT\text{-}TTF)_2CsHg(SCN)_4$, which was determined by X-ray diffraction, is shown in Fig. 3-17[14]. Though the salt belongs to triclinic system, there is a little difference compare with above three salts. The crystallographic data are a= 20.903 Å, b= 4.459 Å c= 22.097 Å, α= 90.01 °, β= 96.14 ° and γ= 77.36 °, respectively , and the 2D plane is *bc* plane. The arrangement of molecule belongs to α''-type, and there are four molecules in a unit cell along c-axis as shown in Fig. 3-17.

The STM image for *bc* plane is shown in Fig. 3-18(a) which was obtained by the constant current mode (sample bias: -41.8 mV, tunneling current: 6.8 nA, and scan area: 50 Å × 50 Å). The arrangement of four molecules in a unit cell is clearly recognized. In this case, if the inverse sample bias (41.8 mV) was applied, the image was almost unchanged, also. The 2D unit cell size is 22 Å × 4.5 Å and is in good agreement with the crystal structure determined by X-ray diffraction.

On the other hand, the current image for side view is shown in Fig. 3-18(b) which was taken at 200 Å ×200 Å area, -22.0 mV sample bias, and 2.2 nA tunneling current. This image clearly shows the alternate stacks of BEDT-TTF conductive layers and $CsHg(SCN)_4$ anion layers, and the spacing period is about 20 Å that is in good agreement with the lattice constant of a-axis (20.903 Å).

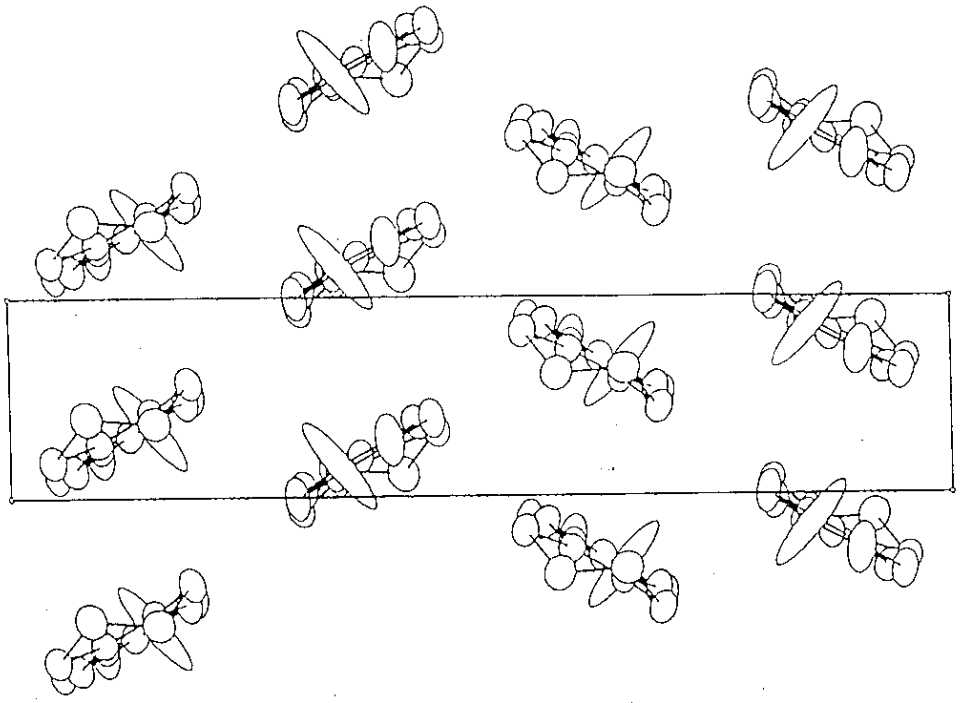

Fig. 3-17 The crystal structure of $(BEDT\text{-}TTF)_2CsHg(NCS)_4$.

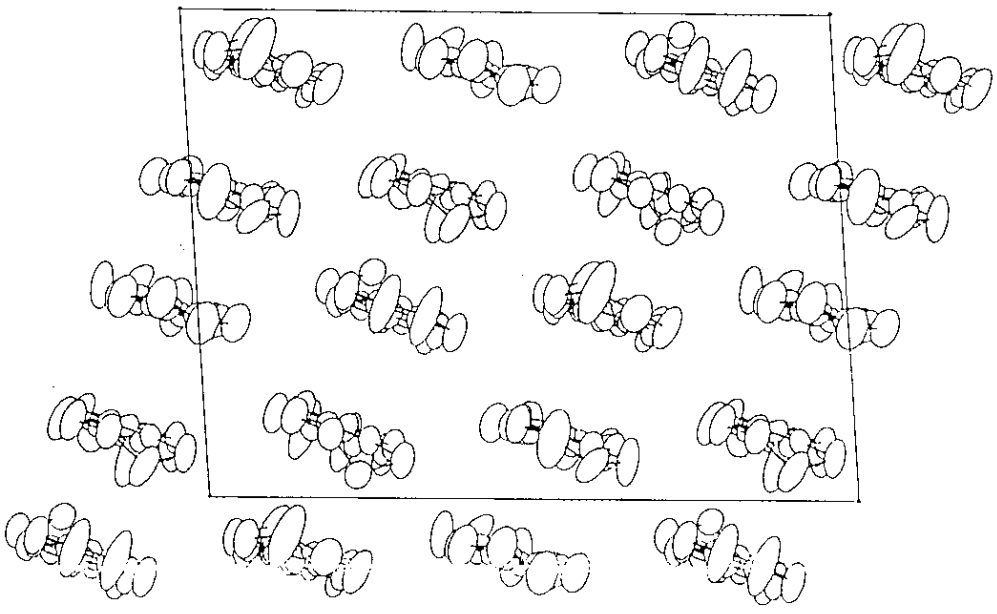

Fig. 3-19 The crystal structure of$(BEDT\text{-}TTF)_3Li_{0.5}Hg(SCN)_4(H_2O)_2$.

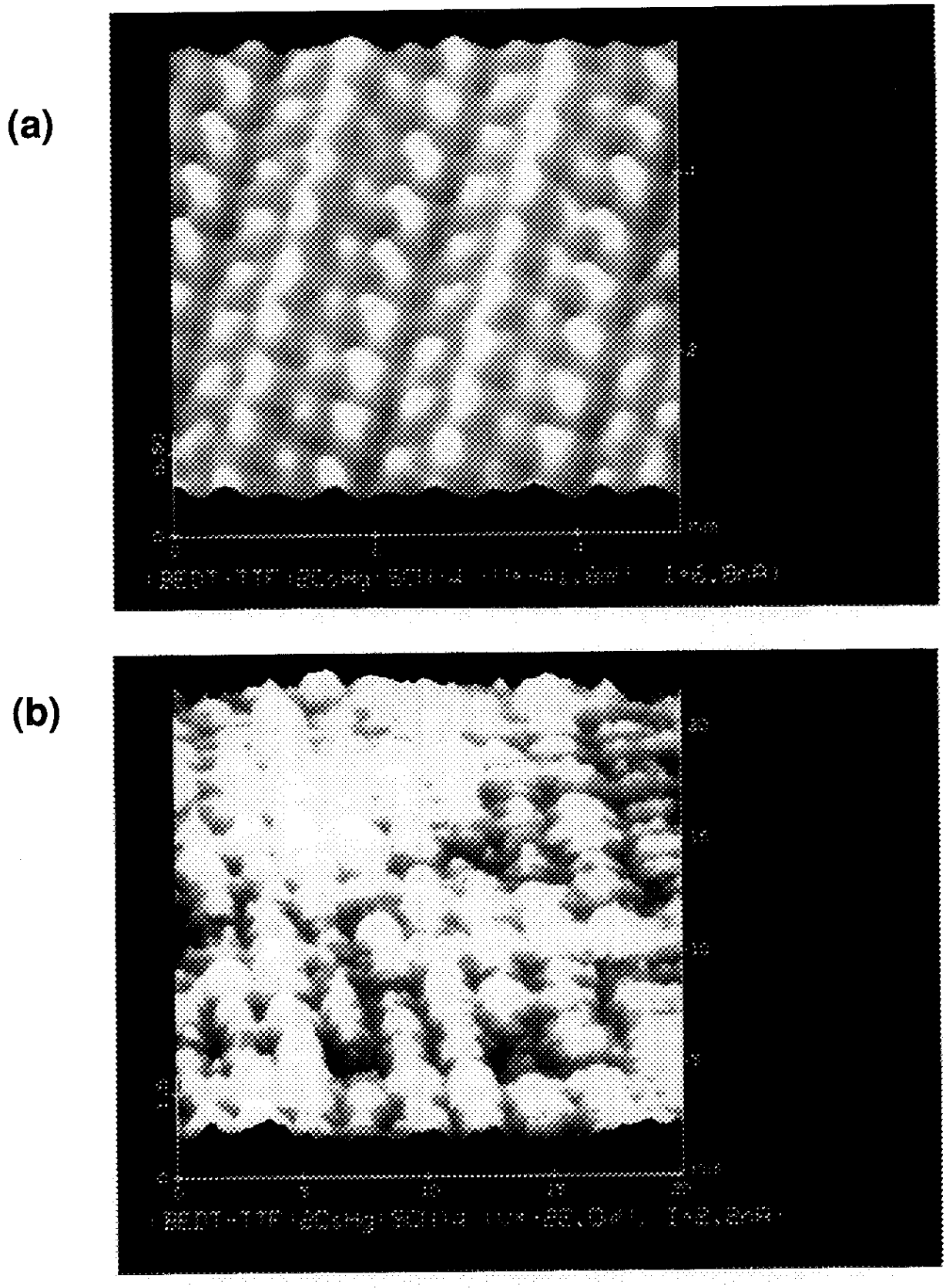

Fig. 3-18 STM images of $(BEDT\text{-}TTF)_2CsHg(NCS)_4$ single crystal; (a) for the *bc* plane with a sample bias of -41.8 mV and a scanning area of 50 Å × 50 Å, and (b) for the plane along a-axis with a sample bias of -22.0 mV and scanning area of 200 Å × 200 Å.

3.3.6. $(BEDT\text{-}TTF)_3Li_{0.5}Hg(SCN)_4(H_2O)_2$

The crystal structure of $(BEDT\text{-}TTF)_2Li_{0.5}Hg(SCN)_4(H_2O)_2$ which was determined by X-ray diffraction is shown in Fig. 3-19[14]. The salt belongs to monoclinic system, and the crystallographic data are a= 12.583 Å, b= 19.721 Å, c= 36.395 Å and β= 91.50 °, respectively. In this salt, 2D plane is *ab* plane.

Typical STM image for *ab* plane is shown in Fig. 3-20 which was obtained by the constant current mode (sample bias: -35.7 mV, tunneling current: 5.6 nA and scan area: 60 Å × 60 Å). When the inverse sample bias was applied (35.7 mV), the image was almost unchanged, also. The image is in good agreement with the crystal structure determined by X-ray diffraction.

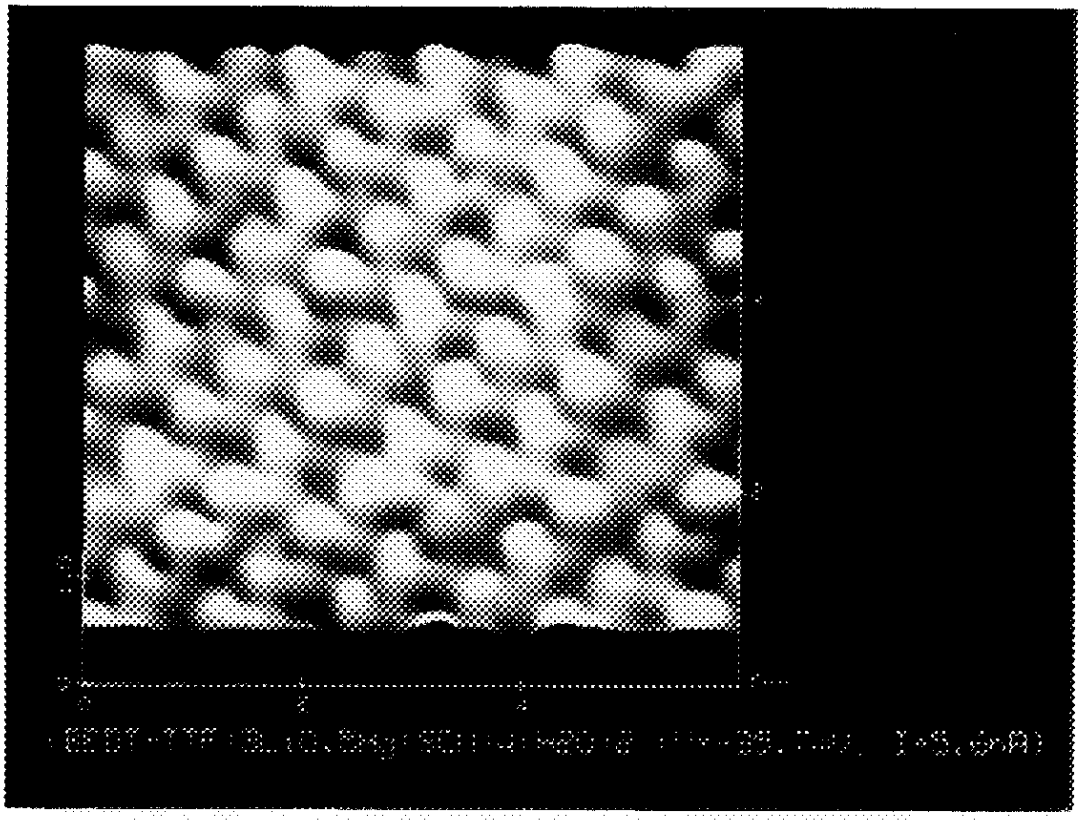

Fig. 3-20 STM image of $(BEDT\text{-}TTF)_3Li_{0.5}Hg(SCN)_4(H_2O)_2$ single crystal for the *ab* plane with a sample bias of -35.7 mV and a scanning area of 60 Å × 60 Å.

3.3.7. Conclusion

In this section (3.3), we presented STM images for the series of $(BEDT\text{-}TTF)_2X$ in which the size of anions was systematically changed. For $X=Cu(NCS)_2$ salt anion size is smallest and the lattice constants are also small. Consequently, 2D intermolecular interaction (κ-type) fairly large and it shows highly metallic character. On the other hand, for $X=MHg(SCN)_4$ (M=Cs, Rb, K and NH_4) salts the lattice constants become lager depending on the size of anions. In the case of M=Rb, K and NH_4, it was known by X-ray analysis that the crystals are all isomorphous and molecular arrangement in 2D plane is α-type. These features are clearly visualized in STM images. Because of the increase of the anion layer thickness, 2D character in donor layer becomes stronger and the layer alternation contrast becomes more evident (see Fig. 3-11(b)). All three salts are metallic even at very low temperatures (2D character). M=Cs salt has a different crystal structure. Very large cation size (Cs^+) may make the 2D interaction weaker and rather 1D column structure is visualized in STM image (Fig. 3-18). Consequently this salt shows metal-insulator (M-I) transition at 210K. Although in M=Li salt cation size is small, the inclusion of water molecule ($Li_{0.5}Hg(SCN)_4(H_2O)_2$) may deform the crystal structure and also 1D like structure is predominant. This salt also shows M-I transition at 170K.

In conclusion, all features in the crystal structure obtained by X- ray analysis are almost faithfully visualized in STM images for $(BEDT\text{-}TTF)_2X$ salts and some of the features are even more evidently recognized in STM images. Thus, we can use STM technique for crystal structure analysis very effectively.

3.4. C_{60} Films on HOPG

The discovery of the method of preparing macroscopic quantities of the pure carbon molecule C_{60}[15] has stimulated numerous studies to determine the bulk and surface structures of the condensed phases of this molecular material. The availability of a solid form has made studies possible using infrared and ultraviolet absorption spectroscopy, X-ray and electron diffraction[16], NMR[17],[18] and Raman spectroscopy[19],[20],[21], all of which provide evidence that supports the proposed "soccer ball " structure of C_{60}. Recently, real-images of C_{60} films have been obtained using high-resolution microscopy techniques such as STM[22],[23],[24],[25],[26],[27],[28],[29], AFM[30],[31],[32] and TEM[33] on thin films of high-purity C_{60} and of C_{60}/C_{70} mixtures prepared on metallic, semiconductor and insulating substrates. In this section, we describe on the soccer ball (C_{60}) image on HOPG substrate which was obtained directly by using STM in air.

Ultra thin films of C_{60} was prepared by the Molecular Beam Epitaxy (MBE) technique. The base pressure in the MBE vessel was about 1×10^{-9} Torr. Powder C_{60} was evaporated slowly (1Å/min) on HOPG substrate, and the total thickness was ~10 Å which corresponds to monolayer of C_{60}.

The grain size of C_{60} film was estimated to be several hundred Å by SEM image as shown in Fig.3-21. Figure 3-22 shows an STM image of the film with 300 Å × 300 Å area at tunnel current of 0.49 nA and sample bias of -799.9 mV. In this figure, two islands were recognized as ~300 Å size which is in agreement with result of SEM image. Moreover, various clusterings of C_{60} molecules were seen around the boundary of island. Figure 3-23 shows a higher magnification view of the film with 100 Å × 100 Å area. In this figure, one-dimensionally ordered clusters was seen more clearly, and distance between two molecules was ~10Å which is close to the intermolecular distance of C_{60} in the crystal.

Why does the one dimensional arrangement occur? There are two interpretations which are the possibility of epitaxial growth and/or the influence of boundary dislocation

line on the substrate. The other image for this film is shown in Fig. 3-24. The figure shows not only C_{60} arrangement but also substrate graphite carbon atom arrangement in which the angle between C_{60} line and graphite carbon line is ~23°. The schematic image to consider the possibility of epitaxial growth is shown in Fig. 3-25. A vector which has 10.72 Å in length and 23.4° degree to graphite carbon line, is drawn from the center of graphite hexagon. The position of arrowhead is equivalent to the start point. This result means that there is a possibility of epitaxial growth of C_{60} on HOPG. In order to occur the epitaxial growth, there should be some interactions between C_{60} and graphite. Chen *et al.*[24] reported that such packing arrangement as short linear chains was obtained in the STM images for C_{60} film on a gold substrate and described the weakness of the bonding force among the

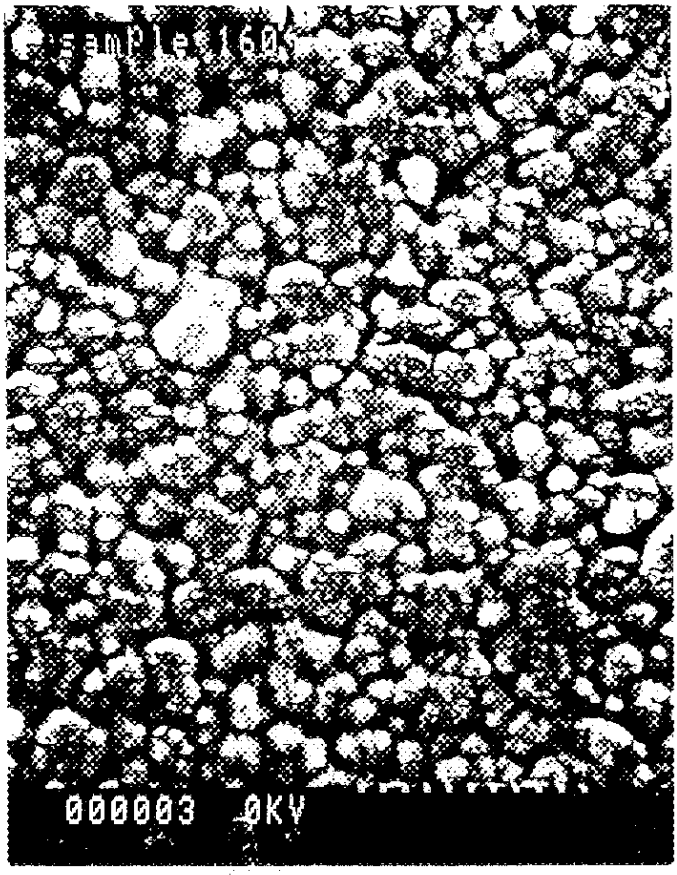

Fig. 3-21 SEM image of C_{60} film on HOPG. The grain size was estimated to be several hundred Å.

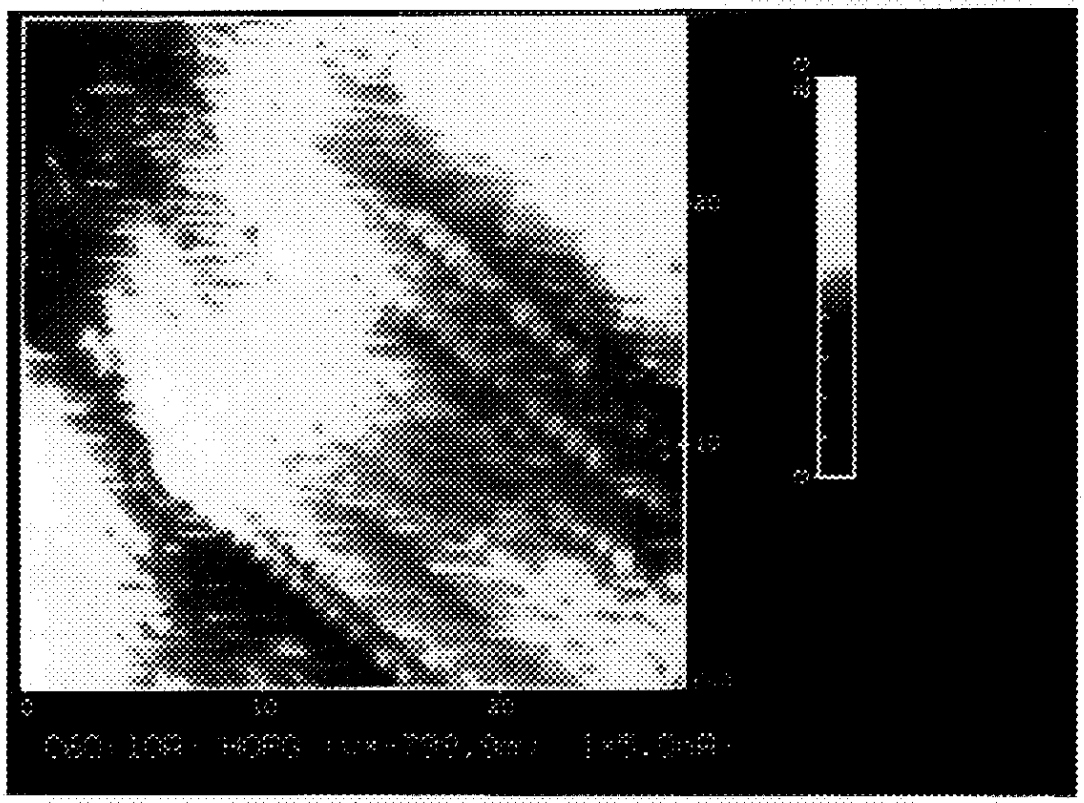

Fig. 3-22 STM image of C_{60} film whose thickness was10 Å, on HOPG with a sample bias of -799.9 mV and a scanning area of 300 Å × 300 Å.

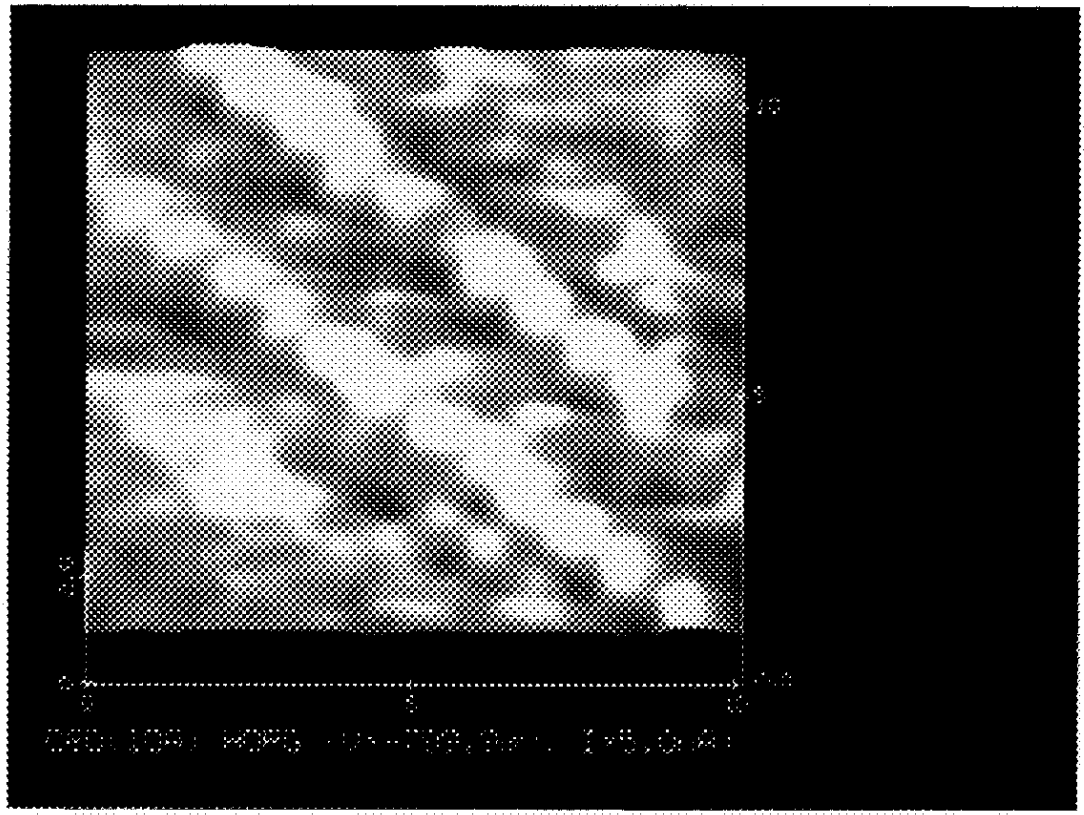

Fig. 3-23 STM image of C_{60} with more high magnification (100 Å × 100 Å). A C_{60} cluster was recognized more clearly.

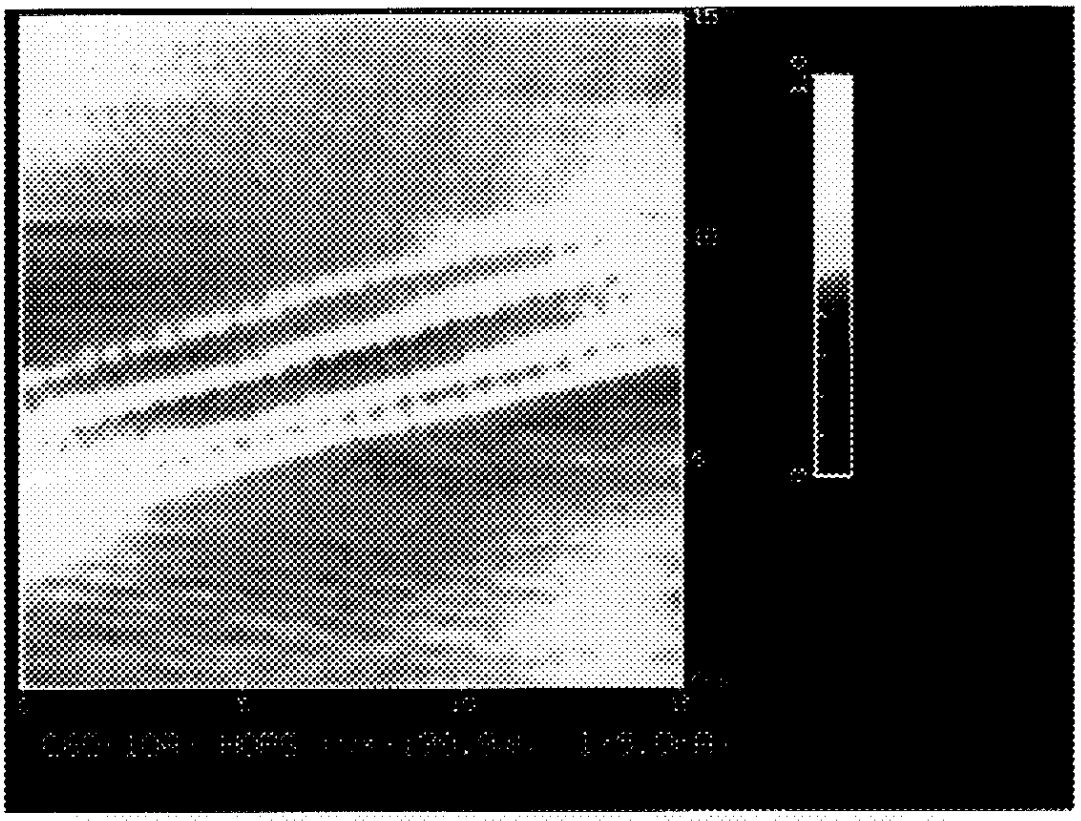

Fig. 3-24 STM image of C_{60} film on HOPG with a sample bias of -199.9 mV. In this figure, not only C_{60} arrangement but also carbon atoms of substrate were recognized. The angle between C_{60} line and graphite carbon line was ~23° ,and the distance between two molecules was ~10 Å.

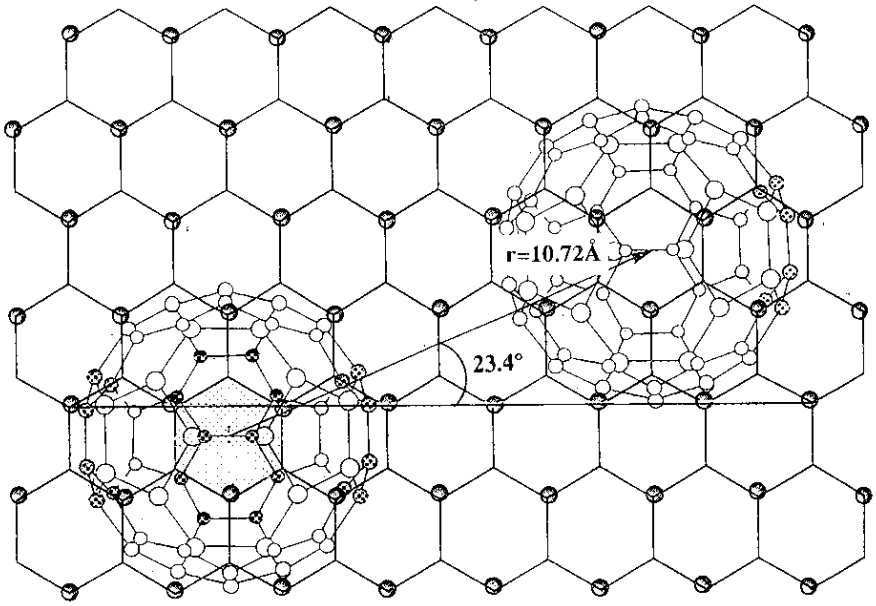

Fig. 3-25 The possibility of epitaxial growth of C_{60} on HOPG.

molecules in the monolayer films. In addition, Liu *et al.*[28] obtained STM images of C_{70} film on HOPG. In this report, they described that the molecular arrangement could be explained for a monolayer of C_{70} on graphite surface by using a C_{70}-graphite and C_{70}-C_{70} two-body potential which include both van der Waals' and dipolar electrostatic but not inductive terms. The result was suggested that C_{70}-graphite interactions involve charge transfer. Mikami *et al.*[34] carried out the simulation of the growth for C_{60} film on HOPG and obtained the growing direction of the C_{60} film which is tilting about 17° degree to graphite carbon line (b-axis).

On the other hand, our present result stated above can be explained if we assume the contribution of fairly strong interactions between C_{60} and graphite. Ionization potentials of C_{60} molecule and graphite are 7.6 eV and 4.6 eV respectively, so there may take place electron transfer from graphite to C_{60} which results in charge transfer or Coulombic interaction between them besides the van der Waals interaction. The charge transfer interaction could fix and stop the rotation of C_{60} molecules even at room temperature, which may lead to a preferred directional interaction between C_{60} molecules. This situation results in one-dimensional arrangement of C_{60} molecules on graphite if we take into account of the most favorable relative arrangement for maximum stability of both interactions. A realistic model is shown in Fig. 3-25. If the first molecule (left-hand side) may sit on graphite so as to fit "naphthalene" part of C_{60} (red color) to a hexagon of graphite (yellow color), then there may be four equivalent sites (green color) on the graphite for the most favorable positions for the second molecule to make intermolecular interaction strongest. As for the third molecule there remains only two "equivalent" positions, on the same direction and on the 46.8° deflected direction (blue color). If the second molecule may be deformed by the effect of the first molecule, the same direction could be a preferential site for the third molecule. Actually straight one dimensional arrangement was most frequently observed, but some deflected linear arrays (not shown in the figure) were less frequently but definitely observed. These observations may support the above model. This model is just a qualitative speculation and actual simulative calculation is absolutely required.

General situation of discussions on epitaxial growth of thin films is very preliminary in any cases, especially on C_{60}, and a further study on this problem is off course interesting but it is a separate subject beyond the scope of this thesis work at the present stage. The most important point is a finding that there exists one-dimensional array of C_{60} molecules on a surface of graphite at the early stage of vacuum deposition. In addition, the substrate used has many microscopic boundaries because of artificial graphite. Therefore, the probable ordering along such boundary dislocation lines may not be excluded.

3.5. Phthalocyanine Films on HOPG

The generation of high quality, thin, continuous films is a major objective of the modern electronics industry. Phtalocyanines, in general, exhibit high thermal stability and sublime at temperatures in excess of 450°C. This property lends itself readily to the relatively simple procedure of thin film deposition, not applicable to functionalized phthalocyanines. Structures can be fabricated in a layer-like arrangement by sequential deposition and the use of masks. Another way of generating thin films of phthalocyanines is to use a technique borrowed from the field of polymer processing, spin coating, suitable for thermally unstable compounds. For the spin coating technique, materials need either to exhibit a liquid phase or as in the case of the sample in this study, solubility in relatively low boiling solvents. One way of solublising phthalocyanines is to substitute the periphery with medium length (6 to 10 carbon atoms) hydrocarbon chains. Octa- substituted phthalocyanines have been prepared which are either metal-free or substituted with nickel or copper. These phthalocyanines are by-products of various synthetic routes to prepare materials suitable for the deposition of Langmuir-Blodgett films. An aim is to generate materials that have physical properties suitable for spin deposition and also have good electrical properties. The two types of phthalocyanine were used and their structure is shown in Fig. 3-26 , where R is C_8H_{17} or OC_4H_9. It is convenient to use abbreviation for the otherwise rather long name. Throughout this discussion the following abbreviations will be used: octaocty- metal free phthalocyanine (OOMF) and octaneptyl-oxy metal free phthalocyanine (OPOMF).

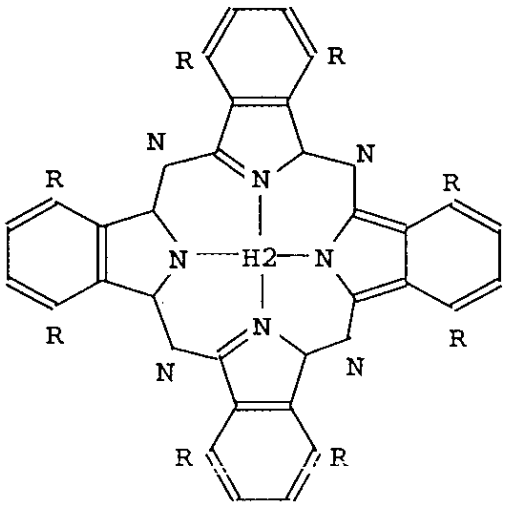

Fig. 3-26 Molecular structure of OOMF ($R=C_8H_{17}$) and OPOMF($R=OC_4H_9$).

The solution for the spin coating method was toluene. The basic principles of this method involve the rapid drying of a solution as it rotates

and spreads on a substrate revolving at speeds of approximately 2000 rps. A single drop of solution is allowed to fall onto the surface of a cleaned dust free substrate that is rotating. As the drop makes contact with the substrate it fragments into minute droplets that then move on the surface under the influence of centrifugal forces. As the liquid moves over the surface, the solvent evaporates rapidly leaving, if conditions are correct, a smooth, continuos film. Films deposited in this way are of the order of 500 ~1000 Å thick, depending on the particular material, and are clearly visible to the naked eye.

The surface observation of the films had been carried out several times but a good image had not been obtained. The reason is that the sample had high resistance itself and moreover, the films was not enough thin for STM experiment. Accordingly, in an attempt to improve conductivity, the samples were exposed to iodine vapor for 24 hrs, this also had the advantage of making the films visible and it could be obtained some STM images. The image of OOMF was, as shown in Fig. 3-27, obtained at -624.4 mV bias voltage and 1.0 nA tunneling current. The scan area was 150 Å × 150 Å , and a molecule size was about 25 Å. The distance between molecules was about 35 Å. On the other hand, in the case of OPOMF , the arrangement was seen in Fig. 3-28. The line extended one dimensionally, and the length was about 100 Å.

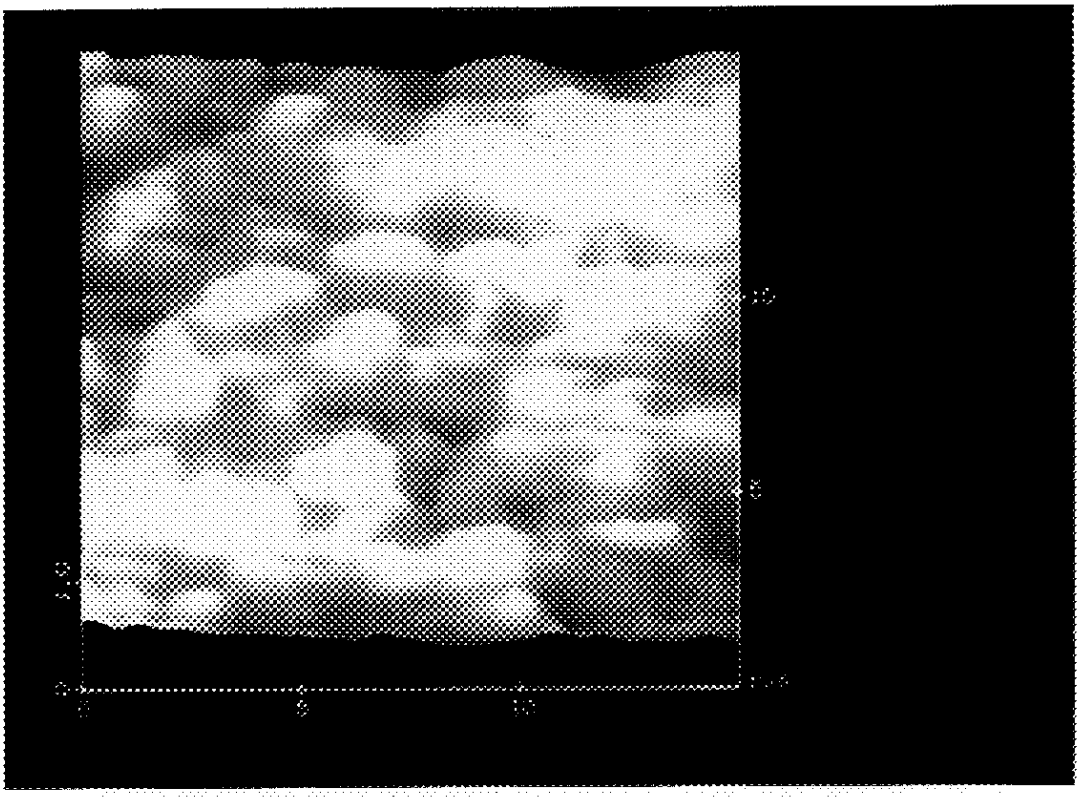

Fig. 3-27 STM image of OOMF film with a sample bias of -624.4 mV and a scanning area of 150 Å × 150 Å,

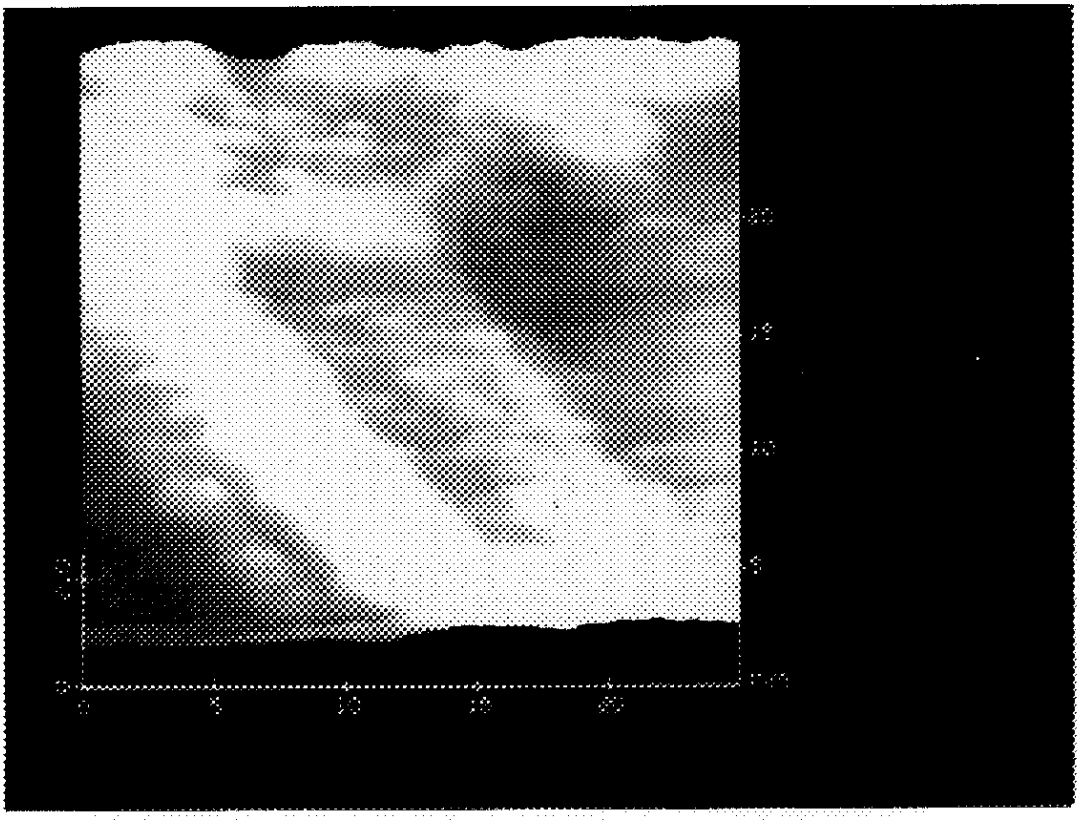

Fig. 3-28 STM image of OPOMF film with a sample bias of -52.8 mV and a scanning area of 250 Å × 250 Å,

3.6. Conclusion

This chapter summarized the experiments of surface structure for some functionality materials in air at room temperature.

In the case of HOPG, the images had atomic resolution and showed triangle lattice with 2.46 Å period, which is caused by the interaction between first layer's atom and second layer's atom.

In the case of BEDT-TTF salts, the surface images of all crystals were in good agreement with the crystal structure determined by X-ray diffraction. Therefore it suggests that the surface structure is almost the same as the crystal structure in bulk. We observed the images of BEDT-TTF molecules directly, and also we could indirectly assign the position of molecules in the insulating anion layer through the two types of bright and dark images of BEDT-TTF molecules. The resolution was rather at molecular level than atomic level. The reason may partly ascribe to the condition of the sample surface. In our case, all samples were not specially treated to make it clean. Moreover, surface observations were carried out in air.

In the case of C_{60}, some images were obtained in which one-dimensional clustering of C_{60} molecules was detected. There are some possibilities for epitaxial growth due to the interactions of C_{60}-C_{60} and C_{60}-graphite involving the charge transfer. More study is required to make it clear.

In the case of phthalocyanine films, it was too difficult to obtain good images. We could improve an image of phthalocyanines by doping iodine, but still we could hardly distinguish phthalocyanine from iodine definitely.

References

[1] M. Amrein, A. Stsiak, H. Gross, E. Stoll and G. Travaglini: *Science*, **240**(1988)514.

[2] J. S. Foster and J. E. Frommer: *Nature*, **333**(1988)542.

[3] J. K. Spong, H. A. Mizes, L. J. Lacomb Jr, M. M. Dovek, J. E. Frommer and J. S. Foster: *Nature*, **338**(1989)137.

[4] P. H. Lippel, R. J. Wilson, M. D. Miller, Ch. Woll and S. Chiang: *Phys. Rev. Lett.*, **62**(1989)171.

[5] K. Kobayashi, T. Tukada and N. Isshiki: *Kotaibutsuri*, **25**(1990)39 [In Japanese].

[6] K. Oshima, T. Mori, H. Inokuchi, H. Urayama, H. Yamochi and G. Saito: *Phy. Rev.*, **B39**(1989)11387.

[7] T. Sugano, H. Hayashi, M. Kinoshita and K. Nishikida: *Phy. Rev.*, **B39**(1989)938.

[8] H. Urayama, H. Yamochi, G. Saito, S. Sato, T. Sugano and M. Kinoshita, A. Kawamoto, J. Tanaka, T.Inabe, T. Mori, Y. Maruyama, H. Inokuchi and K. Oshima: *Chem. Lett.*, **1988**,463.

[9] K. Oshima, T. Mori, H. Inokuchi, H. Urayama, H. Yamochi and G. Saito: *Phys. Rev.*, **B37**(1988)938.

[10] H. Mori, S. Tanaka, K. Oshima, G. Saito, T. Mori, Y. Maruyama and H. Inokuchi: *Solid State Commun.*, **74**(1990)1261.

[11] M. Oshima, H. Mori and G. Saito: *Chem. Lett.*, **1989**,1159.

[12] M. Yoshimura, N. Ara, M. Kageshima, R. Shiota, A. Kawazu, H. Shigekawa and Y. Saito: *Hyoumenkagaku*, **11**(1990)25 [In Japanese].

[13] A. Kawazu, M. Yoshimura, H. Shigekawa, H. Mori and G. Saito: *J. Vac. Sci. Technol.*, **B9**(1991)1006.

[14] H. Mori, S. Tanaka, T. Mori, Y. Maruyama, H. Inokuchi and G. Saito: *Solid State Commun.*, **78**(1991)49.

[15] W. Krätschmer, K. Fostiropoulos and D. R. Huffman: *Chem. Phys. Lett.*, **170**(1990)167.

[16] W. Krätschmer, L. D. Lamo, K. Fostiropoulos and D. R. Huffman: *Nature*, **347**(1990)354.

[17] R. Tycko, R. C. Haddon, G. Dabbagh, S. H. Glarum, D. C. Douglass and A. M. Mijsce: *J. Phys. Chem.*, **95**(1991)518.

[18] C. Yannoni, R. Jhonson, G. Meijer, D. Bethune and J. Salem: *J. Phys. Chem.*, **95**(1991)9.

[19] D. S. Bethune, G. Meijer, W. Tang. H. J. Rosen: *Chem Phys. Lett.*, **174**(1990)219.

[20] D. S. Bethune, G. Meijer, W. Tang. H. J. Rosen, W. Golden, H. Seki, C. Brown and M. de Vries: *Chem Phys. Lett.*, **179**(1991)181.

[21] R. Meilunas, R. P. H. Chang, S. Liu and M. Kappes: *J. Appl. Phys.*, **70**(1991)5128.

[22] R. J. Wilson, G. Meijer, D. S. Bethune, R. D. Johnson, D. D. Chambliss, M. S. de Vries, H. E. Hunziker and H. R. Wendt: *Nature*, **348**(1990)621.

[23] J. L. Wragg, J. E. Chemberlain, H. W. White, W. Krätschmer and D. R. Huffman: *Nature*, **348**(1990)623.

[24] T. Chen, S. Howells, M. Gallagher, L. Yi, D. Sarid, D. L. Lichtenberger K. W. Nebesny and C. D. Ray: *J. Vac. Sci.*, **B10**(1992)170.

[25] X. P. Gao *et al.*: (unpublished).

[26] Y. Z. Li, J. C. Patrin, M. Chander, J. H. Weaver, L. P. F. Chibante and R. E. Smalley: *Nature*, **351**(1991)547.

[27] Y. Guo, N. Karasawa and W. A. Goddard III: *Nature*, **351**(1991)464.

[28] S. Liu and M. M. Kappes: *Thin Solid Films*, **216**(1992)142.

[29] Y. Z. Li, M. Chander, J. C. Patrin, J. H. Weaver, L. P. F. Chibante and R. E. Smalley: *Science*, **253**(1991)429.

[30] E. J. Snyder M. S. Anderson, W. M. Tong, R. S. Williams, S. J. Anz, M. M. Alvarez, Y. Rubiin, F. N. Diederich and R. L. Whetten: *Science*, **253**(1991)171.

[31] D. Sarid *et al.*: *Ultramicroscopy* (to be published)

[32] P. Dietz, K. Fostiropoulos, W. Krätschmer and P. K. Hansuma: *Appl. Phys. Lett.*, **60**(1992)62.

[33] Su Wang and P. R. Buseck: *Chem. Phys. Lett.*, **182**(1991)1.

[34] M. Mikami, T. Takeuchi, I. Fukuda, H. Sato and R. Mikami: 4th C_{60} Symp. (Toyohashi in JAPAN ,1993).

4. Electronic Structure Studied by STM

4.1. Introduction

Since Giaever's first measurement of the superconducting energy gap using an Al-Al_2O_3-Al planar junction, tunneling spectroscopy has become one of the most powerful techniques for studying the properties of superconducting materials[1]. Tunneling spectroscopy provides a direct measure of the quasiparticle density of state at and near the Fermi level. It also measure of the pair potential of the Cooper pairs and the spectral density of the coupling strength, $\alpha^2F(\omega)$. The characterization of samples can be made by performing tunneling experiments as a function of temperature, magnetic field, transport current and crystal orientation. Giaever's experiment was supported Bardeen, Cooper and Schreiffer's (BCS) theory of superconductivity, which predicted a gap in the quasiparticle density of state at the Fermi level. BCS theory predicts the equation: $2\Delta/kT_c = 3.52$, where k is Boltzman's constant. This ratio is a measure of the coupling strength of the Cooper pairs. Gieaever and others found that Al, Nb, V, In, Ta and other materials have the ratios quite close to the predicted value[2]. But the most notable exception to this rule is Pb and tunneling was again the key to understanding the disparity for this strongly coupled superconductor.

Giaever also found that $2\Delta/kT_c$ was 4.3 for lead, then Gieaever *et. al.* considered that there is a discrepancy between BCS theory and the density of state measured by tunneling spectroscopy[3]. Eliashberg derived a theory which could account for strongly coupled superconductors in terms of $\alpha^2F(\omega)$[4]. McMillan and Rowell used this theory and showed that this modification of the BCS theory was enough to account for tunneling characteristics of most superconducting material within a few percent[5].

Almost immediately after Bednorz and Müller discovered superconductivity in copper oxide[6], several groups in the world performed experiments to determine the nature of the superconductivity in these materials. At the time of Bednorz and Müller discovery, several groups had low temperature STM and were immediately employed to measure the

energy gap of the high T_c materials [7],[8],[9]. Low temperature STM/STS is the best tool to study superconductivity itself, so in this chapter, we applied room temperature STM/STS for a organic conductor and low temperature STM/STS for a $YBa_2Cu_3O_y$ high T_c superconductor. At first, the electronic structure of $(BEDT\text{-}TTF)_2KHg(SCN)_4$ for the plane along b-axis was measured at room temperature. In the next section, the energy gap of $YBa_2Cu_3O_y$ single crystal was determined by using our LTSTM/STS.

4.2. $(BEDT\text{-}TTF)_2KHg(SCN)_4$

Two-dimensionality is very essential to get a metallic organic conductor or superconductor with the suppression of metal-insulator transition at low temperatures. The STM image for the plane along the b-axis (perpendicular to 2D plane) of $(BEDT\text{-}TTF)_2KHg(SCN)_4$ crystal in Fig. 3-11(b) shows the alternate stacks of BEDT-TTF conductive layers and $KHg(SCN)_4$ anion layers. The cross-sectional curve, as shown in Fig. 4-1, clearly exhibits the corrugation with the period of 20 Å. The thickness of anion layer of this compound is rather large compared with $Cu(NCS)_2$ salt and therefore, the strong two-dimensionality in the electronic properties is expected because of its weak interlayer coupling. In other to clarify the local two-dimensionality experimentally we applied STM/STS technique which is the most relevant and unique method for this purpose.

The STS measurement was performed as follows: The tip was fixed at a position, *e.g.*, the mountain position (a) in Fig.4-1 , and *(dI/dV)-V* was measured, then the tip was moved along b-axis by about 2.5 Å step after measuring the *(dI/dV)-V* curve at each point. This process was carried out from mountain to next one through the valley. The results of this STS measurement are shown in Fig. 4-2 in which the ordinate indicates *(dI/dV)/(I/V)*, i.e., proportional to the normalized electron density of states. As the tip was moved by about 10 Å, the linear line (a) changed to a concave curve (e), and when it was moved by about 10 Å more, the curve returned to the linear line again. The period, 20 Å, coincides with the lattice constant of b-axis and, the linear and the concave curves may correspond to BEDT-TTF metallic conduction layer and $KHg(SCN)_4$ insulating layer, respectively, and these results indicate that this crystal actually has 2D electronic structure as well as 2D crystal structure.

This is the first finding of microscopic electronic structure for an organic conductor and it is impossible to get the exactly corresponding data by any macroscopic method. Mori *et al.* recently reported the persistence of metallic conductivity down to 0.6K [10], and Osada *et al.* demonstrated the 2D character of this crystal with the high-field magneto transport measurement[11]. Our finding described above is just consistent with these results and

moreover, it directly assures the weak interlayer coupling and strong two-dimensionality in this substance for the first time.

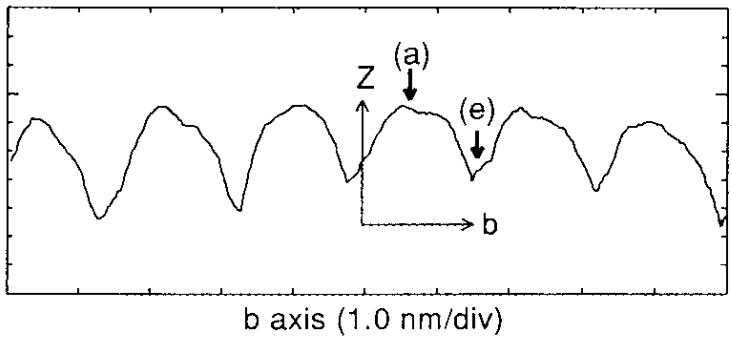

Fig. 4-1 The cross section curve of $(BEDT\text{-}TTF)_2KHg(SCN)_4$ along b-axis which is perpendicular to 2D plane.

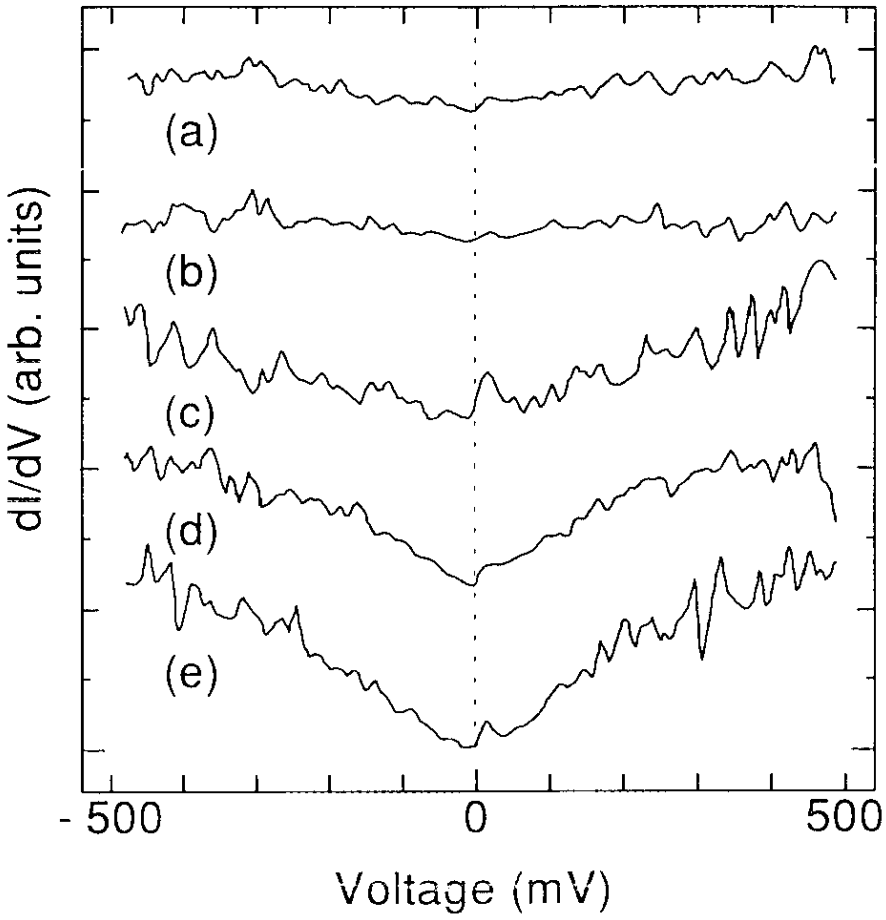

Fig. 4-2 The STS measurement along the b-axis for an $(BEDT\text{-}TTF)_2KHg(SCN)_4$ single crystal. The tip was moved by a 2.5 Å step from (a) to (e).

4.3. Y-Ba-Cu-O

Since the discovery of high temperature superconductivity in the layered copper oxides by Bednorz and Müller[6], there have been huge number of reports of superconductivity in this new class of oxides with T_c's in the temperature range of 40-130 K. A number of experimental methods have been applied for the study of these new superconducting compounds, including transport, magnetic susceptibility, low temperature X-ray crystallography, calorimetry and farinfrared transmission and reflectance spectroscopy. In particular, superconducting gaps Δ were studied by infrared transmission, reflectance measurements, NMR, Raman scattering, heat capacity and tunneling spectroscopy[12],[13],[14].

The tunneling spectroscopy has traditionally been an important method for the study of superconductivity. The method provides not only a direct measure of the superconducting energy gap and the phonon density of states, but also of the electron-phonon coupling strength, which plays a crucial role in the mechanism of superconductivity. Therefore this method is considered to define the best superconducting gap among all methods above-mentioned. In order to measure tunneling spectra, such types of tunneling junction have been used as planar junction, point contact, break junction and STM. In the planar junction method, it is difficult to control the insulating film thickness and it is measuring all over electronic structure. Point contact and break junction methods give the local information but the sample surface is damaged easily under pressure. Therefore, STM is the most powerful tool for the moment because STM is non contact type and has atomic level resolution.

The BCS ratio, $2\Delta/kTc$, is an important factor to characterize the nature of a superconductor, and it is known that the standard value of BCS ratio is 3.52 in the weak coupling limit for conventional superconductors. The values of BCS ratio of $YBa_2Cu_3O_y$ high Tc superconductor have been determined by several groups as shown in Table 4-1. The data were obtained not only by tunneling spectroscopy but also by different techniques for single crystal, sintered pellet or film samples. These values are scattering over the range of 2

Table 4-1 Gap measurements for $YBa_2Cu_3O_y$

Investigator	Method	Sample	T_C	$2\Delta/kT_C$
Mori *et al.* (Present work)	STM/S	Single crystal	88K:magnetic susceptibility	7.6±0.4
Kirk[15] *et al.*	Point contact	Sintered pellet	90K:assumed	8 ~ 10
Edgar[16] *et al.*	Point contact	Sintered pellet	91.7K:zero gap point	5
Kirtley[17] *et al.*	Point contact and infrared absorption	Single crystal and sintered pellet	90K:assumed	3.7 ~ 5.6 1.6 ~ 3.4
Moreland[18] *et al.*	Break Junction	Sintered pellet	93K:midpoint of resistance transition	4.8
Lee[19] *et al.*	Planar junction		60K:zero gap point	8
Iguchi[20] *et al.*	Planar junction	Sintered pellet	60K:zero gap point	10.5
Collins[21] *et al*	Infrared		90K:zero gap point	8
Cooper[22] *et al.*	Raman scattering	Single crystal	90K:magnetic susceptibility	7.5 ~ 9
Gallagher[23] *et al.*	STM/S	Sintered pellet	88K:zero resistance	13
Lozanne[24] *et al.*	STM/S	Film	84K:zero resistance	11
Betum[25] *et al.*	Point contact	Sintered pellet	84K:mid point resistance transition	3.2

to 13 in terms of $2\Delta/kTc$. There are some reasons of a scattering of these values. One reason is the sample quality. The best quality sample such as single crystal or epitaxial film should be used. The second reason is the vagueness in determining the transition temperature. Most of high temperature superconductors have comparatively wide transition. Transition temperature defined by resistivity measurement has relatively large uncertainty. The better value of transition temperature is given by a sharp magnetic susceptibility transition detected by SQUID magnetometer. The third reason may be the existence of anisotropy of the gap. In the case of YBCO system, the ratio of the gap for c-axis (perpendicular to Cu-O plane) to *ab* plane (parallel to Cu-O plane) was reported as 1.5~1.7 by several methods of tunneling spectroscopy[26],[27],[28], farinfrared reflectance[29], Raman scattering[30] and NMR[31]. Therefore, the gap energy obtained by optical measurement or planer contact junction may correspond to a superposition of the values for c-axis and *ab* plane. In order to determine a reliable value of BCS ratio, it is necessary to use high quality sample and to measure *Tc* and gap with most reliable methods. In this sense, a single crystal should be used, and STM/STS and SQUID meter may be the best combination for determining Δ and *Tc*.

In this experiment, a single crystal of YBCO superconductor was studied by our LTSTM. The crystal structure is shown in Fig. 4-3 and the *ab* plane is parallel to the Cu-O plane. A single crystal of $YBa_2Cu_3O_y$ was supplied by Prof. M.Sato. The size of the crystal is $8\times4\times3$ mm^3, as shown in Fig. 4-4. The magnetic susceptibility measurement was carried out by using SQUID magnetometer (SHE Vriable Temperature Susceptometor (VTS) 900 series, Biomagnetic Technologies, inc.) with the help of Dr. Y. Nakzawa and Mr. H. Ogata, and the superconducting transition temperature (*Tc*) of the sample was detected at 88K as a sharp and clear diamagnetic response (Fig. 4-5.). The sample was fixed on copper plate with gold paste and was set in the LTSTM unit. The typical result of tunneling spectroscopy at 12 K on the *ab* plane is shown in Fig. 4-6. The absolute value for the density of state (ordinate) can be hardly determined in usual tunneling spectroscopy because the tunneling current may be substantially disturbed depending on the measuring conditions, e.g. surface conditions. The spectral energy, however, is relatively unaffected by such surface conditions, so the qualitative features are not so sensitive to surface conditions. Several spectral scans are

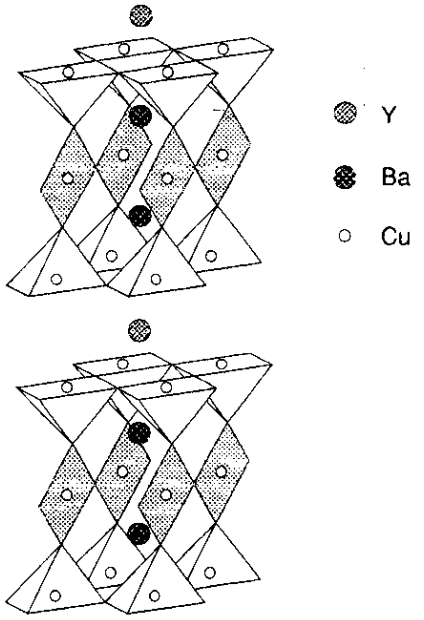

Fig. 4-3 The crystal structure of YBCO.

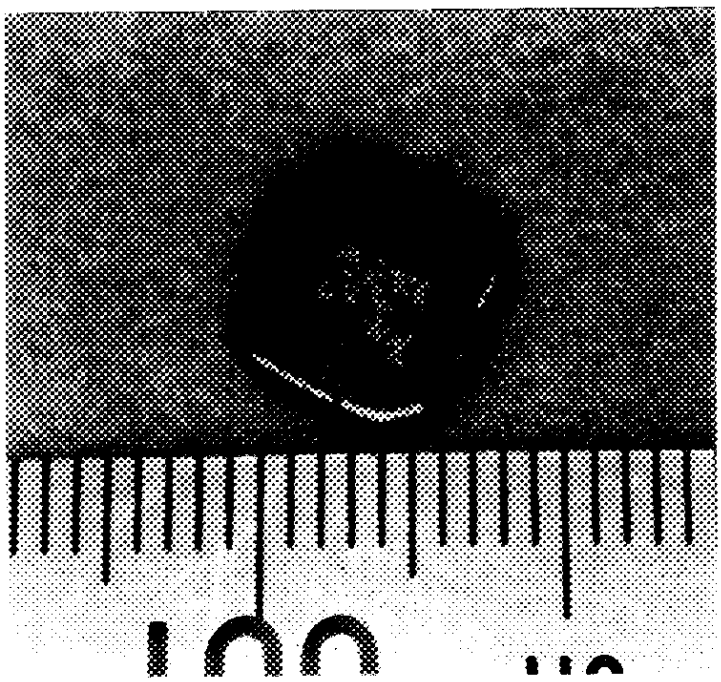

Fig. 4-4 The photograph of YBCO single crystal.

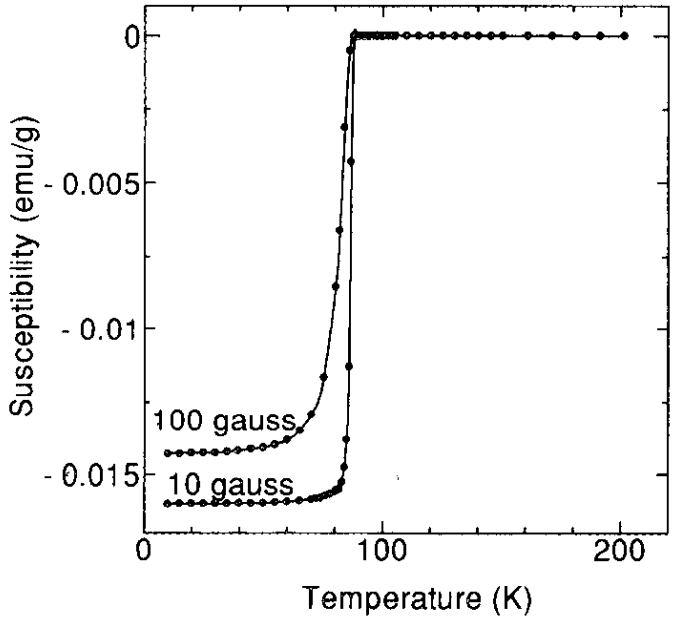

Fig. 4-5 Magnetic susceptibility curves of YBCO single crystal taken in the field of 10 gauss and 100 gauss. The on set of superconductivity is at approximately 88K.

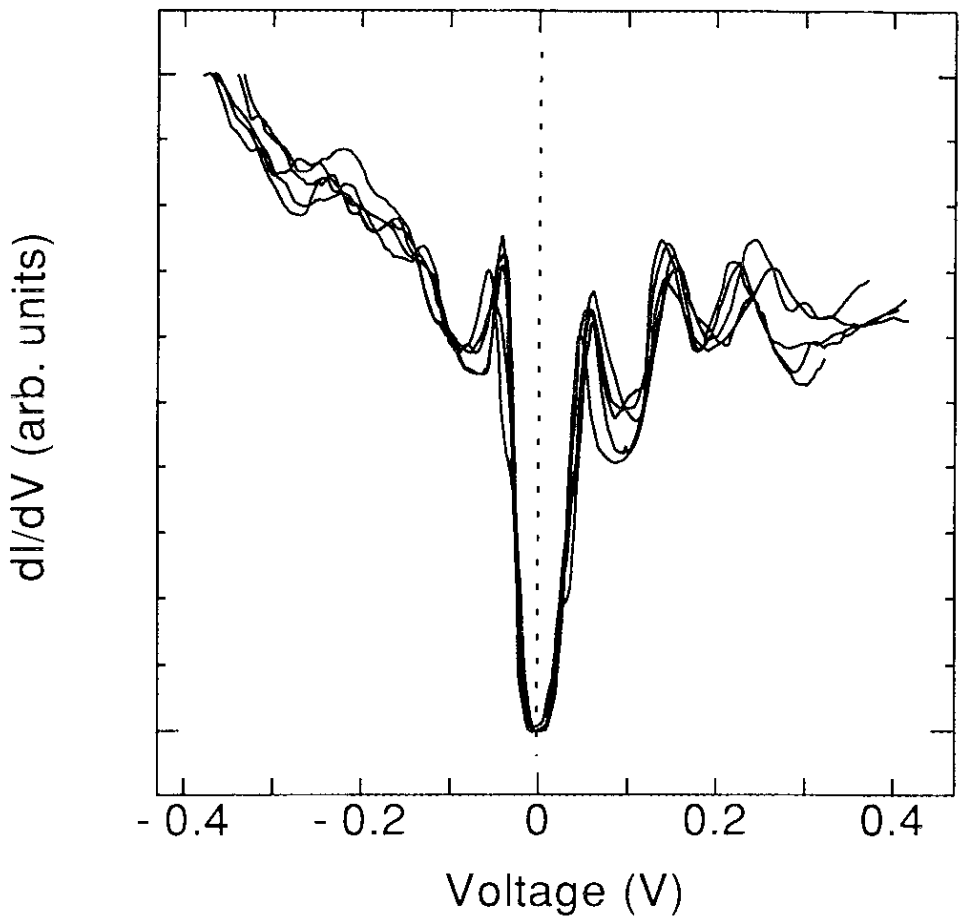

Fig. 4-6 The dI/dV vs V measured at 12K for YBCO single crystal by LTSTS. The superconducting gap is clearly recognized. The five scans traced almost identical structure, which indicates fairly well stability in this measurement. See the text on the ordinate scale.

shown in this figure. As shown in this figure, the superconducting gap is clearly recognized. The stability of the measurements was relatively well and the error-bars of the 2Δ value are within ±6%. In order to determine average value of 2Δ, four different scans are plotted in Fig. 4-7 with expanding energy scale. Assuming the constant density of states upon transition, each 2Δ was determined graphically (The area of a valley should be equal to that of the hill.). The average superconducting gap 2Δ was estimated to 58±3.5mV and correspondingly $2\Delta/kTc$=7.6±0.4. The value is larger than 3.52 which corresponds to a conventional weak coupling superconductor in BCS theory. It is a critical problem that this large value might be within the strong coupling regime or extending beyond BCS theory.

High Tc copper oxide superconductors have more or less two-dimensional structure, and anisotropic nature in superconductivity, if it exist, should be most interesting point in the study on these substances. Hasegawa *et al.* reported the different gap energies for *ab* plane and perpendicular plane to it of $Bi_2Sr_2CaCu_2O_y$ by STM tunneling spectroscopy[32]. Photoelectron spectroscopy, however, has issued an opposite result with respect to the anisotropy in gap energy[33]. In our case, since we have not yet succeeded in measuring a tunneling spectrum for different planes, we can discuss only on a wider gap for *ab* plane (conducting plane). This may be one reason for large BCS ratio. *Tc* is uniquely determined without any anisotropy, and the physical meaning of BCS ratio may become quite obscure in the case of anisotropic superconductor. Anyhow, such large value for $2\Delta/kTc$ may imply that the mechanism for superconductivity could be somewhat beyond the electron-phonon coupling (not only strong coupling). It remains still challenging, so we have to complete LTSTM/STS at least.

In conclusion our result is considered to be a reliable data for $YBa_2Cu_3O_y$ on the *ab* plane because single crystal was used and the transition temperature was determined from the sharp transition curve of magnetic susceptibility by using SQUID magnetometer, and STM which is the best tool for measurement of an energy gap was used. Our value, 7.6±0.4, seems to be reasonable judging from the Table and the discussion described above.

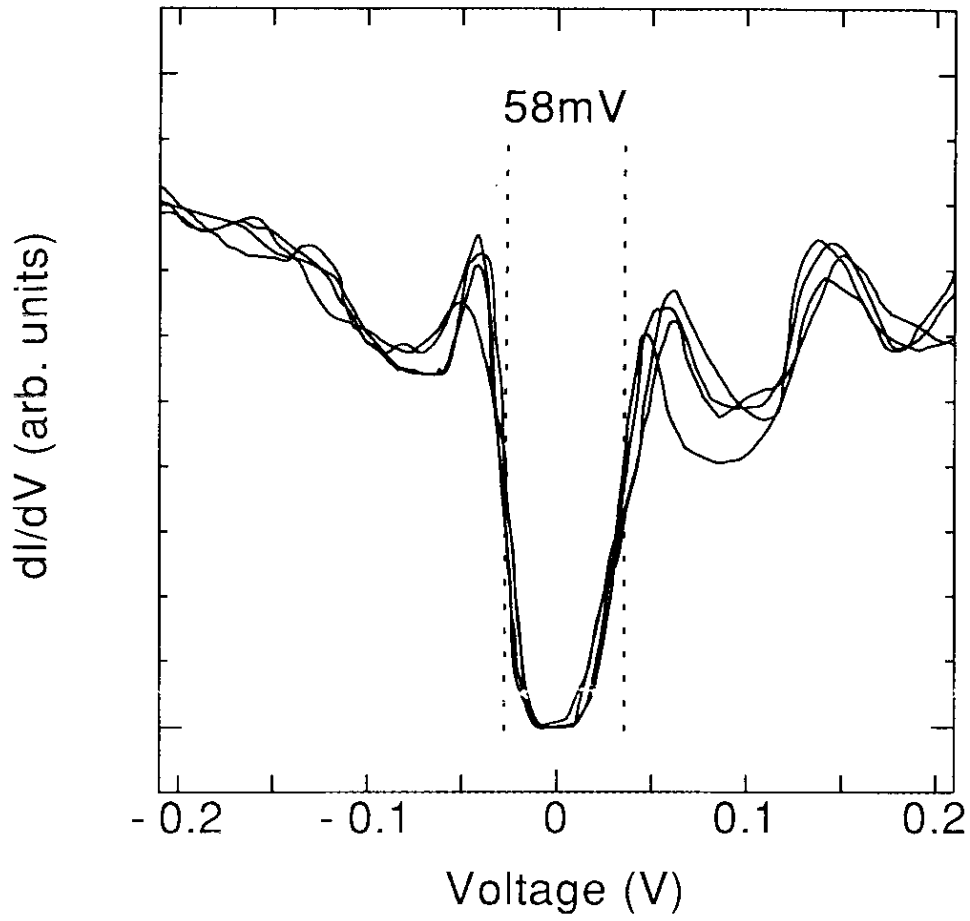

Fig. 4-7 The superconducting gap is estimated to be 2Δ~58meV. Using Tc of 88K then $2\Delta/kTc$ is 7.6±0.4 which is indicating strong-coupling regime.

4.4. Conclusion

The STM/STS has shown to be a unique tool for studying electronic structure of some materials. For the $(BEDT\text{-}TTF)_2KHg(SCN)_4$ salt, electronic property of molecular level region could be revealed, that is, alternation of metallic layer and insulating layer was clearly displayed by this method. On the other hand, for a single crystal of $YBa_2Cu_3O_y$, the superconducting gap measurement by LTSTM/S showed that it might be a strongly-coupled superconductor with $2\Delta/kT_c=7.6\pm0.4$.

Our LTSTM/STS machine has not yet been completed because LTSTS function is still not completely available. The atomic resolution and stability should be improved more at low temperatures.

References

[1] I. Giaever: *Phys. Lett.*, **5**(1960)147.

[2] T. Van Duzer, C. W. Turner: *"Plinciple of Superconductive Device Circuit"*, Elsevier, New York (1981).

[3] I. Giaever, H. R. Hart and K. Megerle: *Phys. Rev. Lett.* , **10**(1963)14.

[4] G. M. Eliashberg: *JETP*, **11**(1960)696.

[5] W. L. McMillan and J. M. Rowell: *Phys. Rev. Lett.*, **19**(1965)108.

[6] J. G. Bednorz and K. A. Müller: *Z. Phys.*, **B64**(1986)189.

[7] M. Naito, D. P. E. Smith, M. D. Kirk, B. Oh, M. R. Hahn, K. Char, D. B. Mitzi, J. Z. Sun, D. J. Webb, M. R. Beasley, O. Fischer, T. H. Geballe, R. H. Hammond, A. Kapitulnik and C. F. Quate: *Phys. Rev.*, **B35**(1987)7228.

[8] J. R. Kirtley, C. C. Tsuei, Sung I. Park, C. C. Chi, J. Rozen and M. W. Shafer: *Phys. Rev.*, **B35**(1987)7216.

[9] S. Pan, K. W. Ng, A. L. de Lozanne, J. M. Tarascon and L. H. Greene: *Phys. Rev.*, **B35**(1987)7220.

[10] H. Mori, S. Tanaka, K. Oshoma, G. Saito, T. Mori, Y. Maruyama and H. Inokuchi: *Solid State Commun.*, **74**(1990)1261.

[11] T. Osada *et al.*; *"The phisiscs and Chemistry of Organic Superconductors"* ed. by G. Saito and S. Kagoshima, (Springer-Verlag, 1990)p.220.

[12] Z. Schlesinger, R. L. Greene, J. G. Bednorz and K. A. Müller: *Phys. Rev.*, **B35**(1987)5334.

[13] P. E. Shulewski, A. J. Sievers, S. E. Russek, H. D. Hallen, D. K. Lathrop and R. A. Buhrmman: *Phys. Rev.*, **B35**(1987)5330.

[14] U. Walter, M. S. Sherwin, A. Stacy, P. L. Richards and A. Zettl: *Phys. Rev.*, **B35**(1987)7216.

[15] M. D. Kirk, D. P. E. Smith, D. B. Mitzi, J. Z. sun, D. J. Webb, K. Char, M. R. Hahn, M. Naito, B. Oh, M. R. Beasley, T. H. Geballe, R. H. Hammond, A. Kapitulnik and C. F. Quate: *Phys. Rev.*, **B35**(1987)8850.

[16] A. Edgar, C. J. Adkins and S. J. Chandler: *J. Phys. C*, (1987)L1009.

[17] J. R. Kirtley, R. T. Collins, Z. Schlesinger, W. J. Gallagher, R. L. Sandstrom, T. R. Dinger and D. A. Chance: *Phys. Rev.*, **B35**(1987)8846.

[18] J. Moreland, J. W. Ekin, L. F. Goodrich, T. E. Capobianco, A. F. Clark, J. Kwo, M. Hong and S. H. Liou: *Phys. Rev.*, **B35**(1987)8856.

[19] M. Lee, A. Kapitulnik and M. R. Beasley: *Bull. Am. Phys. Soc.*, **33**(1988)594.

[20] I. Iguchi, H. Watanabe, Y. Kasai, T. Mochiku, A. Sugishita and E. Yamaka: *Jpn. J. Appl. Phys.*, **26**(1987)L645.

[21] R. T. Collins, Z. Schlesinger, F. Holtzberg, P. Chaudhari and C. Feild: *Proceedings on High Tc Workshop*, Oberlech, Austria (August 1988).

[22] S. L. Cooper, M. V. Klein, B. G. Pazd, J. P. Rice and D. M. Ginsberg: *Phys. Rev.*, **B37**(1988)5920.

[23] M. C. Gallagher, J. G. Adler, J. Jung and J. P. Franck: *Phys. Rev.*, **B37**(1988)7846.

[24] A. L. de Lozanne, K. W. Ng, S. Pan, R. M. Silver and A. Berezin: *J. Microsc.*, **152**(1988)117.

[25] P. J. M. van Betum, L. E. C. van de Leemput, L. W. M. Schreurs, P. A. A. Teunissen and H. van Kempen: *Phys. Rev.*, **B36**(1987)843.

[26] J. S. Tsai, I. Takeuchi, J. Fujita, T. Terashima, Y. Bando, K. Iijima and K. Yamamoto: *Physica C* **157**(1989)537.

[27] J. S. Tsai, I. Takeuchi, J. Fujita, T. Yoshitake, S. Miura, S. Tanaka, T. Terashima, Y. Bando, K. Iijima and K. Yamamoto: *Physica C* **153-155**(1988)1385.

[28] A. Zettl, A. Behrooz, G. Briceno, W. N. Creager, M. F. Crommie, S. Hoen and P Pinsukanjana: "*Mechanism of High Tenperature Superconductivity*" ed. by K. Kanimura and A. Oshiyama (Springer-Verlag, 1989) p.249.

[29] R. T. Collins, Z. Schlesinger, F. Holtzberg and C. Field: preprint.

[30] S. L. Cooper, F. Slakey, M. V. Klein, J. P. Rice, E. D. Bukowski and D. M. Ginsberg: *Phys. Rev.* **B38**(1988)11934.

[31] D. J. Durand, S. E. Barrett, C. H. Penninton, C. P. Slichter, E. D. Bukowski, T. A. Friedmann, J. P. Rice and D. M. Ginsberg: "*Strong Correlation and Superconductivity*" ed by H. Fukuyama, S. Maekawa and A. P. Malozemoff (Springer-Verlag, 1989) p.244.

[32] T. Hasegawa, M. Nantoh and K. Kitazawa; *Ohyobutsuri*, **59**(1990)1642[In Japanese].

[33] D. S. Dessan, B. O. Wells, Z. -X. Shen, W. E. Spicer, A. J. Arko, R. S. List, D. B. Mitzi and A. Kapitulnik; *Phys. Rev. Lett.*; **66**(1990)2160.

Summary

A Scanning Tunneling Microscopy (STM) is a new type of microscopy with atomic resolution. The microscopy is based on quantum mechanical tunneling effect of electron and has been applied to various fields. Now, we can use the technique not only in atmosphere at room temperature but also in vacuum or in water, at low temperatures or high temperatures. Moreover, not only solid state structures but also electronic structures of a surface can be detected in atomic scale by Scanning Tunneling Spectroscopy (STS). An STS which combines STM with tunneling spectroscopy can reveal the electronic structure of some real space portion with atomic resolution. The method is especially useful for detecting an energy gap structure near Fermi surface of materials in superconducting state. A complete STM/STS system for low temperature operation, however, has not been available so far. In this thesis work, the surface and electronic structures of some functionality molecular materials are studied by STM firstly at room temperature, and in parallel an STM/STS system for low temperature has been designed. In final part of this work, electronic structures of a high Tc superconductor has been tried to study with using the newly constructed low temperature STM (LTSTM) system.

In our LTSTM, there are three features. 1) The unit is designed compactly and rigidly. As the result, the unit can reduce the influence of vibrations and can be used in the magnetic field by combining with slender dewar. 2) Although a piezoelectric response is reduced by cooling from room temperature to 4K with a factor about one tenth, the fine approach mechanism at low temperature by using a step motor and differential screws is enough to bring the sample towards the tip with step size to ensure that the tip does not crash into the sample. The fine approach achieves about 70 Å stroke per one step. 3) It is very difficult but important to decrease the electrical noise in a long cable between sample and pre-amplifier. We use the I-V converter which has better performance. In the system, the electric source is two dry batteries, then the stability is much better than the commercial STM case.

The surface observations has been carried out for some functionality materials in atmosphere at room temperature with the use of conventional STM. In the case of BEDT-TTF salt single crystals, all images are well corresponding to their crystal structures determined by X-ray diffraction. In the case of C_{60} films on HOPG, a soccer ball is recognized and one-dimensional clustering of C_{60} molecules is detected. In the case of phthalocyanine films on HOPG prepared by spin coating method, we can improve STM images by doping iodine.

The electronic structures of $(BEDT\text{-}TTF)_2KHg(SCN)_4$ (organic conductor) and $YBa_2Cu_3O_y$ (oxide superconductor) have been studied. A $(BEDT\text{-}TTF)_2KHg(SCN)_4$ salt has 2D crystal structure in *ac* plane. The step-wise measurements of tunneling spectra along the b-axis clearly show a 2D character in the electronic structure. In the case of $YBa_2Cu_3O_y$, the superconducting gap 2Δ at 12K is recognized to be ~58meV by our LTSTM. This result shows that it might be a strongly-coupled superconductor with $2\Delta/kT_c$=7.6±0.4, which is almost consistent with the reported value.